

PARTICLE, POLYMER & PHASE DYNAMICS IN LIVING FLUIDS

Alison E. Koser

A DISSERTATION

in

Mechanical Engineering and Applied Mechanics

Presented to the Faculties of the University of Pennsylvania

in

Partial Fulfillment of the Requirements for the

Degree of Doctor of Philosophy

2016

Supervisor of Dissertation

---

Paulo E. Arratia, Associate Professor of Mechanical Engineering and Applied Mechanics

Graduate Group Chairperson

---

Kevin Turner, Professor of Mechanical Engineering and Applied Mechanics

Dissertation Committee

Paulo E. Arratia, Associate Professor of Mechanical Engineering and Applied Mechanics

Prashant K. Purohit, Associate Professor of Mechanical Engineering and Applied Mechanics

Mark Goulian, Edmund J. and Louise W. Kahn Endowed Term Professor of Biology and Physics

PARTICLE, POLYMER & PHASE DYNAMICS IN LIVING FLUIDS

© COPYRIGHT

2016

Alison E. Koser

## ACKNOWLEDGEMENT

I thank my advisor Professor Paulo E. Arratia for his unending support and encouragement throughout my graduate studies and academic pursuits. I am grateful for this guidance, enthusiasm, passion, and creativity, which has motivated me and equipped me with the skills and confidence to complete my dissertation and continue my journey in academic research and teaching. I also thank my committee members, Professor Prashant Purohit and Professor Mark Goulian. Professor Purohit's expertise in non-equilibrium dynamics and polymer dynamics has enriched my graduate research and shaped my interest in fundamental mechanics. His support and excitement have provided encouragement. I am grateful for my discussions with Professor Goulian, whose expertise, ideas, and assistance have helped solve problems I could not have done alone. I am thankful for the assistance of the Mechanical Engineering Department staff, particularly Maryeileen Griffith who has eased my transition to and through graduate school.

I include a special thanks for current and former members of the Arratia Lab. In particular, I thank Arvind Gopinath, whose expertise and cleverness has paved the way for much of this work and whose support has nurtured me. I am also thankful for the opportunity to learn from and work alongside Nathan Keim, who taught me how to build and develop experimental setups and cultivated my understanding of fundamental research in fluid dynamics. I am also grateful for the help and patience of Gabe Juarez, Lichao Pan, and Somayeh Farhadi. I am also thankful to Denise Wong, who first introduced me to experiments with bacteria, and to Ed Steager and Elizabeth Hunter, who have patiently taught and shared with me experimental protocols and techniques for working with bacteria.

I thank my family, my husband Mike Patteson and my parents Ken and Linda Koser, for the continued love and support.

# ABSTRACT

## PARTICLE, POLYMER & PHASE DYNAMICS IN LIVING FLUIDS

Alison E. Koser

Paulo E. Arratia

Flocks of birds, schools of fish, and jams in traffic surprisingly mirror the collective motion observed in the microscopic wet worlds of living microbes, such as bacteria. While these small organisms were discovered centuries ago, scientists have only recently examined the dynamics and mechanics of suspensions that contain these swimming particles. I conduct experiments with the model organism and active colloid, the bacterium *Escherichia coli*, and use polymers ( $< 1 \mu\text{m}$ ), particles ( $1\text{-}10 \mu\text{m}$ ), and phase-separated mixtures ( $> 100 \mu\text{m}$ ) to probe the non-equilibrium dynamics of bacterial suspensions. I begin by examining the hydrodynamic interactions between swimming *E. coli* and particles. For dilute suspensions of bacteria in Newtonian fluids, I find that larger particles can diffuse faster than smaller particles - a feature absent in passive fluids, which may be important in particle transport in bio- and geo-physical settings populated by microbes. Next, I investigate *E. coli* dynamics in non-Newtonian polymeric solutions. I find that cells tumble less and move faster in polymeric solutions, enhancing cell translational diffusion. I show that tumbling suppression is due to fluid viscosity while the enhancement in swimming speed is due to fluid elasticity. Visualization of single fluorescently-labeled DNA polymers reveals that the flow generated by individual *E. coli* is sufficiently strong that polymers can stretch and induce elastic stresses in the fluid. These, in turn, can act on the cell in such a way to enhance its transport. Lastly, I probe the interplay between kinetics, mechanics, and thermodynamic of active fluids by examining the evolution of an



active-passive phase interphase. I create this interface by exposing regions of a dense bacterial swarm to UV light, which locally immobilizes the bacteria. Vortices etch the interface, setting interface curvature and speed. The local interface curvature correlates with the interface velocity, suggesting an active analog of the Gibbs-Thomson boundary condition. My results have implications for the burgeoning field of active soft matter, including insight into their bulk rheology, how material properties are defined and measured, and their thermodynamics and kinetics.

# Contents

<b>1</b>	<b>Introduction</b>	<b>1</b>
1.1	Introduction and Motivation . . . . .	1
1.2	Background . . . . .	5
1.2.1	Fluid rheology and single swimmers . . . . .	5
1.2.2	Suspensions of Active Colloids & Swimmers . . . . .	10
1.3	Thesis Overview . . . . .	17
<b>2</b>	<b>Particle dynamics in active fluids: The role of particle size on particle diffusion in aqueous <i>E. coli</i> suspensions.</b>	<b>28</b>
2.1	Introduction . . . . .	28
2.2	Experimental Methods . . . . .	31
2.3	Results and Discussion . . . . .	32
2.3.1	Mean Square Displacements . . . . .	32
2.3.2	Diffusivity and Cross-over Times . . . . .	34
2.3.3	Effective Temperature . . . . .	36
2.3.4	Active Diffusivity of Passive Particles in Bacterial Suspensions	39
2.4	Maximum Particle Effective Diffusivity $D_{\text{eff}}$ . . . . .	41
2.5	Summary and Conclusions . . . . .	43
<b>3</b>	<b>Polymer dynamics in active fluids: how swimming <i>E. coli</i> and polymer molecules interact.</b>	<b>48</b>
3.1	Introduction . . . . .	48
3.2	Methods . . . . .	50
3.3	Results & Discussion . . . . .	51
3.3.1	<i>E. coli</i> trajectories . . . . .	51
3.3.2	Statistical measures of cell motility . . . . .	54
3.3.3	Enhancement in cell run time . . . . .	57
3.3.4	Enhancement in <i>E. coli</i> swimming speed and wobbling suppression . . . . .	59
3.3.5	Polymer dynamics in bacterial-generated flows . . . . .	61
3.4	Conclusions . . . . .	63

<b>4</b>	<b>Phase dynamics in active fluids: The growth and form of active-passive phase boundaries in dense swarms of bacteria.</b>	<b>69</b>
4.1	Introduction . . . . .	69
4.2	Methods . . . . .	71
4.3	Results and Discussion . . . . .	74
4.3.1	Active-Passive Phase Order Parameter . . . . .	74
4.3.2	Boundary-Flow interaction . . . . .	78
4.3.3	The growth and form of active interfaces: Connecting kinetics, thermodynamics, and mechanics . . . . .	84
4.4	Conclusions . . . . .	85
<b>5</b>	<b>Summary &amp; Perspectives</b>	<b>91</b>
5.1	Summary . . . . .	91
5.2	Future Recommendations . . . . .	93
5.3	Perspectives . . . . .	95
	<b>Appendices</b>	<b>99</b>
<b>A</b>	<b>Supplementary Materials for particle dynamics in <i>E. coli</i> suspensions</b>	<b>100</b>
A.1	Role of confinement and interfacial effects . . . . .	100
A.2	Role of concentration on particle dynamics . . . . .	102
A.2.1	Collapse of particle distributions . . . . .	102
A.2.2	Effective diffusivity and cross-over time . . . . .	103
A.2.3	Comparison to previous experiments . . . . .	105
A.2.4	Spectral analysis . . . . .	108
A.3	MSD for a diffusing tracer . . . . .	108
A.4	Previous theory for small and large Peclet number . . . . .	112
A.5	Qualitative estimate for the maximum effective particle diffusivity $D_{\text{eff}}$ . . . . .	113
<b>B</b>	<b>Supplementary Materials for swimming <i>E. coli</i> in polymer solutions</b>	<b>119</b>
B.1	Rheological characterization of solutions . . . . .	119
B.1.1	Shear viscosity and elasticity of CMC solutions . . . . .	119
B.2	Methods . . . . .	124
B.3	MSD Crossover time increases with polymer concentration . . . . .	127
B.4	<i>E. coli</i> Rotational Diffusivity and Mean Run Time . . . . .	128
B.5	Suppression of Wobbling with Molecular Weight . . . . .	128
B.6	Polymer dynamics due to flow generated by tethered cells . . . . .	129
B.7	Estimation of Weissenberg Numbers . . . . .	131

# List of Tables

B.1	Rheological properties of CMC ( $MW = 7.0 \times 10^5$ ) solutions . . . . .	121
B.2	Rheological properties of XG . . . . .	123
B.3	Results of linear regression analysis . . . . .	125
B.4	Viscosity, concentration, relaxation time, and bundle rotation frequencies used to estimate $Wi$ in solutions of CMC. . . . .	133

# List of Figures

1.1	An overview of active colloidal systems - natural and synthetic. . . .	2
1.2	Single natural swimmers moving in Newtonian fluids. . . . .	7
1.3	Single swimmers moving in viscoelastic fluids. . . . .	9
1.4	Collective dynamics in active colloids. . . . .	11
1.5	Interplay between passive and active particles. . . . .	12
1.6	Snapshots of experimental fluids . . . . .	19
2.1	Trajectories of 2 $\mu\text{m}$ particles in <i>E. coli</i> suspensions . . . . .	30
2.2	Mean-square displacements (MSD) of 2 $\mu\text{m}$ particles in <i>E. coli</i> suspen- sions . . . . .	33
2.3	Effective particle diffusivities $D_{\text{eff}}$ and crossover times in bacterial sus- pensions . . . . .	35
2.4	Distribution of 2 $\mu\text{m}$ particle speeds $p(v)$ . . . . .	37
2.5	Active diffusivities $D_A = D_{\text{eff}} - D_0$ . . . . .	40
3.1	Kinematics of swimming <i>E. coli</i> cells in both Newtonian and viscoelas- tic fluids. . . . .	52
3.2	Swimming speeds of <i>E. coli</i> in buffer and polymeric solutions. . . . .	54
3.3	Statistical measures characterizing cell trajectories. . . . .	55
3.4	Viscosity suppresses tumbling. . . . .	57
3.5	Elasticity suppresses wobbling while increasing cell velocity. . . . .	59
3.6	Polymer stretching by a tethered <i>E. coli</i> cell. . . . .	62
4.1	Swarms of <i>Serratia marcesens</i> . . . . .	73
4.2	Phase boundary. . . . .	75
4.3	The interface and active/passive phases interact. . . . .	80
4.4	The interface and active/passive phases interact. . . . .	81
4.5	Phase interface velocity depends on interface curvature and bacterial flow. . . . .	84
A.1	The probability distribution of 2 $\mu\text{m}$ particle displacements $\text{PDF}(\Delta x, \Delta t, c)$	104
A.2	The non-Gaussianity parameter of 2 $\mu\text{m}$ tracers particles . . . . .	105
A.3	Effective diffusivities, $D_{\text{eff}}$ for 2 $\mu\text{m}$ particles, as a function of bacteria concentration . . . . .	106

A.4	Spectral density of particle speeds at varying <i>E. coli</i>	107
A.5	Enhanced particle diffusion due to bacteria activity.	110
B.1	Shear viscosity of CMC solutions.	120
B.2	Relaxation times of polymeric solutions	121
B.3	Shear viscosity versus shear rate for Xanthan Gum solutions	122
B.4	Shear viscosity of PEG solutions	123
B.5	Crossover time vs. concentration	127
B.6	Tumble Angles	129
B.7	Wobbling dependence on polymer molecular weight	130
B.8	Polymer end-to-end distributions	132

# Chapter 1

## Introduction

### 1.1 Introduction and Motivation

Active materials are ubiquitous in nature and permeate an impressive range of length scales, ranging from collectively swimming schools of fish ( $L \sim \text{km}$ ) [1] and marching armies of ants ( $L \sim \text{mm}$ ) [2] to motile microorganisms ( $L \sim \mu\text{m}$ ) [3–6] and cellular molecular motors ( $L \sim \text{nm}$ ) [1, 8]. Suspensions of self-propelling active particles, which inject energy internally and create flows within the fluid medium, constitute so-called *active* fluids [9, 10]. The internally-injected energy drives the fluid out of equilibrium (even in the absence of external forcing) and can lead to swirling collective motions [11] and beautiful pattern formations [12, 13], that naively appear unique to life. Indeed, the motility of swimming microorganisms such as nematodes, bacteria, protozoa and algae has been a source of wonder and curiosity for centuries now. Indeed, upon discovering bacteria in 1676, Anton van Leeuwenhoek proclaimed: “*I must say, for my part, that no more pleasant sight has ever yet come before my eye than these many thousands of living creatures, seen all alive in a little drop of water, moving among one another*” [14].

Since then, scientists have observed and classified other collective large-scale pat-

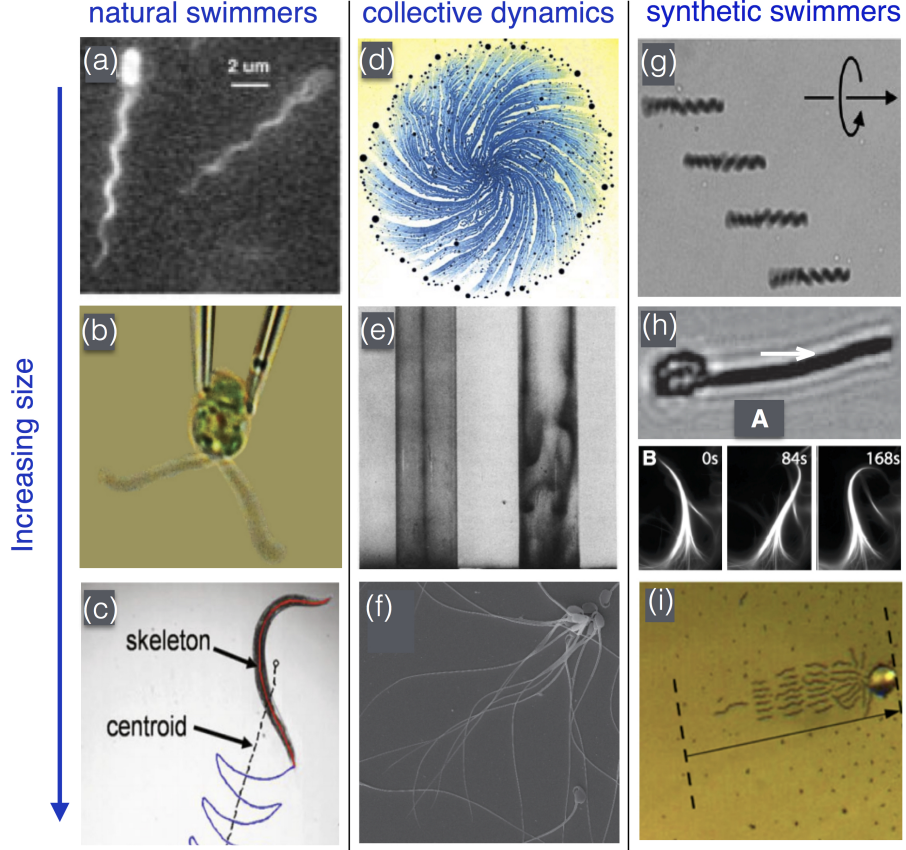


Figure 1.1: An overview of active colloidal systems - natural and synthetic. (a)-(c): Individual natural swimming microorganisms arranged in order of increasing size: (a) prokaryotic bacterium *Escherichia coli* with cell body approximately  $2\ \mu\text{m}$  [29], (b) Eukaryotic unicellular alga *Chlamydomonas reinhardtii* with a cell body that is approximately  $8\ \mu\text{m}$  [5], and (c) multi-cellular organism *C. elegans* that is approximately  $1\ \text{mm}$  long [30]. (d)-(f) Examples of collective behavior seen in aggregates of microorganisms: (d) a bacterial colony of *P. vortex* on agar [31], (e) bioconvection of algae under shear [17], and (f) cooperative behavior in sperm [32]. (g)-(i) Synthetic swimmers: (g) field driven translation of helical magnetic robots [33], (h:A) magnetically driven chain comprised of paramagnetic spheres attached via DNA strands [34], (h:B) metachronal waves generated by re-constituted microtubule-motor extracts [35], and (i) magnetically driven surface snakes comprised of self-assembled  $80\text{-}100\ \mu\text{m}$  spheres [36].



terns in active fluids, such as vortices [15, 24], flocks [16], and plumes [17–19] that form at high concentrations of their organisms and highlight the link between life, fluid flow, and complex behavior. Surprisingly, recently-developed synthetic materials/particles also exhibit these life-like complex behaviors, and include materials, such as shaken grains [20, 21], phoretic colloidal particles [11, 22], and soft field-responsive gels [23]. These active particles (living or synthetic, hard or soft), as collected in Fig. 1.1, have sizes that range from a few tenths of a micron to a few hundred microns, spanning colloidal length scales over which thermal noise is important [24]. The persistent motion of these active colloids allows one to either direct (channel) or extract (harness) the energy injected at one length scale at other scales. For instance, activity can render large, normally athermal spheres diffusive [25] and yield controllable, directed motility of micro-gears [26–28].

Recent interest in active fluids is driven by both practical and scientific relevance [10]. From a technological and engineering standpoint, active suspensions play an integral role in medical, industrial, and geophysical settings. A handful of examples include the spread and control of microbial infections [37, 38], the design of microrobots for drug delivery [39] or non-invasive surgery [40], the biofouling of water-treatment systems [41] and the biodegradation of environmental pollutants [42]. From a scientific standpoint, active suspensions are interesting in their own right because they are non-equilibrium systems that exhibit unique and curious features such as turbulent-like flow in the absence of inertia [43, 44], anomalous shear viscosities [45–47], enhanced fluid mixing [48, 49], and giant density fluctuations [21, 24]. Because these features are generic to many other active materials (e.g. cell, tissues, vibrated granular matter), active suspensions serve as a playground for understanding and deciphering generic features of active materials across many length scales.

The suspending fluid in these active suspensions can be simple and Newtonian (e.g. water) or complex and non-Newtonian (e.g. mucus). Complex fluids are materials that are usually homogeneous at the macroscopic scale and disordered at the microscopic scale, but possess structure at the intermediate scale. Examples include polymeric solutions, dense particle suspensions, foams, and emulsions. These complex fluids often exhibit non-Newtonian fluid properties under an applied deformation. These properties include viscoelasticity, yield-stress, and shear-thinning viscosity. An overarching goal in the study of complex fluids is to understand the connection between the structure and dynamics of the fluid microstructure to its bulk flow behavior [22, 51]. For example, recent experiments by Keim and Arratia [52, 53], which visualize a monolayer of dense colloidal particles under cyclic shear at low strains, have shown how local particle re-arrangements connect to the suspension bulk yielding transition. This work highlights how local measures of the microstructure can shed new light on the bulk material response in an amorphous material.

In active fluids, it is even more challenging to link the activity at the microscale to the fluid meso- and macro-scales. This is because the interplay between the motion of active particles and the complex fluid rheology of the suspending medium leads to a number of intricate and often unexpected results. In particular, the local mechanical stresses exerted by microorganisms in an active colloidal suspension can alter the local properties of its environment [54]; while, simultaneously, the complex fluid rheology modifies the swimming gaits and spread of individual organisms [55, 75]. It is essential to understand this two-way coupling in order to predict, control, and mimic the properties of this emerging class of soft active materials.

An important example of this is in living tissues, which are continuously exposed to stimuli that lead to growth and remodeling of their structure. This remodeling in the

tissue microstructure is often implicated in medical conditions such as asthma. Recent work by Park *et al.* [56] has shown how tissue microstructural details, such as cell shape, affects bulk properties, such as fluidity and rigidity. In a similar vein, recent experiments have shown that the interplay between the motion of active particles and the complex fluid rheology of the suspending medium leads to a number of intricate and often unexpected results. In particular, the local mechanical stresses exerted by swimming bacteria in polymeric solutions can alter the local properties of its environment [54]; while simultaneously, the complex fluid rheology modifies the swimming gaits of individual organisms [55, 75]. It is essential to understand this two-way coupling in order to uncover the universal principles underlying these active complex materials and in order to design and engineer new active materials.

Here, I review recent work on active colloids moving in fluidic environments and discuss how recent theory and experiments have elucidated connections between micro-scale descriptions and the resulting macro-scale collective response. Next, I identify remaining challenges and present my thesis which investigates the dynamics of particle, polymers, and phases in suspensions of bacteria as model active fluids.

## 1.2 Background

### 1.2.1 Fluid rheology and single swimmers

#### Single swimmer in Newtonian fluids

Many organisms move in the realm of low Reynolds number  $\text{Re} \equiv \ell U \rho / \mu \ll 1$  because of either small length scales  $\ell$ , low swimming speeds  $U$  or both. In a Newtonian fluid with density  $\rho$  and viscosity  $\mu$ , this implies that inertial effects are negligible, the hydrodynamics is governed by the Stokes' equation, and stresses felt by the swimmer

are linear in the viscosity. To therefore achieve any net motion (i.e. swim), microorganisms must execute non-reversible, asymmetric strokes as shown in Fig. 1.2 in order to break free of the constraints imposed by the so-called “scallop theorem” [57].

In the Stokes’ limit, the flow caused by the moving particle can then be described as linear superposition of fundamental solutions such as stokelets and stresslets. The exact form of the generated flow depends on the type of swimmer. For instance, an externally-actuated swimmer with fixed gaits creates flow that decay a distance  $r$  away from the swimmer as  $1/r$ . A freely propelled swimmer is however both force free and torque free; therefore the induced fields are due to force dipoles, which decay as  $1/r^2$ , or higher order multipoles. Naturally-occurring, freely-moving organisms can typically be classified into one of two categories: (i) pullers (negative force dipole) such as *Chlamydomonas reinhardtii* [5] or (ii) pushers (positive force dipole) such as the bacteria *Escherichia coli* [48] and *Bacillus subtilis* [24,45]. Note that other organisms such as the alga *Volvox carteri* may fall between this pusher/puller distinction; other organisms move by exerting tangential waves along their surfaces and are called squirmers [4]. While this pusher/puller classification is limited and oversimplified, it provides a dichotomy for a reasonable framework.

The dipole approximations are useful in estimating force disturbances far from the swimmer. Closer to the moving swimmer, the flow field is time-dependent and can significantly deviate from these dipole approximations [58,59]. Significant theoretical work exists on characterizing these complex temporal and spatial flow fields around individual swimmers and obtaining approximate descriptions that may then be used as a first step in understanding how two and more swimmers interact [60]. Other geometries such as infinitely long waving sheets and cylinders have also been used to gain insight into the motility behavior of undulatory swimmers such as sperm cells

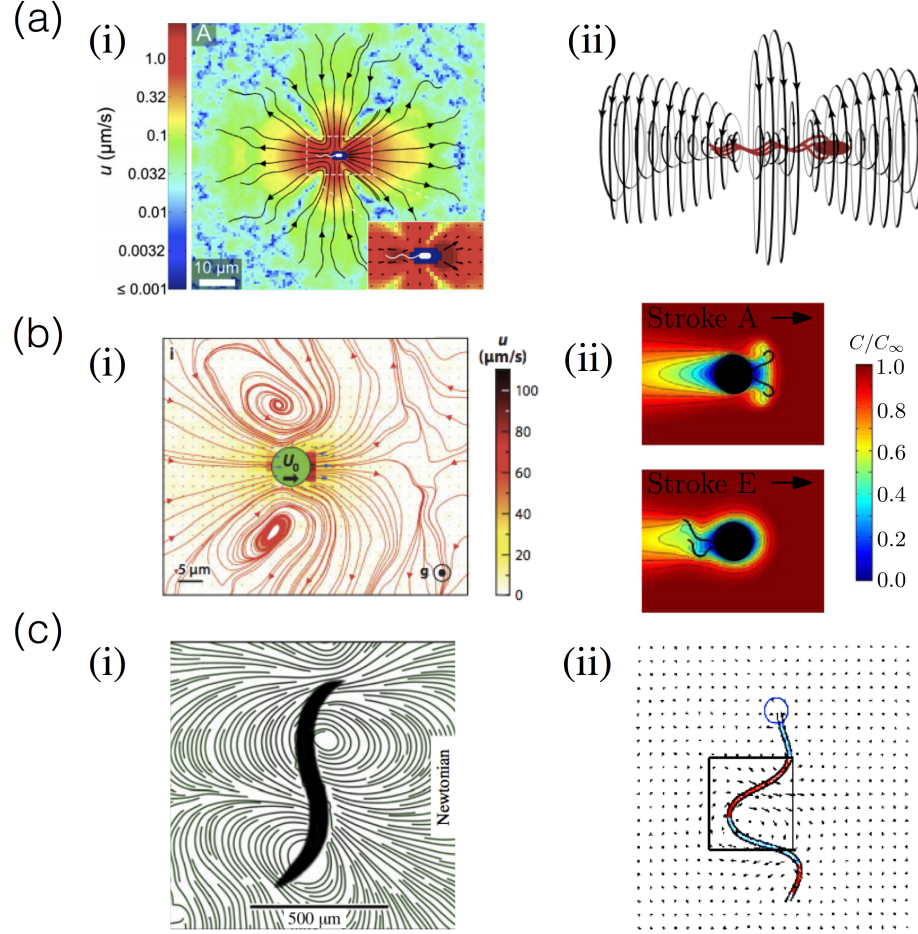


Figure 1.2: Single natural swimmers moving in Newtonian fluids. (a) (i) Experimentally measured period averaged, color-coded velocity field around *Escherichia coli* bacterium [60]. (ii) Three-dimensional streamlines of a simulation of the flow in a frame co-moving with the bacterium [58]. (b) (i) Averaged streamlines around *Chlamydomonas reinhardtii* [61] - the color map denoting velocity magnitudes. (ii) Snapshots of the computed nutrient concentration fields  $C$  around a model swimmer swimming in a nutrient gradient with undulatory strokes (A) and breaststrokes (B) [62]. (c) (i) Streamlines around a swimming nematode *C. elegans* [67]. (ii) Computed velocity fields around a flexible self-propelling swimmer [68].

and nematode (*C. elegans*) [62–64].

A feature common to these theoretical studies is that the swimming gait - i.e, the temporal sequence of shapes generating the propulsion - is assumed to be constant and independent of the fluid properties. Recent experiments paint a more colorful picture. Even in simple Newtonian fluids, fluid viscous stresses can significantly affect the microorganisms swimming gait and therefore their swimming speed [55,65].

### **Single swimmer in complex fluids**

The two-way coupling between swimmer kinematics and fluid rheological properties can give rise to many unexpected behaviors for microorganism swimming in complex fluids. For instance, the stresses in a viscoelastic fluid are both viscous and elastic, and therefore time dependent. Consequently, kinematic reversibility can break down and propulsion is possible even for reciprocal swimmers [66,69]. This effect is especially important for small organisms since the time for the elastic stress to relax is often comparable to the swimming period [55,70]. Therefore, elastic stresses may persist between cyclic strokes.

Emerging studies - some of which are highlighted in Fig. 1.3 - are revealing the importance of fluid rheology on the swimming dynamics of microorganisms. Consider the effects of fluid elasticity on swimming at low  $Re$ . Would fluid elasticity enhance or hinder self-propulsion? Theories on the small amplitude swimming of infinitely long wave-like sheets [73] and cylinders [74] suggest that fluid elasticity can reduce swimming speed, and these predictions are consistent with experimental observations of undulatory swimming in *C. elegans* [75]. On the other hand, simulations of finite-sized moving filaments [76] or large amplitude undulations [70] suggest that fluid elasticity can increase the propulsion speed - consistent with experiments on rotating

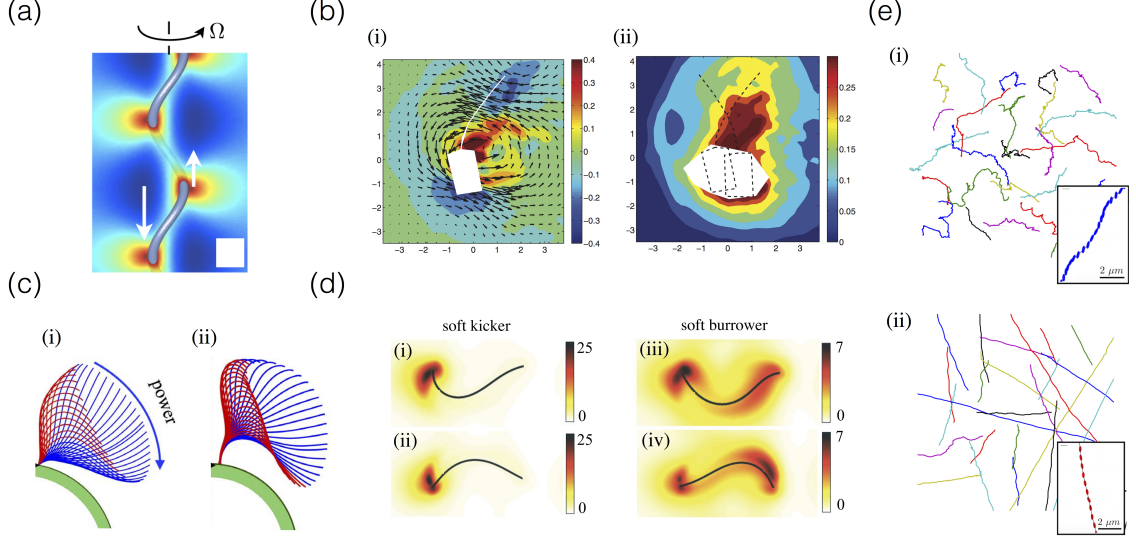


Figure 1.3: Single swimmers moving in viscoelastic fluids. (a) The axial component of fluid velocity generated by a rotating, force-free helical segment [71]. (b) Particle image velocimetry results for flow field around a flexible artificial swimmer moving in a two-dimensional fluid (i) vorticity (colors) and velocity (arrows) and (b) cycle averaged magnitude of the rate of strain tensor. The vorticity and rate-of-strain fields are normalized by the oscillation frequency. The white regions show the position of the swimmer at different instants throughout a cycle [72]. (c) (i) The sequence of shapes (swimming gait) attained by the cilia in *Chlamydomonas reinhardtii* in Newtonian fluid of viscosity around 6 Pa.s. The direction of the power stroke is indicated. (ii) The ciliary shapes seen when the same organism moves in a viscoelastic fluid are dramatically different [55]. (d) Contour plots of the polymers stress generated around a moving soft swimmer for a (i,ii) soft kicker and a (iii, iv) soft burrower. The mobility is affected by both the softness of the swimmer as well as by the elasticity of the fluid through which the swimmer moves [70]. (e) (i) *Escherichia coli* trajectories in water-like Newtonian fluid. Trajectories consist of straight segments punctuated by re-orienting tumbles. (Inset) The cell body wobbles with a characteristic amplitude and frequency. (ii) Replacing the Newtonian fluid with a viscoelastic fluid results in straighter trajectories with suppressed tumbling and cell body wobbles [65].

rigid mechanical helices [77]. In recent work on *Chlamydomonas reinhardtii* [55], the investigators found that the beating frequency and the wave speed characterizing the cyclical bending of the flagella are both enhanced by fluid elasticity. Despite these enhancements, the net swimming speed of the alga is hindered for fluids that are sufficiently elastic. Additionally shear-thinning viscosity effects *E. coli* may contribute to the increase in cell velocity [54] in polymer solutions but had little to no effect on the swimming speed of *C. elegans* [67]. Overall, the emerging hypothesis is that there is no universal answer to whether motility is enhanced or hindered by viscoelasticity or shear-thinning viscosity. Instead, the microorganism propulsion speed in complex fluids depends on how the fluid microstructure (e.g. polymers, particles) interact with the velocity fields generated by a particular microorganism.

### 1.2.2 Suspensions of Active Colloids & Swimmers

In general, a single active entity in a fluid - Newtonian or complex - behaves very differently from a suspension comprised of multiple such entities. Examples are shown in Fig. 1.4. Interactions between multiple swimmers (or active colloids) can lead to many fascinating phenomena not seen in suspension of passive particles at equilibrium including anomalous density and velocity fluctuations, large scale vortices and jets, and traveling bands and localized asters. Identifying means to relate the microstructural features (e.g. swimmer local orientation) to macrostructural properties and bulk phenomena would yield ways to control, manipulate, and even direct the properties in these novel living systems.



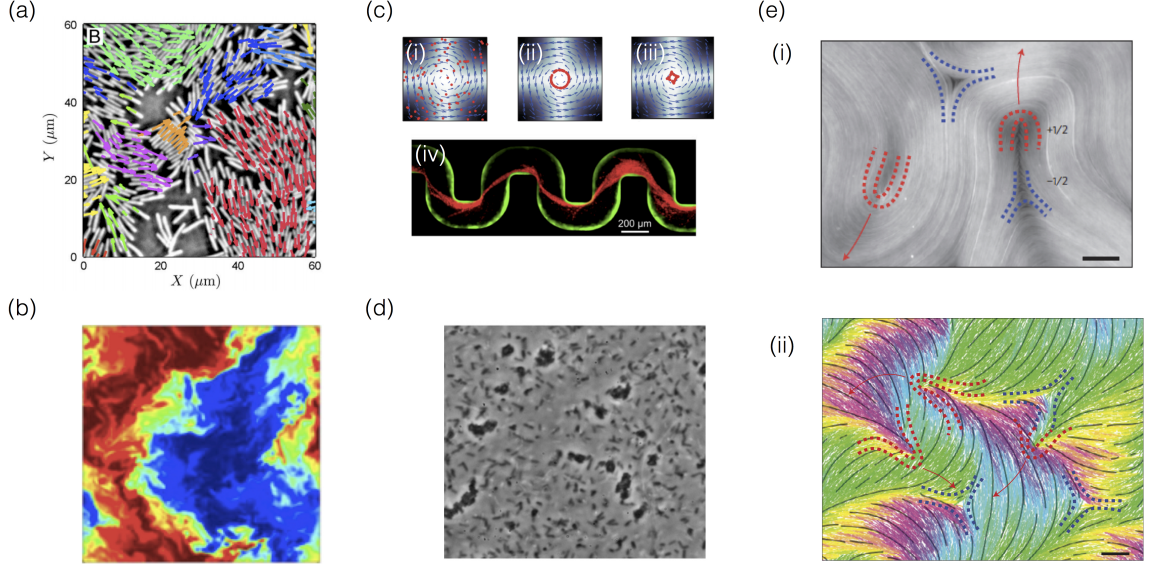


Figure 1.4: Collective dynamics in active colloids. (a) A snapshot of a swarming bacterial colony of *B. subtilis* on agar. Velocity vectors are overlaid on the bacteria. The lengths correspond to the speeds and are used to identify individual clusters [24]. (b) Scalar fields such as tracer concentration can be passively advected by the background velocity field generated by motile bacteria, demonstrating the mixing efficacy of active suspensions [78]. (c) (i-iii) Simulated spatial distribution of microorganisms in Taylor-Green vortices for different mobilities and elasticities. Relatively higher elastic effects cause an initially uniform distribution of microorganisms to aggregate. In real systems, where bacteria secrete polymers, this effect may enhance the aggregation and biofilm formation [79]. (iv) Bacterial biofilm streamers (red) form efficiently at high bacterial concentrations and may lead to catastrophic blockage in synthetic and natural channels through which fluids flow [80]. (d) Bright field microscopy image of a mixture of motile bacteria and polymers, evidencing the formation of bacterial clusters due to depletion effects [81]. (e) (i) Florescence microscopy image of a microtubule active nematic with defects of charge  $+1/2$  (red) and  $-1/2$  (blue). (ii) Snapshot of simulated nematic with marked defects. The color of the rod indicates its orientation and the black streamlines guide the eye over the coarse-grained nematic field [82].

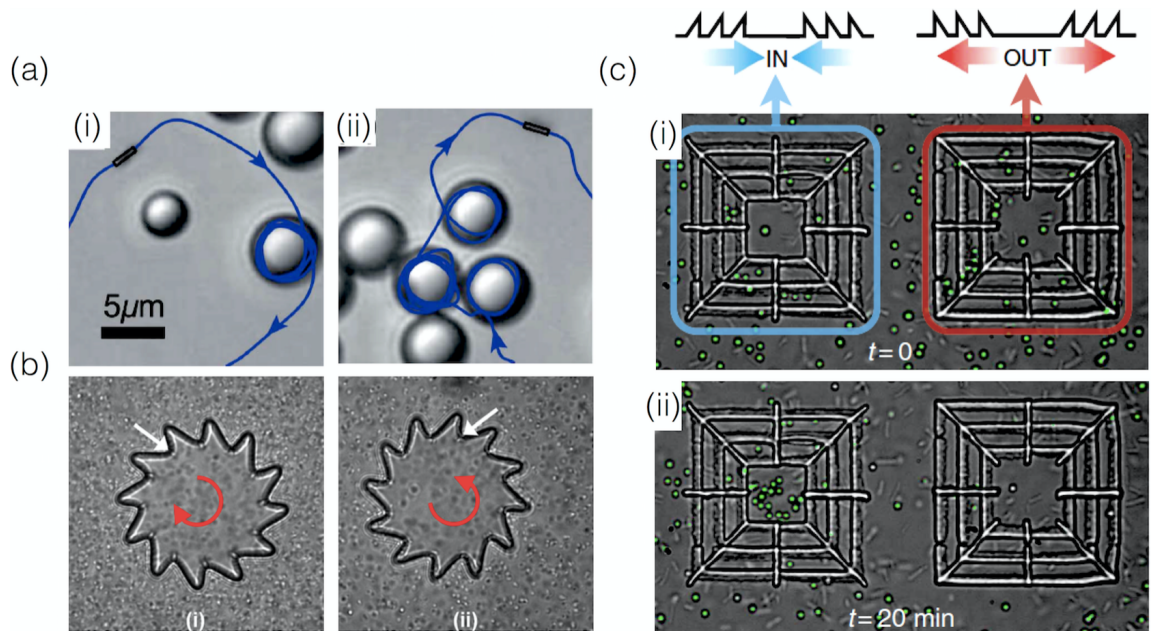


Figure 1.5: Interplay between passive and active particles. (a) Passive spheres temporarily capture micro-swimmers. The active colloids are Au-Pt rods moving in aqueous hydrogen peroxide [83]. Trajectories of single rods are shown in blue. (b) Bacterially driven microgears: Collisions between swimming bacteria and gears drive clockwise or counterclockwise rotation depending on the orientation of the teeth (i vs ii) [26]. (c) Surface topology in the presence of motile bacteria guides an (i) initial distribution of colloids to (ii) either aggregated (left) or depleted (right) regions [84].

## Dilute suspensions of active particles

A suspension of active colloids is considered dilute when interactions among particles are negligible. Even in the absence of particle interactions, however, the interplay between activity and the fluidic environment, as reviewed below, leads to novel and even unexpected phenomena.

### *Active particles in Newtonian fluids*

In the absence of activity, the shear viscosity  $\eta$  of a dilute suspensions of (passive) hard spheres is given by the Einstein relation,  $\eta = \eta_s(1 + \frac{5}{2}\phi)$  [85], where  $\eta_s$  is the viscosity of the suspending fluid and  $\phi$  is the volume fraction of the particles. In the presence of activity, however, the shear viscosity can be a strong function of the microorganisms swimming kinematics. We will briefly discuss the origins of this behavior below.

By using a kinetic theory based approach and solving the Fokker-Plank equation for the distribution of particle orientations under shear, Saintillan [86] showed that for a dilute suspension of force dipoles, the zero-shear viscosity  $\eta$  still follows an Einstein-like relation,  $\eta = \eta_s(1 + K\phi)$ , with the constant  $K$  now related to swimmer kinematics. For pushers,  $K < 0$ , while for pullers,  $K > 0$ . This leads to an interesting result: activity can either enhance or reduce the fluid viscosity depending on the swimmer kinematics (puller or pusher).

Due to the exceptionally low shear rates and stresses needed to realize these potential modifications in viscosity, experimental verifications of theories have been limited [45–47]. In 2009, Sokolov and Aranson [45] presented some of the first experimental evidence of activity-modified viscosity in a fluid film of pushers (*Bacillus subtilis*). They found that the presence of bacteria significantly reduces the suspension

effective viscosity. Subsequent experiments using shear rheometers have shown that the fluid viscosity can be effectively larger in suspensions of *C. reinhardtii* (pullers) [46] or lower in suspensions of *E. coli* (pushers) [47] compared to the case of passive particles (non-motile organisms) for the same shear-rates. Activity also seems to affect the suspension extensional viscosity in a similar way [87,88].

Clearly, activity has a fascinating effect on the viscosity of active suspensions; theoretical and numerical investigations seem to predict a regime in which the viscosity of the suspension can be lower than the viscosity of the suspending fluid. This striking phenomenon has been recently observed in experiments for *E. coli* (pushers) [45], where it was also found that the suspension viscosity linearly decreased as the bacterial concentration increased (in the dilute regime). Despite such advances, however, it has been a challenge to experimentally visualize the evolution of the microstructure (particle positions and orientations) during the rheological (viscosity) measurements. This type of information and measurements are critical to obtain insights into the physical mechanisms leading to this “vanishing” viscosity phenomenon in bacterial suspensions.

### ***Active particles in complex fluids***

Given the evidence that bacterial activity can alter suspension viscosity, it is natural to expect that the interaction of active particles or microorganisms with the fluid microstructure (polymers, particles, liquid crystals, cells, and networks) in complex fluids can also lead to interesting phenomena. Indeed, an extreme example of this is how even dilute concentrations of bacteria can disrupt long range order in lyotropic liquid crystals. The presence of bacteria can locally melt the underlying nematic order and generate large scale undulations with a length scale that balances bacterial activ-

ity and the anisotropic viscoelasticity of the suspending liquid crystal [89]. Related experiments using active liquid crystals comprised of reconstituted microtubule-motor mixtures [82] suggest similar disruptive effects on long range order. In this case, the active entities are motile defects, which generate flow, and are spontaneously created and annihilated within the ambient environment, as shown in Fig. 1.4e. These studies illustrate how even dilute concentrations of active particles can locally deform and activate the microstructure of complex fluids. These synergistic and dynamic materials possess qualities (new temporal and spatial scales) distinct from both passive complex fluids and suspensions of active particles in Newtonian fluids.

The microstructure of complex fluids, however, does not simply submit to the flow generated by active particles. Instead, as discussed in Section 2.2 and 2.3, the microstructure couples to the active particles, altering their swimming gait and speed. Indeed, the microstructure can even be exploited to adaptively guide active particles. For instance, it has recently been shown that the underlying nematic structure of lyotropic liquid crystals can align bacteria, controlling their motility and direction [89]. The nematic director can even set the bacterial direction near walls, where near-wall hydrodynamic torques can reorient cells [90]. In recent experiments, Trivedi *et al.* [91] demonstrated that in lyotropic liquid crystals bacteria can transport particles and non-motile eukaryote cells along the nematic director. Conversely, passive particles ( $\approx 1\text{-}15\ \mu\text{m}$  diameter) can be used to manipulate and capture active particles (self-propelled Au-Pt rods) [83], which tend to orbit along surfaces of passive particles, as shown in Fig. 1.5a. Together, these works seem to mirror the trafficking of cargo in cells by active motors [1] and suggest novel methods to transport active and passive components of these living, complex fluids, some of which are highlighted in Fig. 1.5.

## Non-dilute suspensions of active particles

The investigations briefly discussed above highlight the striking role of activity on material fluid properties even in the dilute regime when particle interactions are negligible. As the concentration of particles increases, however, the particle interactions (either steric and aligning interactions or hydrodynamic interactions) can suddenly give rise to collective motion and unexpected fluid rheology, as reviewed next.

Perhaps one of the first models for collective motion was proposed by Toner and Tu [16] using a modification of the classical liquid crystal model in the absence of fluid hydrodynamic interactions. This seminal work has been significantly extended theoretically to cover a range of interactions. Interestingly, these models as well as simpler discrete agent-based simulations are able to capture many of the universal features observed in natural active colloidal systems including flocking and collective behavior.

In order to incorporate the role of fluid interactions, recent mean-field models use dipole approximations in simple (Newtonian) fluids. Recent reviews by Koch and Subramanian [92] and Marchetti, *et al.* [10] summarize linear stability analyses of these mean-field models. The general consensus of these studies is that hydrodynamic interactions mediated by the fluid can, in some cases, destabilize homogeneous suspensions and assist collectively moving states.

Even when the suspending fluid is Newtonian, interactions between active particles can induce non-Newtonian features, such as elasticity. In order to model the rheology of active suspensions, Hatwalne *et al.* [93] generalized the kinetic equations for liquid crystals and obtained a general expression for frequency-dependent stress in an oscillatory shear flow. This stress depends on the detailed swimming kinematics (pusher or puller), the active correlation times, and the density. Importantly, the

theory predicts that – as the system approaches an orientational-order transition – this previously Newtonian fluid begins to exhibit elasticity, with elastic stresses than increase with the orientational order. This work highlights how the active particle microstructure can dramatically alter the bulk material properties.

On this front, experimental investigations have remained a challenge. It is difficult to track the dynamics of dense active particles and the resultant fluid flows they generate, and coupling these types of observations with simultaneous bulk rheology measurements has yet to be done in detail. More studies are needed to understand this coupling - even in the case of a suspending simple Newtonian fluid. The structure and dynamics of dense active suspensions - in the case of non-Newtonian suspending fluids - is new ground for exploration.

## 1.3 Thesis Overview

After review of the current literature, it is clear that many outstanding questions remain to be answered. In this work, I will focus on two of these questions. They are

1. One, how does the two-way, non-linear coupling between swimmer and fluid at microscopic scales affect the dynamics and properties at macroscopic scales?
2. Two, is it possible - as in classical, passive mechanics and thermodynamics - that effective equations of state can describe these active, far from equilibrium systems?

To this end, I explore particle, polymer, and phase dynamics in suspensions of the archetypical model organism *E. coli*. This work spans a wide class of active materials, bridging Newtonian and non-Newtonian suspending fluids and bacterial

concentrations that range from dilute and non-interacting to dense and collectively-moving. Figure 1.6 shows snapshots of the diverse experimental fluids. The following is a brief outline of the thesis work.

Chapter 2 starts by examining the dynamics of swimming *E. coli* suspended in Newtonian fluids by using tracer particles of varying size. For dilute suspensions of bacteria in Newtonian fluids, I find that larger particles can diffuse faster than smaller particles - a feature absent in passive fluids. This anomalous particle-size dependence is due to an interplay between the active dynamics of the *E. coli* and the passive Brownian motion of the particle and has broad implications for particle transport in active fluids ranging from geophysical to biophysical settings.

In Chapter 3, I investigate *E. coli* swimming dynamics in non-Newtonian fluids, namely, polymeric solutions. I find that even small amounts of polymer in solution can drastically change *E. coli* dynamics: cells tumble less and their velocity increases, leading to an enhancement in cell translational diffusion and a sharp decline in rotational diffusion. I show that tumbling suppression is due to fluid viscosity while the enhancement in swimming speed is mainly due to fluid elasticity. Visualization of single fluorescently-labeled DNA polymers reveals that the flow generated by individual *E. coli* is sufficiently strong to stretch polymer molecules and induce elastic stresses in the fluid, which in turn can act on the cell in such a way to enhance its transport. These results show that the transport and spread of chemotactic cells can be independently modified and controlled by the fluid material properties.

Chapter 4 describes tests of the use of constitutive equations and thermodynamic equations of state to active fluids, by creating and examining the structure and dynamics of an active-passive phase separated system. This interface is created in a bacterial swarm, by transforming regions of the swarm into passive phases by expos-



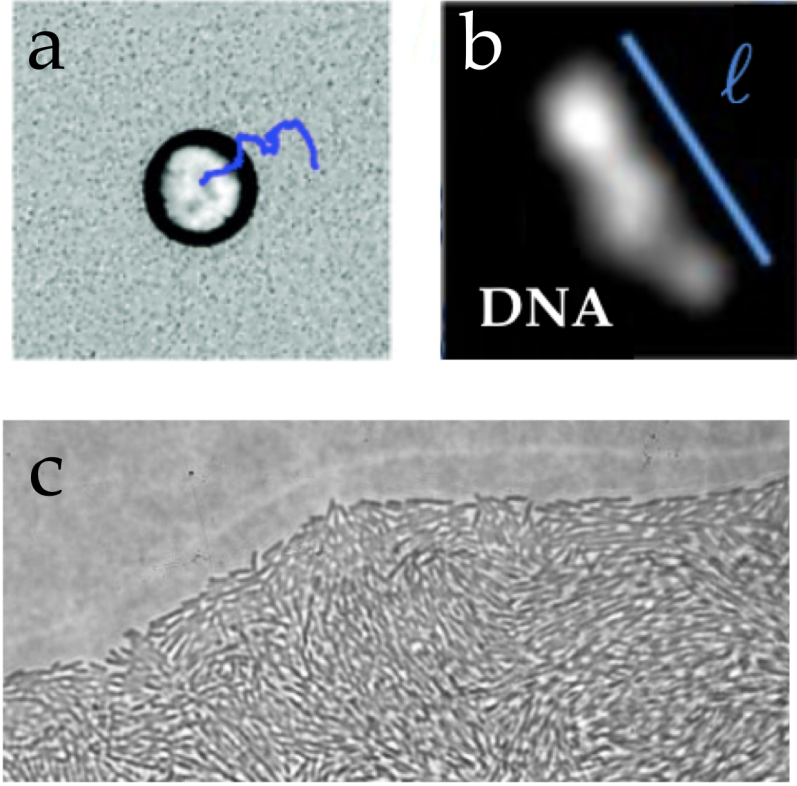


Figure 1.6: Snapshots of experimental fluids. (A) Particles: A sample trajectory of a  $39 \mu\text{m}$  bead in a suspension of *E. coli* (B) Polymers: A fluorescently stained DNA molecule with polymer end-to-end distance  $\ell$  suspended in an active environment. (C) Phases: An active phase comprised of a bacterial swarm on agar.

ing them to UV light, which immobilizes the bacteria. We find that the interface stabilizes the collective motion of the bacteria, generating larger and longer-lasting vortex structures compared to the bulk. The vortices, in return, etch the interface, setting the interface's structure and curvature. The local interface curvature correlates with the local interface velocity, suggesting an active analog of the Gibbs-Thomson boundary condition.

I conclude in Chapter 5 by summarizing the results, discussing its implications, and providing perspective.

# Bibliography

- [1] Vicsek T, Zafeiris A. 2012. **Collective Motion.** Phys Rep 517:71-140.
- [2] Gavish N, Gold G, Zangwill A, *et al.* 2015. **Glass-like dynamics in confined and congested ant traffic.** *Soft Matter* 11:6552.
- [3] H. C. Berg. 2008. ***E. coli in motion.*** Springer Science & Business Media.
- [4] Lauga E, Powers TR. 2009. **The hydrodynamics of swimming microorganisms.** *Rep Prog Phys* 72:096601.
- [5] Goldstein RE. 2015. **Green Algae as Model Organisms for Biological Fluid Dynamics.** *Ann Rev Fluid Mech.* 47:343-375.
- [6] Son D, Brumley DR, Stocker R. 2015. **Live from under the lens: exploring microbial motility with dynamic imaging and microfluidics.** *Nat Rev Micro* 13:761-775.
- [7] Howard J. 2001. **Mechanics of motor proteins and the cytoskeleton.** Sinauer Associates.
- [8] Fakhri N, Wessel AD, Willms C, *et al.* 2014. **High-resolution mapping of intracellular fluctuations using carbon nanotubes.** *Science* 344:1031-1035.
- [9] Ramaswamy S. 2010. **The Mechanics and Statistics of Active Matter.** *Ann Rev Cond Matt Phys* 1:323-345..
- [10] Marchetti MC, Joanny JF, Ramaswamy S, *et al.* 2013. **Hydrodynamics of soft active matter.** *Rev Mod Phys* 85:1143.
- [11] Dombrowski C, Cisneros L, Chatkaew S, *et al.* 2004. **Self-Concentration and Large-Scale Coherence in Bacterial Dynamics.** *Physical Review Letters* 93:098103.

- [12] Ben-Jacob E. 1997. **From snowflake formation to growth of bacterial colonies II: Cooperative formation of complex colonial patterns.** *Cont Phys* 38:205-241.
- [13] Surrey T, Nedelec R, Leibler S, Karsenti E. 2001. **Physical properties determining self-organization of motors and microtubules.** *Science* 292:1167.
- [14] Dobell C. 1932. **Antony van Leeuwenhoek and His “Little Animals”.** *London: John Bale, Sons & Danielsson.*
- [15] Czirák A, Ben-Jacob E, Cohen I, Vicsek T. 1996. **Formation of complex bacterial colonies via self-generated vortices.** *Phys Rev E* 54:2.
- [16] Toner J, Tu Y. 1998. **Flocks, herds, and schools: A quantitative theory of flocking.** *Phys Rev E* 58:4828.
- [17] Kessler JO. 1985. **Hydrodynamic focusing of motile algal cells.** *Nature* 313:218-220.
- [18] Hillesdon AJ, Pedley TJ, Kessler JO. 1995. **The development of concentration gradients in a suspension of chemotactic bacteria.** *Bull Math Biol* 57:299-344.
- [19] Tuval I, Cisneros L, Dombrowski C, *et al.* 2004. **Bacterial swimming and oxygen transport near contact lines.** *Proceedings of the National Academy of Sciences* 102:2277-2282.
- [20] Deseigne J, Dauchot O, Chaté H, 2010. **Collective Motion of Vibrated Polar Disks.** *Physical Review Letters* 105:098001.
- [21] Narayan V, Ramaswamy S, Menon N. 2007. **Long-Lived Giant Number Fluctuations in a Swarming Granular Nematic.** *Science* 317:105-108.
- [22] Bricard A, Caussin JB, Desreumaux N, *et al.* 2013. **Emergence of macroscopic directed motion in populations of motile colloids.** *Nature* 503:95-98.
- [23] Masoud H, Bingham BI, Alexeev A. 2012. **Designing maneuverable micro-swimmers actuated by responsive gel.** *Soft Matter* 8:8944-8951.
- [24] Aranson I. 2013. **Active Colloids.** *Physics-Uspexhi* 56:79-92.
- [25] Wu XL, Libchaber A. 2000. **Particle Diffusion in a Quasi-Two-Dimensional Bacterial Bath.** *Physical Review Letters* 84:3017.

- [26] Wong D, Beattie EE, Steager EB, Kumar V. 2013. **Effect of surface interactions and geometry on the motion of microbio robots.** *Applied Physics Letters* 103:153707.
- [27] Sokolov A, Apodaca MM, Grzybowski BA, Aranson IS. 2009. **Swimming bacteria power microscopic gears.** *Proceedings of the National Academy of Sciences* 107:969-74.
- [28] Di Leonardo R, Angelani L, Dell’Acriprete D, *et al.* 2010 **Bacterial ratchet motors.** *Proceedings of the National Academy of Sciences* 107:9541-9545.
- [29] Turner L, Ryu WS, Berg HC. 2000. **Real-time imaging of fluorescent flagellar filaments.** *J Bacteriol* 182:2793-2801.
- [30] Sznitman J, Shen X, Sznitman R, Arratia PE. 2010. **Propulsive force measurements and flow behavior of undulatory swimmers at low Reynolds number.** *Physics of Fluids* 22:121901.
- [31] Ben-Jacob E, Levine H. 2001. **The artistry of nature.** *Nature* 409:985-986.
- [32] Fisher HS, Giomi L, Hoekstra HC, Mahadevan L. 2004. **The dynamics of sperm cooperation in a competitive environment.** *Proc Roy Soc London* 281:20140296.
- [33] Tottori S, Zhang L, Peyer KE, Nelson BJ. 2013. **Assembly, Disassembly, and Anomalous Propulsion of Microscopic Helices.** *Nano Lett* 13:4263-4268.
- [34] Dreyfus R, Baudry J, Roper ML, *et al.* 2005. **Microscopic artificial swimmers.** *Nature* 37:862-865.
- [35] Sanchez T, Welch D, Nicastro D, Dogic Z. 2011. **Cilia-Like Beating of Active Microtubule Bundles.** *Science* {333:456-459.
- [36] Snezhko A, Belkin M, Aranson IS, Kwok WK. 2009. **Self-Assembled Magnetic Surface Swimmers.** *Physical Review Letters* 102:118103.
- [37] Josenhans C, Suerbaum W. 2002. **The role of motility as a virulence factor in bacteria.** *Int J Med Microbiol* 291:605-614.
- [38] Costerton JW, Stewart PS, Greenberg EP. 1999. **Bacterial biofilms: A common cause of persistent infections.** *Science* 284:1318-1322.
- [39] Gao W, Wang J. 2014. **Synthetic micro/nanomotors in drug delivery.** *Nanoscale* 6:10486.

- [40] Nelson BJ, Kaliakatsos IK, Abbott JJ. 2013. **Microrobots for minimally invasive medicine.** *Annu Rev Biomed Eng* 12:55-85.
- [41] Bixler GD, Bhushan B. 2012. **Biofouling: Lessons from nature.** *Phil. Trans. R. Soc. A* 370:2381-2417.
- [42] Kessler JD, Valentine DL, Redmond MC, *et al.* 2011. **A Persistent Oxygen Anomaly Reveals the Fate of Spilled Methane in the Deep Gulf of Mexico.** *Science* 331:312.
- [43] Cisneros CH, Cortez R, Dombrowski C, *et al.* 2007. **Fluid dynamics of self-propelled microorganisms, from individuals to concentrated populations.** *Exp Fluids* 43:737-753.
- [44] Wensink HH, Dunkel J, Heidenreich S, *et al.* 2012. **Meso-scale turbulence in living fluids.** *Proceedings of the National Academy of Sciences* 109:14308-14313.
- [45] Sokolov A, Aranson IS. 2009. **Reduction of Viscosity in Suspension of Swimming Bacteria.** *Physical Review Letters* 103:148101.
- [46] Rafai S, Peyla P, Levan J. 2010. **Effective Viscosity of Microswimmer Suspensions.** *Physical Review Letters* 104:098102.
- [47] López HML, Gachelin J, Douarche C, *et al.* 2015. **Turning Bacteria Suspensions into Superfluids.** *Physical Review Letters* 115:028301.
- [48] Darnton N, Turner L, Breuer K, Berg HC. 2004. **Moving fluid with bacterial carpets.** *Biophys J* 86:1863-1870.
- [49] Kurtuldu H, Guasto JS, Johnson KA, Gollub JP. 2010. **Enhancement of biomixing by swimming algal cells in two-dimensional films.** *Proceedings of the National Academy of Sciences* 108:10391.
- [50] Brady JF, Bossis G. 1988. **Stokesian Dynamics.** *Ann Rev Fluid Mech* 20:111-57.
- [51] Squires TM, Mason TG. 2009. **Fluid mechanics of microrheology.** *Ann Rev Fluid Mech* 2:413.
- [52] Keim NC, Arratia PE. 2013. **Yielding and microstructure in a 2D jammed material under shear deformation.** *Soft Matter* 9: 6222-6225.

- [53] Keim NC, Arratia PE. 2014. **Mechanical and Microscopic Properties of the Reversible Plastic Regime in a 2D Jammed Material.** *Physical Review Letters* 112:028302.
- [54] Martinez VA, Schwarz-Linek J, Reufer M, *et al.* 2014. **Flagellated bacterial motility in polymer solutions.** *Proceedings of the National Academy of Sciences* 111:17771-17776.
- [55] Qin B, Gopinath A, Yang J, *et al.* 2015. **Flagellar Kinematics and Swimming of Algal Cells in Viscoelastic Fluids.** *Scientific Reports* 5:19190.
- [56] Park JA, Kim JH, Bi D, *et al.* 2015. **Unjamming and cell shape in the asthmatic airway epithelium.** *Nat Mat* 14:1040-1048.
- [57] Purcell EM. 1977. **Life at low Reynolds number.** *Am J Phys* 45:3.
- [58] Watari N, Larson RG. 2010. **The Hydrodynamics of a Run-and-Tumble Bacterium Propelled by Polymorphic Helical Flagella.** *Biophys J* 98:12-17.
- [59] Guasto JS, Johnson KA, Gollub JP. 2010. **Oscillatory Flows Induced by Microorganisms Swimming in Two Dimensions.** *Physical Review Letters* 105:168102.
- [60] Drescher K, Dunkel J, Cisneros LH, *et al.* 2011. **Fluid dynamics and noise in bacterial cell - cell and cell - surface scattering.** *Proceedings of the National Academy of Sciences* 108:10940-10945.
- [61] Drescher K, Goldstein RE, Michel M, *et al.* 2010. **Direct Measurement of the Flow Field around Swimming Microorganisms.** *Physical Review Letters* 105:168101.
- [62] Tam D, Hosoi AE. 2011. **Optimal feeding and swimming gaits of biflagellated organisms.** *Proceedings of the National Academy of Sciences* 108:1001-1006.
- [63] Taylor G. 1951. **Analysis of the Swimming of Microscopic Organisms.** *Roy Soc* 209:447-461.
- [64] Was L, Lauga E. 2014. **Optimal propulsive flapping in Stokes flows.** *Bioinspir. Biomim.* 9:016001.
- [65] Patteson AE, Gopinath A, Goulian M, Arratia P. 2015. **Running and tumbling with *E. coli* in polymeric solutions.** *Scientific Reports* 5:15761.

- [66] Keim NC, Garcia M, Arratia PE, 2012. **Fluid elasticity can enable propulsion at low Reynolds number.** *Physics of Fluids* 24:95-98.
- [67] Gagnon DA, Keim NC, Arratia PE. Undulatory swimming in shear-thinning fluids: experiments with *Caenorhabditis elegans*. *J Fluid Mech* 2014;758:R3.
- [68] Fauci LJ, Dillon R. 2006. **Biofluidmechanics of reproduction.** *Ann Rev Fluid Mech* 38:371-394.
- [69] Gagnon DA, Keim NC, Shen X, Arratia PE. 2014. **Fluid-induced propulsion of rigid particles in wormlike micellar solutions.** *Physics of Fluids* 26:103101 .
- [70] Thomases B, Guy RD. 2014. **Mechanisms of elastic enhancement and hindrance for finite length undulatory swimmers in viscoelastic fluids.** *Physical Review Letters* 113:098102.
- [71] Spagnolie SE, Liu B, Powers TR. 2013. **Locomotion of Helical Bodies in Viscoelastic Fluids: Enhanced Swimming at Large Helical Amplitudes.** *Physical Review Letters* 111:068101.
- [72] Espinosa-Garcia J, Lauga E, Zenit R. 2013. **Fluid elasticity increases the locomotion of flexible swimmers.** *Physics of Fluids* 25:031701.
- [73] Lauga E. 2007. **Propulsion in a viscoelastic fluid.** *Physics of Fluids* 19:083104.
- [74] Fu HC, Powers TR, Wolgemuth CW. 2007. **Theory of swimming filaments in viscoelastic media.** *Physical Review Letters* 99:258101.
- [75] Shen XN, Arratia PE. 2011. **Undulatory Swimming in Viscoelastic Fluids.** *Physical Review Letters* 106:208101.
- [76] Teran J, Fauci L, Shelley M. 2010. **Fluid elasticity can enable propulsion at low Reynolds number.** *Physical Review Letters* 104:038101.
- [77] Liu B, Powers TR, Breuer KS. 2011. **Force-free swimming of a model helical flagellum in viscoelastic fluids.** *Proceedings of the National Academy of Sciences* 108:19516-19520.
- [78] Saintillan D, Shelley MJ. 2011. **Emergence of coherent structures and large-scale flows in motile suspensions.** *J Roy Soc Interf* rsif20110355.

- [79] Ardekani AM, Gore E. 2012. **Emergence of a limit cycle for swimming microorganisms in a vortical flow of a viscoelastic fluid.** *Phys Rev E* 85:056309.
- [80] Drescher K, Shen Y, Bassler BL, Stone HA. 2013. **Biofilm streamers cause catastrophic disruption of flow with consequences for environmental and medical systems.** *Proceedings of the National Academy of Sciences* 110:4345-4350.
- [81] Schwarz-Linek J, Valeriani C, Cacciuto A, *et al.* 2012. **Phase separation and rotor self-assembly in active particle suspensions.** *Proceedings of the National Academy of Sciences* 109:4052-4057.
- [82] DeCamp SJ, Redner GS, Baskaran A, *et al.* 2015. **Orientational order of motile defects in active nematics.** *Nat Mat.*
- [83] Takagi D, Palacci J, Braunschweig A, *et al.* 2014. **Hydrodynamic capture of microswimmers into sphere-bound orbits.** *Soft Matter* 10:1784-1789.
- [84] Koumakis N, Lepore A, Maggi C, R. Di Leonardo R. 2013. **Targeted delivery of colloids by swimming bacteria.** *Nat Comm* 4:2588.
- [85] Einstein A. 1906. **A new determination of molecular dimensions.** *Ann Phys* 19:289-306.
- [86] Saintillan D. 2010. **The Dilute Rheology of Swimming Suspensions: A Simple Kinetic Model.** *Exp Mech* 50:1275-1281.
- [87] McDonnell AG, Gopesh TC, Lo J, *et al.* 2015. **Motility induced changes in viscosity of suspensions of swimming microbes in extensional flows.** *Soft Matter* 11:4658-4668.
- [88] Saintillan D. 2010. **Extensional rheology of active suspensions.** *Phys Rev E* 81:056307.
- [89] Zhou S, Sokolov A, Lavrentovich OD, Aranson IS. 2013. **Living liquid crystals.** *Proceedings of the National Academy of Sciences* 111:1265-1270.
- [90] Mushenheim PC, Trivedi RR, Roy SS, *et al.* 2015. **Effects of confinement, surface-induced orientations and strain on dynamical behaviors of bacteria in thin liquid crystalline films.** *Soft Matter* 11:6821.
- [91] Trivedi RR, Maeda R, Abbott NL, *et al.* 2015. **Bacterial transport of colloids in liquid crystalline environments.** *Soft Matter* DOI:10.1039/C5SM02041G.



- [92] Koch DL, Subramanian G. 2011. **Collective Hydrodynamics of Swimming Microorganisms: Living Fluids.** *Annu Rev Fluid Mech* 43:637-59.
- [93] Hatwalne Y, Ramaswamy S, Rao M, Aditi Simha R. 2004. **Rheology of Active-Particle Suspensions.** *Physical Review Letters* 92:118101.

# Chapter 2

## Particle dynamics in active fluids: The role of particle size on particle diffusion in aqueous *E. coli* suspensions.

### 2.1 Introduction

The diffusion of molecules and particles in a fluid is a process that permeates many aspects of our lives including fog formation in rain or snow [1], cellular respiration [2], and chemical distillation processes [3]. At equilibrium, the diffusion of colloidal particles in a fluid is driven by thermal motion and damped by viscous resistance [4]. In non-equilibrium systems, fluctuations are no longer only thermal and the link between these fluctuations and particle dynamics remain elusive [5]. Much effort has been devoted to understanding particle dynamics in non-equilibrium systems, such as glassy materials and sheared granular matter [6]. A non-equilibrium system of emerging interest is active matter. Active matter includes active fluids, that is, fluids that contain self-propelling particles, such as motile microorganisms [7, 24], catalytic colloids [9, 11] and molecular motors [11]. These

particles inject energy, generate mechanical stresses, and create flows within the fluid medium even in the absence of external forcing [12,13]. Consequently, active fluids display fascinating phenomena not seen in passive fluids, such as spontaneous flows [24], anomalous shear viscosities [7,14], unusual polymer swelling [15,16], and enhanced fluid mixing [2,4,8,19]. Active fluids also play important roles in varied biological and ecological settings, which include the contributions of suspensions of microorganisms to biofilm infections [21,22], biofouling of water-treatment systems [23], and biodegradation of environmental pollutants [24].

The motion of passive particles in active fluids (e.g. suspension of swimming microorganisms) can be used to investigate the non-equilibrium properties of such fluids. At short times, particle displacement distributions can exhibit extended non-Gaussian tails. At long times, particles exhibit enhanced diffusivities  $D_{\text{eff}}$  greater than their thermal (Brownian) diffusivity  $D_0$  [2,2,4,4,8–10,19,25]. These traits are a signature of the non-equilibrium nature of active fluids; the deviation from equilibrium also manifests in violations of the fluctuation dissipation theorem [28].

In bacterial suspensions, the enhanced diffusivity  $D_{\text{eff}}$  depends on the concentration  $c$  of bacteria. In their seminal work, Wu and Libchaber [25] experimentally found that  $D_{\text{eff}}$  increased linearly with  $c$  in suspensions of *E. coli*. Subsequent studies [7,9,10,29–31] have observed that this scaling holds at low concentrations and in the absence of collective motion. In this regime,  $D_{\text{eff}}$  can be decomposed into additive components as  $D_{\text{eff}} = D_0 + D_A$  [7,9,10,29–31] where  $D_0$  and  $D_A$  are the thermal and active diffusivities, respectively. It has been proposed that the active diffusivity  $D_A$  is a consequence of advection due to far-field interactions with bacteria [9] and may even be higher near walls [9,10].

While a majority of studies have focused on the role of bacterial concentration  $c$  on particle diffusion, the role of particle diameter  $d$  remains unclear. In the absence of bacteria, the diffusivity of a sphere follows the Stokes-Einstein relation,  $D_0 = k_B T / f_0$ , where  $k_B$  is the Boltzmann constant,  $T$  is the temperature, and  $f_0 = 3\pi\mu d$  is the Stokes friction factor [4] in a fluid of viscosity  $\mu$ . In a bacterial suspension, this relation is no longer expected to be valid. Surprisingly, for large particles (4.5 and 10  $\mu\text{m}$ ), Wu and Libchaber [25] suggested that  $D_{\text{eff}}$  scales as  $1/d$ , as in passive fluids. Recent theory and simulation by Kasyap *et al.* [7] however do not support the  $1/d$  scaling and instead predict a non-trivial dependence of  $D_{\text{eff}}$  on particle size, including a peak in  $D_{\text{eff}}$ . This non-monotonic dependence of  $D_{\text{eff}}$  on particle size implies that measures of effective diffusivities [25], effective temperatures [12,33], and momentum flux [9,10] intimately depend on the probe size and thus are not universal

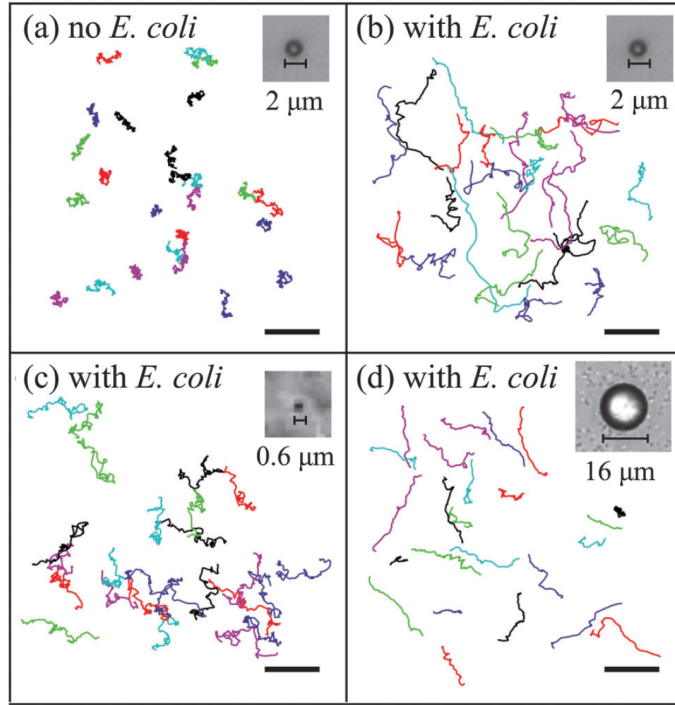


Figure 2.1: Trajectories of 2  $\mu\text{m}$  particles (a) without bacteria and (b) with bacteria ( $c = 3 \times 10^9$  cells/mL) for time interval 8 s. Trajectories of (c) 0.6 and (d) 16  $\mu\text{m}$  particles ( $c = 3 \times 10^9$  cells/mL). Scale bar is 20  $\mu\text{m}$ .

measures of activity. This has important implications for the common use of colloidal probes in gauging and characterizing the activity of living materials, such as suspensions of bacteria [9, 10], biofilms [11, 34], and the cytoskeletal network inside cells [36], as well as in understanding transport in these biophysical setting. Despite the ubiquity of passive particles in active environments, the effects of size on particle dynamics in active fluids has yet to be systematically investigated in experiments.

In this chapter, I experimentally investigate the effects of particle size  $d$  on the dynamics of passive particles in suspensions of *Escherichia coli*. *Escherichia coli* [37] are model organisms for bacterial studies and are rod-shaped cells with 3 to 4 flagella that bundle together as the cell swims forward at speed  $U$  approximately  $10\text{ }\mu\text{m/s}$ . I change the particle size  $d$  from  $0.6\text{ }\mu\text{m}$  to  $39\text{ }\mu\text{m}$ , above and below the effective total length ( $L \approx 7.6\text{ }\mu\text{m}$ ) of the *E. coli* body and flagellar bundle. I find that  $D_{\text{eff}}$  is non-monotonic in  $d$ , with a peak at  $2 < d < 10\text{ }\mu\text{m}$ ; this non-monotonicity is unlike the previously found  $1/d$  scaling [25] and suggests that larger particles can diffuse faster than smaller particles in active fluids. Furthermore, the existence and position of the peak can be tuned by varying the bacterial concentration  $c$ . The active diffusion  $D_A = D_{\text{eff}} - D_0$  is also a non-monotonic function of  $d$  and can be collapsed into a master curve when rescaled by the quantity  $cUL^4$  and plotted as a function of the Péclet number  $\text{Pe} = UL/D_0$  (*cf.* Fig. 2.5(b)). This result suggests that the active contribution to particle diffusion can be encapsulated by an universal dimensionless dispersivity  $\bar{D}_A$  that is set by the ratio of times for the particle to thermally diffuse a distance  $L$  and a bacterium to swim a distance  $L$ .

## 2.2 Experimental Methods

Active fluids are prepared by suspending spherical polystyrene particles and swimming *E. coli* (wild-type K12 MG1655) in a buffer solution (67 mM NaCl in water). The *E. coli* are prepared by growing the cells to saturation ( $10^9$  cells/mL) in culture media (LB broth, Sigma-Aldrich). The saturated culture is gently cleaned by centrifugation and resuspended in the buffer. The polystyrene particles (density  $\rho = 1.05\text{ g/cm}^3$ ) are cleaned by centrifugation and then suspended in the buffer-bacterial suspension, with a small amount of surfactant (Tween 20, 0.03% by volume). The particle volume fractions  $\phi$  are below 0.1% and thus considered dilute. The *E. coli* concentration  $c$  ranges from  $0.75$  to  $7.5 \times 10^9$  cells/mL. These concentrations are also considered dilute, corresponding to volume

fractions  $\phi = cv_b < 1\%$ , where  $v_b$  is the volume [9] of an *E. coli* cell body ( $1.4 \mu\text{m}^3$ ).

A  $2 \mu\text{l}$  drop of the bacteria-particle suspension is stretched into a fluid film using an adjustable wire frame [2, 7, 38] to a measured thickness of approximately  $100 \mu\text{m}$ . The film interfaces are stress-free, which minimizes velocity gradients transverse to the film. I do not observe any large scale collective behavior in these films; the *E. coli* concentrations I use are below the values for which collective motion is typically observed [7] ( $\approx 10^{10}$  cells/ml). Particles of different diameters ( $0.6 \mu\text{m} < d < 39 \mu\text{m}$ ) are imaged in a quasi two-dimensional slice ( $10 \mu\text{m}$  depth of focus). I consider the effects of particle sedimentation, interface deformation, and confinement on particle diffusion and find that they do not significantly affect my measurements of effective diffusivity in the presence of bacteria (for more details, please see Appendix A.1). Images are taken at 30 frames per second using a 10X objective (NA 0.45) and a CCD camera (Sony XCDSX90), which is high enough to observe correlated motion of the particles in the presence of bacteria (Fig. 2.2) but small enough to resolve spatial displacements. Particles less than  $2 \mu\text{m}$  in diameter are imaged with fluorescence microscopy (red, 589 nm) to clearly visualize particles distinct from *E. coli* ( $2 \mu\text{m}$  long). I obtain the particle positions in two dimensions over time using particle tracking methods [38, 39]. All experiments are performed at  $T_0 = 22^\circ\text{C}$ .

## 2.3 Results and Discussion

### 2.3.1 Mean Square Displacements

Representative trajectories of passive particles in the absence and presence of *E. coli* are shown in Fig. 2.1 for a time interval of 8 s. By comparing Fig. 2.1(a) (no *E. coli*) to Fig. 2.1(b) ( $c = 3 \times 10^9$  cells/mL), I readily observe that the presence of bacteria enhances the magnitude of particle displacements compared to thermal equilibrium. Next, I compare sample trajectories of passive particles of different sizes  $d$ , below and above the *E. coli* total length  $L \approx 7.6 \mu\text{m}$ . Figure 2.1(c) and 2.1(d) show the magnitude of particle displacement for  $d = 0.6 \mu\text{m}$  and  $d = 16 \mu\text{m}$ , respectively. Surprisingly, I find that the particle mean square displacements in the *E. coli* suspension are relatively similar for the two particle sizes even though the thermal diffusivity  $D_0$  of the  $0.6 \mu\text{m}$  particle is 35 times larger than that of the  $16 \mu\text{m}$  particle. The  $16 \mu\text{m}$  particles also appear to be correlated for longer times than the  $0.6 \mu\text{m}$  particles. These observations point to a non-trivial

dependence of particle diffusivity on  $d$ .

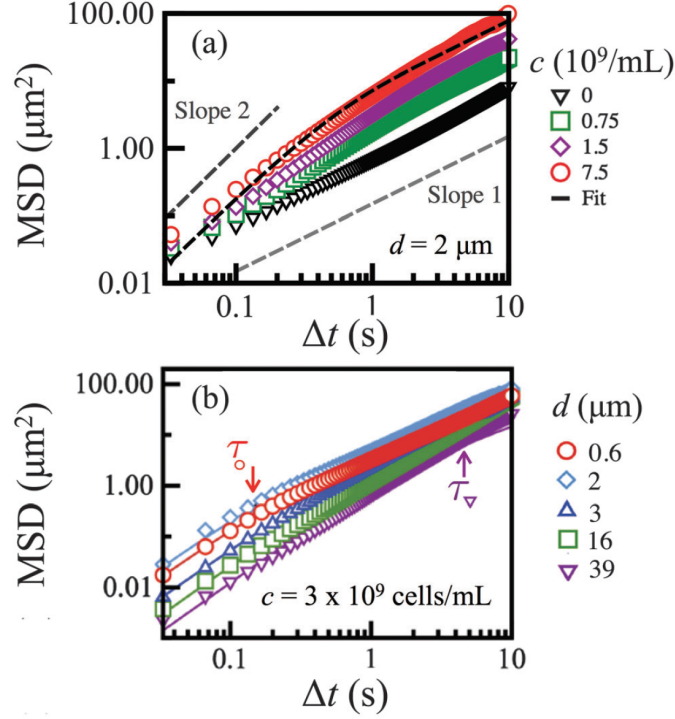


Figure 2.2: (a) Mean-square displacements (MSD) of  $2 \mu\text{m}$  particles versus time  $\Delta t$  for varying bacterial concentration  $c$ . Dashed line is a fit to Langevin dynamics (eqn (2.1)). (b) MSD for varying particle diameter  $d$  versus time for bacterial concentration  $c = 3.0 \times 10^9 \text{ cells/mL}$ . The MSD peaks at  $d = 2 \mu\text{m}$ . The cross-over time  $\tau$  (arrows) increases with  $d$ . Solid lines are Langevin dynamics fits.

To quantify the above observations, I measure the mean-squared displacement (MSD) of the passive particles for varying *E. coli* concentration  $c$  (Fig. 2.2(a)) and particle size  $d$  (Fig. 2.2(b)). Here, I define the mean-squared particle displacement as  $\text{MSD}(\Delta t) = \langle |\mathbf{r}(t_R + \Delta t) - \mathbf{r}(t_R)|^2 \rangle$ , where the brackets denote an ensemble average over particles and reference times  $t_R$ . For a particle executing a random walk in two dimensions, the MSD exhibits a characteristic cross-over time  $\tau$ , corresponding to the transition from an initially ballistic regime for  $\Delta t \ll \tau$  to a diffusive regime with  $\text{MSD} \sim 4D_{\text{eff}}\Delta t$  for  $\Delta t \gg \tau$ .

Figure 2.2(a) shows the MSD data for  $2 \mu\text{m}$  particles at varying bacterial concentrations  $c$ . In the absence of bacteria ( $c = 0 \text{ cells/mL}$ ), the fluid is at equilibrium and  $D_{\text{eff}} = D_0$ . For this case, I am unable to capture the crossover from ballistic to diffusive dynamics due to the lack of resolution:

for colloidal particles in water, for example, cross-over times are on the order of nanoseconds and challenging to measure [40]. Experimentally, the dynamics of passive particles at equilibrium are thus generally diffusive at all observable time scales. I fit the MSD data for the  $d = 2 \mu\text{m}$  case (with no bacteria) to the expression  $\text{MSD} = 4D_0\Delta t$ , and find that  $D_0 \approx 0.2 \mu\text{m}^2/\text{s}$ . This matches the theoretically predicted value from the Stokes-Einstein relation; the agreement ( $\nabla$ ) can be visually inspected in Fig. 2.3(a).

In the presence of *E. coli*, the MSD curves exhibit a ballistic to diffusive transition, and I find that the cross-over time  $\tau$  increases with  $c$ . For  $\Delta t \gg \tau$ , the  $\text{MSD} \sim \Delta t$  with a long-time slope that increases with bacteria concentration  $c$ . Additionally, the distribution of particle displacements follows a Gaussian distribution (see Appendix A.2 for details and measures of the non-Gaussian parameter). These features,  $\text{MSD} \sim \Delta t$  and Gaussian displacements, indicate that the long-time dynamics of the particles in the presence of *E. coli* is diffusive and can be captured by a physically meaningful effective diffusion coefficient  $D_{\text{eff}}$ .

I next turn our attention to the effects of particle size. For varying particle diameter  $d$  at a fixed bacterial concentration ( $c = 3 \times 10^9$  cells/ml), the MSD curves also exhibit a ballistic to diffusive transition, as shown in Fig. 2.2(b). Surprisingly, I find a non-monotonic behavior with  $d$ . For example, the MSD curve for the  $2 \mu\text{m}$  case sits higher than the  $39 \mu\text{m}$  case and the  $0.6 \mu\text{m}$  case. This trend is not consistent with classical diffusion in which MSD curves are expected to decrease monotonically with  $d$  ( $D_0 \propto 1/d$ ). I also observe that the cross-over time  $\tau$  increases monotonically with  $d$ . As I will discuss later in the chapter, the cross-over time scaling with  $d$  also deviates from classical diffusion.

### 2.3.2 Diffusivity and Cross-over Times

I now estimate the effective diffusivities  $D_{\text{eff}}$  and cross-over times  $\tau$  of the passive particles in the bacterial suspensions. To obtain  $D_{\text{eff}}$  and  $\tau$ , I fit the MSD data shown in Fig. 2.2 to the MSD expression attained from the generalized Langevin equation [6], that is

$$\text{MSD}(\Delta t) = 4D_{\text{eff}}\Delta t \left( 1 - \frac{\tau}{\Delta t} \left( 1 - e^{-\frac{\Delta t}{\tau}} \right) \right). \quad (2.1)$$

Equation 1 has been used previously to interpret the diffusion of bacteria [16] as well as the diffusion



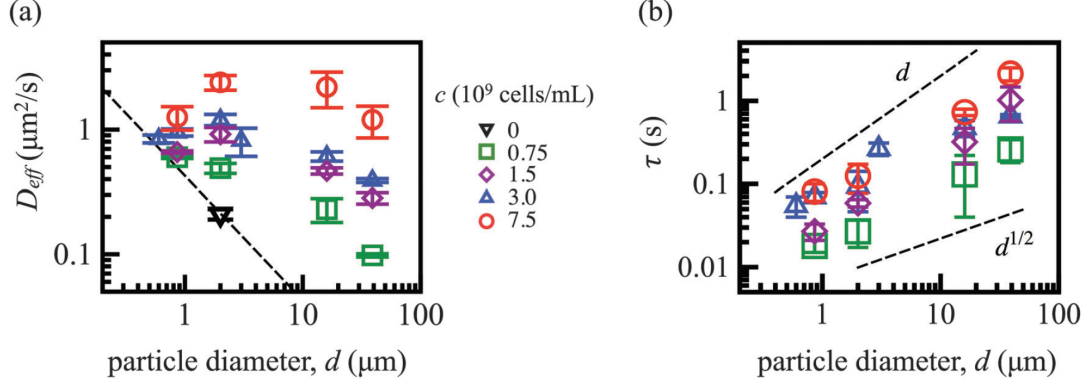


Figure 2.3: (a) Effective particle diffusivities  $D_{\text{eff}}$  versus particle diameter  $d$  at varying  $c$ . The dashed line is particle thermal diffusivity  $D_0$ . (b) The crossover-time  $\tau$  increases with  $d$ , scaling as approximately  $d^n$ , where  $1/2 \lesssim n \lesssim 1$ . This is not the scaling in passive fluids [6] where  $\tau \propto d^2$ .

of particles in films with bacteria [11]. In the limit of zero bacterial concentration,  $D_A = 0$  and eqn (2.1) reduces to the formal solution to the Langevin equation for passive fluids,  $\text{MSD}(\Delta t) = 4D_0\Delta t \left(1 - \frac{\tau_0}{\Delta t} (1 - e^{-\Delta t/\tau_0})\right)$  with  $\tau_0 = \tau(c = 0)$ . For more details on the choice of model, see Appendix A.3.

Figure 2.3 shows the long-time particle diffusivity  $D_{\text{eff}}$  (Fig. 2.3(a)) and the cross-over time  $\tau$  (Fig. 2.3(b)) as a function of  $d$  for bacterial concentrations  $c = 0.75, 1.5, 3.0$  and  $7.5 \times 10^9$  cells/mL. I find that for all values of  $d$  and  $c$  considered here,  $D_{\text{eff}}$  is larger than the Stokes-Einstein values  $D_0$  at equilibrium (dashed line). For the smallest particle diameter case ( $d = 0.6 \mu\text{m}$ ),  $D_{\text{eff}}$  nearly matches  $D_0$ . This suggests that activity-enhanced transport of small ( $d \lesssim 0.6 \mu\text{m}$ ) particles or molecules such as oxygen, a nutrient for *E. coli*, may be entirely negligible [7]. For more information, including figures illustrating the dependence of  $D_{\text{eff}}$  on  $c$  and comparisons between my measured effective diffusivities and previous experimental work, see sections Appendix A.2.4 and Appendix A.2.3 in the supplemental materials.

Figure 2.3(a) also reveals a striking feature: a peak  $D_{\text{eff}}$  in  $d$ . My data demonstrates that, remarkably, larger particles can diffuse faster than smaller particles in suspensions of bacteria. For example, at  $c = 7.5 \times 10^9$  cells/mL ( $\circ$ ) the  $2 \mu\text{m}$  particle has an effective diffusivity of approximately  $2.0 \mu\text{m}^2/\text{s}$ , which is nearly twice as high as the effective diffusivity of the  $0.86 \mu\text{m}$  particle,  $D_{\text{eff}} = 1.3 \mu\text{m}^2/\text{s}$ . I also observe that the peak vanishes as  $c$  decreases. For the lowest bacterial concentration ( $c = 0.75 \times 10^9$  cells/mL), there is no peak:  $D_{\text{eff}}$  decreases monotonically with  $d$ . Clearly,  $D_{\text{eff}}$  does

not scale as  $1/d$ .

Figure 2.3(b) shows the cross-over times  $\tau$  characterizing the transition from ballistic to diffusive regimes as a function of particle size  $d$  for varying  $c$ . I find that the values of  $\tau$  increase with  $d$  and  $c$ . I note that the variation of  $\tau$  with  $c$  (Figure A.3 in Appendix) does not follow a linear form. Instead, the data suggests possible saturation of  $\tau$  for suspensions of higher – but still dilute – concentrations. The cross-over time  $\tau$  scales with particle diameter approximately as  $\tau \sim d^n$ , where  $\frac{1}{2} \lesssim n \lesssim 1$ . This cross-over time does not correspond to the inertial relaxation of the particle. Therefore, this scaling does not follow the trend seen for passive particles at thermal equilibrium [6], where  $\tau$ , being the Stokes relaxation time (order 1 ns), scales as  $m/f_0 \propto d^2$  with particle mass  $m \propto d^3$ . The data (Fig. 2.3(b)) highlights that in active fluids the super-diffusive motion of the passive particles cannot be ignored – even for time scales as large as a second – and that the time scales over which diffusive motion is valid ( $\Delta t > \tau$ ) depends on the size  $d$  of the particle. Further implications of a particle size-dependent cross-over time will be discussed below.

### 2.3.3 Effective Temperature

The data so far suggests that particle dynamics in bacterial suspensions, while having an anomalous size-dependence (Figs. 2.1,2.2,2.3), maintain the characteristic super-diffusive to diffusive dynamics for passive fluids [6]. The long-time diffusive behavior (Fig. 2.2) and enhancement in  $D_{\text{eff}}$  (Fig. 2.3(a)), which is rooted in particle-bacteria encounters, suggest that the particles behave as if they are suspended in a fluid with an effectively higher temperature.

To explore the concept of effective temperature in bacterial suspensions, I measure the distribution of particle speeds  $p(v)$  as a function of bacterial concentration  $c$ . The particle speed distributions determine the mean kinetic energy of the particles. If the distribution follows a Maxwell Boltzmann form – as is always the case in fluids at equilibrium – the mean kinetic energy is related to the thermodynamic temperature via the equipartition theorem. Such a relationship may not always exist for out-of-equilibrium fluids.

Figure 2.4(a) shows  $p(v)$  for  $d = 2 \mu\text{m}$  case for a range of  $c$ . I define the particle speeds  $v$  over a time interval of 0.5 s. This time interval is greater than the crossover times for the  $2 \mu\text{m}$  particles (*cf.* Appendix Figure A.3) to ensure that a particle samples multiple interactions with bacteria and exhibits diffusive behavior. In the absence of bacteria, the system is in thermal equilibrium and  $p(v)$

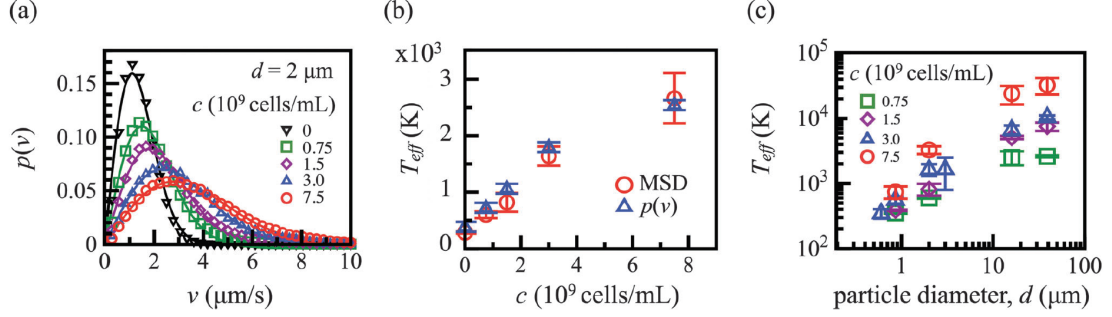


Figure 2.4: (a) Distribution of  $2 \mu\text{m}$  particle speeds  $p(v)$  follow a Maxwell-Boltzmann distribution (solid curves) with clear peaks that shift right as  $c$  increases. (b) The effective temperature  $T_{\text{eff}}$  extracted by fitting  $p(v)$  data to eqn (2.2) ( $\Delta$ ) matches those obtained from an extended Stokes-Einstein relation ( $\circ$ ). (c) The effective temperature  $T_{\text{eff}}$  increases with  $d$  for varying  $c$ .

follows the two dimensional Maxwell-Boltzmann distribution,

$$p(v) = vm(k_B T_{\text{eff}})^{-1} e^{\frac{-mv^2}{2k_B T_{\text{eff}}}}, \quad (2.2)$$

with peak speeds  $v_{\text{max}} = \sqrt{2k_B T_{\text{eff}}/m}$ , where  $m$  is the mass of the polystyrene particle. Fitting the  $p(v)$  data in the absence of bacteria ( $\nabla$  in Fig. 2.4(a)) to eqn (2.2) yields  $T_{\text{eff}} \approx T_0$ , as expected.

In the presence of bacteria, the particle speed distributions also follow a Maxwell-Boltzmann form, eqn (2.2), with peaks that shift toward higher values of  $v$  as the *E. coli* concentration  $c$  increases. Because the data follows the Maxwell-Boltzmann form (Fig. 2.4(a)) for all  $c$ , this indicates that there is no correlated motion at long times as is the case in swarming bacterial suspensions, for which the particle speed distributions exhibits an exponential decay [42]. I also note that the power spectra of particle speeds (Appendix A.2.4) are reasonably flat, consistent with white-noise forcing and an absence of correlated motion. Figure 2.4(a) thus indicates that an effective temperature  $T_{\text{eff}}$  can be defined from  $p(v)$  and is increasing with the bacterial concentration.

To quantify this ‘enhanced’ temperature and the deviation from equilibrium behavior, I fit the  $p(v)$  data (Fig. 2.4(a)) to eqn (2.2). These fits allow us to obtain  $T_{\text{eff}}$  as a function of  $c$ , as shown in Fig. 2.4(b) ( $\Delta$ ). Also shown in Fig. 2.4(b) are the values extracted of  $T_{\text{eff}}$  ( $\circ$ ) from an extended Stokes-Einstein relation,  $T_{\text{eff}} = 3\pi\mu d D_{\text{eff}}/k_B$ , where  $D_{\text{eff}}$  are the values from the MSD fits shown in Fig. 2.3(a) and  $\mu$  is the viscosity of the solvent ( $\mu \approx 1 \text{ mPa s}$ ). I find that both estimates of  $T_{\text{eff}}$  are higher than room temperature  $T_0$  and increase linearly with  $c$ .

For a fluid at equilibrium, the temperatures from these two methods, MSD and  $p(v)$ , are expected

to be the same but not for systems that are out of equilibrium [5, 6, 43, 44], such as the bacterial suspensions investigated here. The good agreement in Fig. 2.4(b) suggests that  $T_{\text{eff}}$  may be a useful signature of bacterial activity with some analogies to equilibrium systems. Note that in defining the effective temperature via the generalized Stokes-Einstein relation, I have assumed the viscosity to be a constant and independent of bacterial concentration, which may not be true when the bacterial concentrations are sufficiently high [45]. Figure 2.4(b) suggests that an unchanging viscosity is a valid assumption for my system.

As shown in Fig. 2.4(b), the estimates of  $T_{\text{eff}}$  are higher than room temperature  $T_0$  and increase linearly with  $c$  at least for  $c < 7.5 \times 10^9$  cells/mL. In this regime ( $c < 7.5 \times 10^9$  cells/mL), the bacterial suspensions can be considered dilute and homogenous with particle-bacteria interactions being binary to leading order. Additionally, in the absence of collective behavior, fluctuations in bacterial concentration scale as  $\sqrt{c}$ . These features imply that the effective diffusivity  $D_{\text{eff}}$  has a linear dependence on  $c$ , consistent with my measurements (see Appendix A.2.4 for figure and more details). Therefore, the extended Stokes-Einstein relationship suggests effective temperature also scales linearly with concentration, as shown in Fig. 2.4(b).

At the highest concentration ( $c = 7.5 \times 10^9$  cells/mL), the slope in the  $T_{\text{eff}}$  versus  $c$  curve decreases. This decreasing slope may be understood using a momentum flux argument for purely steric interactions that include the bacteria and particle size. In the over-damped systems, as in my bacteria suspensions, the momentum flux to the particle due to bacteria-particle interactions results in excess kinetic energy, which is eventually dissipated away viscously. At low concentrations, the flux (and therefore the active temperature) is proportional to  $c$ . If interactions are not purely binary, as at high concentrations, the bacteria size as well as particle size may limit the number of bacteria interacting with the particle at any given time and  $T_{\text{eff}}$  may saturate due to finite size effects.

Finally, I investigate the role of particle diameter in the suspension effective temperature. Figure 2.4(c) shows the values of  $T_{\text{eff}}$  estimated from an extended Stokes-Einstein relation as a function of  $d$  for different values of  $c$ . Surprisingly, I find that  $T_{\text{eff}}$  increases with particle size  $d$ , a behavior different from thermally equilibrated systems where temperature does not depend on the probe size. I note that for the largest particle diameter,  $d = 39 \mu\text{m}$ , estimated  $T_{\text{eff}}$  values are approximately 100 times greater than room temperature  $T_0 = 295 \text{ K}$ , consistent with previous reports [25].

The dependence of  $T_{\text{eff}}$  on particle size  $d$  (Fig. 2.5(a)) may be understood through the previously

introduced extended Stokes-Einstein relation,  $T_{\text{eff}} = D_{\text{eff}} f_0 / k_B = T_0 + (3\pi\mu D_A / k_B) d$ , where  $T_0 = (3\pi\mu D_0 / k_B) d$ . If  $D_A$  were independent of  $d$ , then  $T_{\text{eff}}$  would be linear in  $d$ . However, a linear fit does not adequately capture the trend over the full range of particle diameters. This is a consequence of the particle size dependent  $D_{\text{eff}}$  shown in Fig. 2.3(b) and hints at a particle-size dependent active diffusivity  $D_A$ . This variation of  $T_{\text{eff}}$  with  $d$  highlights the interplay between particle size and the properties of the self-propelling particles (*E. coli*) as well as challenges in gauging activity using passive particles.

### 2.3.4 Active Diffusivity of Passive Particles in Bacterial Suspensions

To explore the aforementioned dependence of  $D_A$  on particle size, I plot  $D_A = D_{\text{eff}} - D_0$  with  $d$ . Here,  $D_0$  is the particle thermal diffusivity (in the absence of bacteria<sup>1</sup>) and is obtained from the Stokes-Einstein relation  $D_0 = \frac{k_B T_0}{3\pi\mu d}$ . Indeed, as shown in Fig. 2.5(a),  $D_A$  exhibits a non-monotonic dependence on  $d$  for all  $c$ .

To understand the observed dependence of the active diffusivity on the particle size, I consider the relevant time scales in my particle/bacteria suspensions, namely: (i) the time for the particle to thermally diffuse a distance  $L$  equal to the total bacterial length  $L^2/D_0$ , (ii) the time for a bacterium to swim at a speed  $U$  for a distance  $L$  given by  $L/U$ , and (iii) the mean run time which is the inverse of the tumbling frequency  $\omega_T^{-1}$ . Dimensionless analysis then suggests there are two independent time parameters: (i) the ratio of the first two above, which is the Péclet number,  $\text{Pe} \equiv UL/D_0$ , and (ii)  $\tau^* = U/\omega_T L$ , which is the ratio of the run length  $U/\omega_T$  to the bacterial length.

It is these two parameters,  $\text{Pe}$  and  $\tau^*$ , that govern the particle dynamics in my experiments. When the Péclet number is much less than one, then the thermal particle diffusion dominates and transport by the bacteria is ineffective. When the Péclet number is much larger than one, then thermal diffusion is negligible and the transport is due to the convection from bacteria. The swimming

---

<sup>1</sup>For a suspension of passive particles of volume fraction  $\phi$ , the Einstein viscosity [46] is  $\mu = \mu_0(1 + 5\phi/2)$ , where  $\mu_0$  is the viscosity of the suspending medium. In the absence of collective motion, the maximum change in the viscosity due to bacteria (since they are force free and exert no drag on the fluid) in my bacterial suspensions (with volume fractions of  $\phi = 1\%$ ) is thus 2.5%. Therefore,  $\mu$  and  $D_0$  is not expected to change significantly with the bacterial concentrations used here. This is consistent with the observation that the effective temperature estimates from both an extended Stokes-Einstein relation and particle speed distribution (Fig. 4b) agree.

speed  $U$ , tumble frequencies  $\omega_T^{-1}$ , and combined length of the cell body and flagellar bundle  $L$  are estimated from prior experiments [16,47] with *E. coli* as approximately  $10 \mu\text{m/s}$ ,  $1 \text{ s}^{-1}$ , and  $L \approx 7.6 \mu\text{m}$ , respectively. Thus, in my experiments, the Péclet number varies from approximately 130 to 8600, via the particle bare diffusivity  $D_0$  (through the particle diameter). I note that one stain of bacteria is used – thus, the run length and bacteria size do not change in my experiments, and consequently,  $\tau^* \approx 1.8$  is a constant.

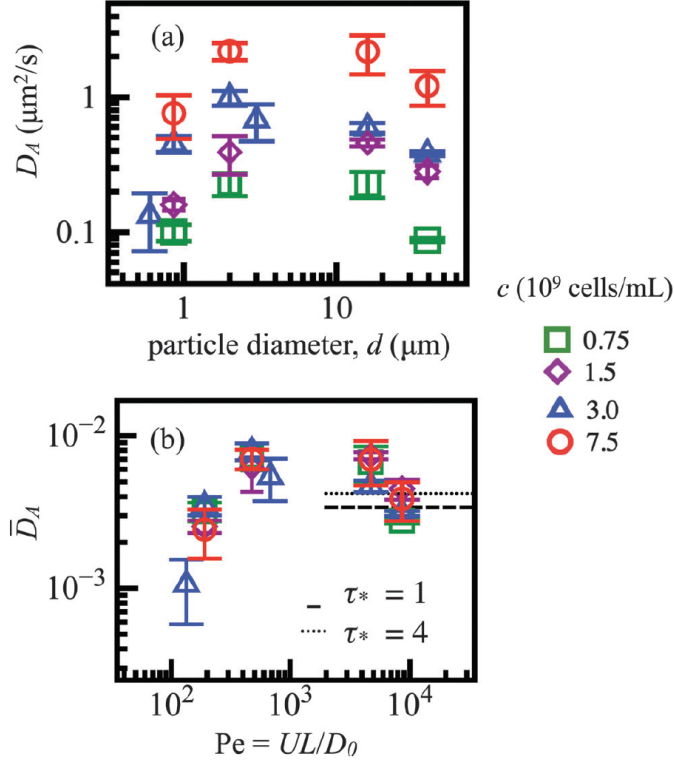


Figure 2.5: (a) Active diffusivities  $D_A = D_{\text{eff}} - D_0$  are non-monotonic with particle size for varying concentrations of bacteria. (b) Scaled hydrodynamic diffusivity  $\bar{D}_A = D_A/cUL^4$  collapses with Péclet number  $\text{Pe} = UL/D_0$ . The maximum  $\bar{D}_A$  occurs at  $\text{Pe}_A$  between 450 and 4500. For  $100 < \text{Pe} < \text{Pe}_A$ ,  $\bar{D}_A$  scales as  $\text{Pe}^\alpha$ , where  $\alpha \approx 2$ .

In order to gain insight into the non-trivial dependence of  $D_A$  on  $d$ , I scale out the concentration dependence by introducing the dimensionless active diffusivity  $\bar{D}_A = D_A/cUL^4$  and plot it against the Péclet number,  $\text{Pe}$ . Figure 2.5(b) shows that all the active diffusion  $D_A$  versus  $d$  data shown in Figure 2.5(a) collapses into a single master curve, thereby indicating that  $\bar{D}_A$  is independent of  $c$ , at least for dilute suspensions investigated here.

I find that for  $Pe \lesssim 10^3$ , the values of  $\overline{D}_A$  initially increases with increasing  $Pe$  (or particle size) and follows a scaling  $\overline{D}_A \sim Pe^2$ . The observed increase of  $\overline{D}_A$  with  $Pe$  may be due to the decreasing particle Brownian motion, which allows the particle's motion to be correlated with the bacterial velocity disturbances for longer times.

In the limit of  $Pe \rightarrow \infty$ , the particle's Brownian motion vanishes and the particle displacements are dominated by the convective transport via bacteria-particle interactions. Thus  $\overline{D}_A$  is expected to be independent of  $Pe$  and depend only on the parameter  $\tau^*$ , defined here as the ratio of the run length  $U/\omega_T$  to the bacterial length  $L$ . My experimentally measured  $\overline{D}_A$ , which correspond to  $\tau^* \approx 1.8$ , exhibit a slight decline with  $Pe$  at high  $Pe$  and have magnitudes that agree well with recent theoretical predictions [7] (dashed lines in Fig. 2.5(b)) for very large Péclet at  $\tau^* = 1$  and  $\tau^* = 4$ . An increase in the run time (or  $\tau^*$ ) would increase the asymptotic value of the scaled active diffusivity  $\overline{D}_A$  (see Appendix A.4).

An important feature of the data shown in Fig. 2.5(b) is the peak in  $\overline{D}_A$  at  $Pe_A \approx 10^3$ . The appearance of the peak in  $\overline{D}_A$  in my data may be due to the weak but non-zero effects of Brownian motion, which allows particles to sample the bacterial velocity field in such a way that the mean square particle displacements and correlation times are higher compared to both the very high  $Pe$  (negligible Brownian motion) as well as the very low  $Pe$  (Brownian dominated) [7]. This feature (i.e. peak in  $\overline{D}_A$ ) is surprising because it suggests an optimum particle size for maximum particle diffusivity that is coupled to the activity of the bacteria. The existence of such a peak has been predicted in a recent theory/simulation investigation [7], and my data agrees at least qualitatively with such predictions. I note that the predicted peak in  $\overline{D}_A$  happens at a  $Pe \approx O(10)$ , which is smaller than my experimental values of ( $Pe \approx 10^3$ ). One reason why may be due to variations in bacterial concentration within the film, especially near the film's surfaces where bacteria may cluster.

## 2.4 Maximum Particle Effective Diffusivity $D_{\text{eff}}$

My data (Fig. 2.5(b)) shows that the dimensionless active diffusion  $\overline{D}_A$  collapses unto a universal curve with a peak in  $Pe$  for all bacterial concentrations. The data also shows that, with the exception of the lowest bacterial concentration  $c$ , the particle effective diffusivity  $D_{\text{eff}}$  exhibits a peak in  $d$ , which

varies with  $c$  (Fig. 2.3(a)). For instance, for  $c = 1.5 \times 10^9$  cells/mL, the peak is at approximately  $2 \mu\text{m}$ , while for larger concentrations ( $c = 7.5 \times 10^9$  cells/mL), the peak (as obtained by fitting the data to a continuous function) shifts to higher values of  $d$ . This suggests that one can select the particle size which diffuses the most by tuning the bacteria concentration.

In what follows (see also Appendix A.5, I provide a prediction, based on my experimentally-measured universal curve of  $\overline{D}_A$  with  $\text{Pe}$  (Fig. 2.5(b)) for the existence as well as the location of the peak of  $D_{\text{eff}}$  in  $d$ . As noted before, the particle effective diffusivity  $D_{\text{eff}}$  can be described as the linear sum of the particle thermal diffusivity  $D_0$ , which is independent of  $c$  and decreases with  $d$ , and the active diffusivity  $D_A$ , which is linear in  $c$  and non-monotonic in  $d$ , through the particle-size dependent  $\overline{D}_A$ . Therefore, I can recast the effective diffusivity as

$$D_{\text{eff}} = D_0 + (cL^3) (UL) \overline{D}_A. \quad (2.3)$$

The criterion for the existence of a maximum  $D_{\text{eff}}$  is obtained by taking the derivative of eqn (2.3) with respect to the Péclet number and setting the derivative to zero. In order to estimate  $\overline{D}_A$  (and its slope), I fit the data in Fig. 2.5(b) near the peak in the range  $200 < \text{Pe} < 4000$  with a second order polynomial equation. I find that a peak exists in  $D_{\text{eff}}$  if

$$cL^3 \gtrsim 0.4. \quad (2.4)$$

For the bacterial length used here  $L = 7.6 \mu\text{m}$ , this yields  $c \approx 0.9 \times 10^9$  cells/mL, which is in quantitative agreement with the concentration range ( $0.75 \times 10^9$  cells/mL  $< c < 1.5 \times 10^9$  cells/mL) in which the peak in  $D_{\text{eff}}$  emerges in my data (Fig. 2.3(a)). As described in Appendix A.5, I find that the location of the  $D_{\text{eff}}$  peak in  $d$  here defined as  $d_{\text{eff}}^{\text{max}}$  is given by

$$d_{\text{eff}}^{\text{max}} \approx d_A \left[ 1 - \left( \frac{1}{5cL^3 - 2} \right) \right] \quad (2.5)$$

where  $d_A$  corresponds to the Péclet number  $\text{Pe}_A \approx 1000$  at which  $\overline{D}_A$  is maximum. For the *E. coli* used here,  $d_A = kT\text{Pe}_A/3\pi\mu UL \approx 6 \mu\text{m}$ . Note that  $d_{\text{eff}}^{\text{max}}$  is always less than or equal to  $d_A$  and increases with  $c$ , consistent with my experimental observations (Fig. 2.3(a)). In general the criterion, eqn (2.4), and  $d_{\text{eff}}^{\text{max}}$ , eqn (2.5), will depend on  $\tau^*$ . For suspensions of bacteria, the universal curve of  $\overline{D}_A$  informs when and where a peak in the particle diffusivity occurs.



## 2.5 Summary and Conclusions

In summary, I find that the effective particle diffusivity  $D_{\text{eff}}$  and temperature  $T_{\text{eff}}$  in suspensions of *E. coli* show strong deviations from classical Brownian motion in the way they depend on particle size  $d$ . For example, Fig. 2.3(a) shows that  $D_{\text{eff}}$  depends non-monotonically in  $d$  and includes a regime in which larger particles can diffuse faster than smaller particles. The existence as well as the position of a  $D_{\text{eff}}$  peak in  $d$  can be tuned by varying the bacterial concentration  $c$ . I also find that the cross-over time  $\tau$  increases with particle size and scales as approximately  $d^n$ , where  $1/2 \lesssim n \lesssim 1$ , as shown in Fig. 2.3(b).

Measures of  $T_{\text{eff}}$  obtained from either an extended Stokes-Einstein relation or particle speed distributions seem to agree quite well (Fig. 2.4(b)). This is surprising since this kind of agreement is only expected for systems at equilibrium. The good agreement between the measurements suggests that  $T_{\text{eff}}$  may be a useful signature of bacterial activity. However, unlike thermally equilibrated systems,  $T_{\text{eff}}$  varies with size  $d$  (Fig. 2.4(c)). This non-trivial dependence of both  $D_{\text{eff}}$  and  $T_{\text{eff}}$  on particle size  $d$  implies that these common gauges of activity are not universal measures. Nevertheless, my data suggest that one can define optimal colloidal probes of activity for suspensions of bacteria, which correspond to  $\text{Pe} = UL/D_0 \approx 10^3$ . At these Pe values,  $\bar{D}_A$  is maximized, which provides ample dynamical range (magnitude of the signal). Also at these Pe values, the cross-over time  $\tau$  is still relatively small, which allows for adequate temporal resolution. Both of these features are important in using passive particles to characterize a spatially and temporally varying level of activity in materials.

My anomalous particle-size dependent results in active fluids has important implications for particle sorting in microfluidic devices, drug delivery to combat microbial infections, resuspension of impurities and the carbon cycle in geophysical settings populated by microorganisms. A natural next step would be to study the role of external fields such as gravity or shear in influencing particle transport in these active environments.

# Bibliography

- [1] Pruppacher HR, Klett JD. 1978. **Microphysics of Clouds and Precipitation.** *Reidel, Dordrecht.*
- [2] Perry SF, Burggren WW. 2007. **Why respiratory biology? The meaning and significance of respiration and its integrative study.** *Integr. Comp. Biol.* 47:506-509.
- [3] Górak A, Sorensen E. 2014. *Distillation: Fundamentals and Principles.* *Academic Press.*
- [4] Einstein A, 1905. **The theory of the brownian movement.** *Ann. Physik* 17:549.
- [5] Ojha RP, Lemieux PA, Dixon PK, Liu AJ, Durian DJ. 2004. **Statistical mechanics of a gas-fluidized particle** *Nature* 427:521-523.
- [6] Cipelletti L, Ramos L. 2005. **Slow dynamics in glassy soft matter.** *J. Phys.: Condens. Matter* 17:R253-R285.
- [7] Sokolov A, Aranson IS. 2009. **Reduction of Viscosity in Suspension of Swimming Bacteria.** *Physical Review Letters* 103:148101.
- [8] Zhang HP, Be'er A, Florin EL, Swinney HL. 2010. **Collective motion and density fluctuations in bacterial colonies.** *Proceedings of the National Academy of Sciences* 107:13626.
- [9] Takagi D, Braunschweig AB, Zhang J, Shelley MJ. 2013. **Dispersion of Self-Propelled Rods Undergoing Fluctuation-Driven Flips.** *Physical Review Letters* 110:038301.
- [10] Palacci J, Sacanna S, Steinberg AP, Pine DJ, Chaikin PM, 2013. **Living crystals of light-activated colloidal surfers.** *Science* 339:936.
- [11] Ndec FJ, Surrey T, Maggs AC, Leibler S. 1997. **Self-organization of microtubules and motors.** *Nature* 389:6648.

- [12] Marchetti MC, Joanny JF, Ramaswamy S, Liverpool TB, Prost J, Rao M, Aditi Simha R. 2013. *Rev. Mod. Phys.* 85:1143.
- [13] S. Ramaswamy. 2010. **Hydrodynamics of soft active matter.** *Annu. Rev. Condens. Matter Phys.* 1:323-45.
- [14] Mussler M, Rafai S, P. Peyla, Wagner C. 2013. **Effective viscosity of non-gravitactic *Chlamydomonas Reinhardtii* microswimmer suspensions.** *EPL* 101:54004.
- [15] Kaiser A, Lowen H. 2014. **Unusual swelling of a polymer in a bacterial bath.** *J. Chem Phys.* 141:044903.
- [16] Patteson AE, Gopinath A, Goulian M, Arratia PE. 2015. **Running and tumbling with *E. coli* in polymeric solutions.** *Scientific Reports* 5:15761.
- [17] Leptos KC, Guasto JS, Gollub JP, Pesci AI, Goldstein RE. 2009. *Physical Review Letters* 103:198103.
- [18] Kurtuldu H, Guasto JS, Johnson KA, Gollub JP. 2011. **Dynamics of Enhanced Tracer Diffusion in Suspensions of Swimming Eukaryotic Microorganisms.** *Proceedings of the National Academy of Sciences* 108:10391.
- [19] Thiffeault JL, Childress S. 2010. **Stirring by swimming bodies.** *Phys. Lett. A*, 374:3487-3490.
- [20] Kim MJ, Breuer KS. 2004. **Enhanced diffusion due to motile bacteria.** *Physics of Fluids* 16:L78.
- [21] Josenhans C, Suerbaum S. 2002. **The role of motility as a virulence factor in bacteria..** *Int. J. Med. Microbiol.* 291:605-614.
- [22] Costerton JW, Stewart PS, Greenberg EP. 1999. **Bacterial biofilms: a common cause of persistent infections.** *Science* 284:1318-1322.
- [23] Bixler GD, Bhushan B. 2012. **Biofouling: lessons from nature.** *Phil. Trans. R. Soc. A* 370:2381-2417.
- [24] Valentine DL, Kessler JD, Redmond MC, Mendes SD, Heintz MB, Farwell C, Hu L, Kinnaman FS, Yvon-Lewis S, Du M, Chan EW, Tigreros FG, Villanueva CJ. 2010. **Propane respiration jump-starts microbial response to a deep oil spill.** *Science* 330:208.

- [25] Wu XL, Libchaber A. 2000. **Particle Diffusion in a Quasi-Two-Dimensional Bacterial Bath.** *Physical Review Letters* 84:3017.
- [26] Jepson A, Martinez VA, Schwarz-Linek J, Morozov A, Poon WCK. 2013. **Enhanced diffusion of nonswimmers in a three-dimensional bath of motile bacteria.** *Phys. Rev. E* 88:041002.
- [27] Miño G, Mallouk TE, Darnige T, Hoyos M, Dauchet J, Dunstan J, Soto R, Wang Y, Rousselet A, Clément E. 2011. **Enhanced Diffusion due to Active Swimmers at a Solid Surface.** *Physical Review Letters* 106, 048102.
- [28] Chen DTN, Lau AWC, Hough LA, Islam MF, Goulian M, Lubensky TC, Yodh AG. 2007. **Fluctuations and Rheology in Active Bacterial Suspensions.** *Physical Review Letters* 99:148302 (2007).
- [29] Pushkin DO, Yeomans JM. 2013. **Fluid Mixing by Curved Trajectories of Microswimmers.** *Physical Review Letters* 111:188101.
- [30] Underhill PT, Hernandez-Ortiz JP, Graham MD. 2008. **Diffusion and Spatial Correlations in Suspensions of Swimming Particles.** *Physical Review Letters* 100:248101 (2008).
- [31] Hernandez-Ortiz JP, Underhill PT, Graham MD. 2009. **Dynamics of confined suspensions of swimming particles.** *J. Phys.: Condens. Matter* **21**:204107.
- [32] Kasyap TV, Koch DL, Wu M. 2014. **Hydrodynamic tracer diffusion in suspensions of swimming bacteria.** *Physics of Fluids* 26:081901.
- [33] Loi D, Mossa S, Cugliandolo LF. 2008. **Effective temperature of active matter.** *Phys. Rev. E* 77:051111.
- [34] Rogers SS, van der Walle C, Waigh TA. 2008. **Microrheology of bacterial biofilms in vitro: Staphylococcus aureus and Pseudomonas aeruginosa.** *Langmuir* 24:13549-13555.
- [35] Vaccari L, Allan DB, Sharifi-Mood N, Singh AR, Leheny RL, Stebe KJ. 2015. **Films of bacteria at interfaces: three stages of behaviour.** *Soft Matter* 11:6062-6074.
- [36] Fodor É, Guo M, Gov NS, Visco P, Weitz DA, van Wijland F. 2015. **Activity-driven fluctuations in living cells.** *Euro Phys Lett.* 110:48005.

- [37] Berg HC. 2008. **E. coli in Motion.** *Springer Science & Business Media.*
- [38] Qin B, Gopinath A, Yang J, Gollub JP, Arratia PE. 2015. **Flagellar Kinematics and Swimming of Algal Cells in Viscoelastic Fluids.** *Scientific Reports* 5:9190.
- [39] Crocker J, Grier D. 1996. **Methods of Digital Video Microscopy for Colloidal Studies.** *J. Colloid. Interf. Sci* 179:298.
- [40] Huang R, Chavez I, Taute KM, Lukić B, Jeney S, Raizen MG, Florin, E. 2011. **Direct observation of the full transition from ballistic to diffusive Brownian motion in a liquid.** *Nature Physics* 7:576-580.
- [41] Pathria PK. 1996. **Statistical Mechanics.** *Butterworth, Oxford.*
- [42] Sokolov A, Apodaca MM, Grzybowski BA, Aranson IS, 2010. **Swimming bacteria power microscopic gears.** *Proceedings of the National Academy of Sciences* 107:969-974.
- [43] Ben-Isaac E., Park Y, Popescu G, Brown FL, Gov NS, Shokef Y. 2011. **Effective Temperature of Red-Blood-Cell Membrane Fluctuations.** *Physical Review Letters* 106:238103.
- [44] Ben-Isaac E, Fodor É, Visco P, van Wigland F, Gov NS. 2015. **Modeling the dynamics of a tracer particle in an elastic active gel.** *Phys. Rev. E* 92:012716.
- [45] López HM, Gachelin J, Douarche C, Auradou H, Clément E. 2010. **Enhanced Diffusion due to Active Swimmers at a Solid Surface.** *Physical Review Letters* 107:969-974.
- [46] Einstein A. 1906. the theory of Brownian movement. *Ann. der Physik* 19:289-306.
- [47] Min TL, Mears PJ, Chubiz LM, Rao CV, Golding I, Chemla YR. 2009. **High-resolution, long-term characterization of bacterial motility using optical tweezers.** *Nature Methods* 6:831-835.

# Chapter 3

## Polymer dynamics in active fluids: how swimming *E. coli* and polymer molecules interact.

### 3.1 Introduction

Flagellar propulsion of microorganisms is perhaps one of the earliest forms of motility [1, 2]. This flagellar propulsion plays an important role in various biological and ecological settings, such as the spread and control of diseases [3-6], transport in lakes and oceans [7] and the biodegradation of environmental pollutants [8]. Therefore, it is essential to understand the role of the ambient environment in mediating and influencing the motility of microorganisms. Many of these environments are liquid-like and contain particles, polymers or other macromolecules, which introduce non-Newtonian features to the fluid such as shear-thinning viscosity and elasticity. These so-called complex fluids can strongly affect the motility of microorganisms [9-12]. For instance, glycoproteins in the stomach mucus form a viscoelastic gel that offer an effective barrier against most parasitic microorganisms. Yet, the bacterium *H. pylori* excretes enzymes that transform the impenetrable gel into a viscous

polymer solution, which enables swimming and ultimately leads to persistent infections [13]. In this case, the subtle interplay of cell activity and complex material properties has significant impact: *H. pylori* alone infects 50% of the world’s population [5], and more generally, bacteria comprise 65% of human microbial infections [14].

Many additional biological functions rely on the motion of living particles in complex fluids, including fertilization through sperm cells swimming within cervical mucus [15] and the transport of mucus in the human lungs by rhythmically beating cilia [16]. An emerging number of investigations reveal intricate (and sometimes contradictory) ways in which the fluid material properties affect the motility of microorganisms. For example, fluid elasticity has been found to either enhance [17-21] or hinder [10, 22, 23] microorganism’s swimming speed depending on the details of the swimming kinematics and the generated flow fields. Recently, the effects of shear-thinning viscosity, a common attribute of many polymeric fluids, have been found to have little to no effect on swimming speed in experiments [24, 25] and theoretical studies [26]. In contrast, experiments with the bacterium *E. coli* indicate that the shear-thinning viscosity of semi-dilute polymer solutions can lead to an enhancement in swimming speed [25]. Together, these works highlight the subtle interplay between fluid material properties and swimming kinematics, which results in a striking and often unanticipated variety of outcomes.

In this chapter, I focus on run-and-tumble motility, a general mechanism employed by many prokaryotic flagellated bacteria (e.g. *E. coli*, *S. marcescens*, and *V. alginolyticus*) and even some eukaryotic organisms such as the green algae *C. reinhardtii* [27]. This mechanism can be described as a repeating sequence of two actions: (i) a period of nearly constant-velocity straight-line translation (run) followed by (ii) a seemingly erratic rotation (tumble). This run and tumble series – a hallmark of many swimming bacteria ultimately dictates their spread and transport. Here, the transport is effectively described by a persistent random walk with an active effective diffusion coefficient. While the run and tumble mechanism has been widely studied in simple, water-like (i.e. Newtonian) fluids [28-31], many bacteria that employ this mechanism live in biological fluids that contain macromolecules and are not Newtonian. Since motility is directly linked to virulence [3, 6], understanding the role of fluid rheology on run-and-tumble dynamics and the overall spread of bacteria is therefore of much practical interest.

## 3.2 Methods

Here, the run-and-tumble motility of the bacterium *E. coli* is experimentally investigated in polymeric solutions using cell tracking methods and single molecule experiments. The bacterium *E. coli* is an archetypical model for studies of run-and-tumble dynamics [28, 31]. *E. coli* is known to thrive in the human digestive tract (a viscoelastic medium) and is a common agent for food poisoning [32]. I find that the presence of even small amounts of polymers in solution dramatically alters the cell motility: tumbling is suppressed and cells swim faster. By varying (i) the type of polymer, (ii) polymer molecular weight (MW) and (iii) polymer concentration, I show that fluid viscosity suppresses tumbles while fluid elasticity enhances swimming speed. I also show in single molecule experiments using fluorescently labeled DNA polymers that the flow field generated by *E. coli* is able to stretch initially coiled polymer molecules, and thus induce elastic stresses in the fluid. These changes in motility behavior, driven by the material properties of the ambient fluid, can have profound influences on transport and foraging of nutrients. My results also suggest that tuning the material properties of the fluidic environment can control the spreading of bacteria.

I experiment with different types of polymeric fluids and a water-like buffer solution. Three main types of polymer molecules are used: poly-ethylene glycol (PEG, Sigma-Aldrich,  $MW = 8.0 \times 10^4$ ,  $R_g = 6$  nm), carboxy-methyl cellulose (CMC - a linear, flexible polymer, Sigma-Aldrich,  $MW = 7.0 \times 10^5$ ,  $R_g = 28$  nm) and xanthan gum (XG, Sigma Aldrich,  $MW = 2.0 \times 10^6$ ,  $R_g = 600$  nm), where  $R_g$  is the polymer radius of gyration. I note that radius of gyration of the polymer molecules range from 6 nm to 600 nm. This range is comparable to the width of a single *E. coli* flagellum (approximately 20 nm) but smaller than total effective length of the bacterium (body plus flagellar bundle) of approximately  $7 \mu\text{m}$  [28]. I varied CMC concentrations from 10 to 500 ppm, significantly below the overlap concentration of  $10^4$  ppm, to diminish the role of polymer-polymer interactions and avoid the presence of polymer networks. To discriminate between the roles of elasticity and shear-thinning fluid properties, I also use CMC of different molecular weights ( $9.0 \times 10^4$ ,  $2.5 \times 10^5$ , and  $7.0 \times 10^5$ ) as well as solutions of xanthan gum, a semi-rigid polymer. Xanthan gum solutions exhibit shear-thinning viscosity and elasticity. By adjusting the polymer concentration and MW, I make fluids of desirable viscosity ( $1.0 < 20$  mPa s) and elasticity (fluid relaxation time  $\lambda$  up to 50 ms [33]). Finally, Newtonian fluids are prepared using (i) a water-like buffer solution of 67 mM NaCl in water and (ii) PEG aqueous solutions. The concentration of PEG in solution varies from 1.3 to 3.5%



by weight. All PEG solutions display Newtonian viscosity. See Appendix B.1 for rheology details.

My experimental protocol consists of directly observing *E. coli* cells suspended in thin fluid films (Appendix B.2). I track the orientation of representative cell bodies via the angle  $\phi$ , defined as the angle made by the unit vector aligned with the major axis of the elliptical cell body  $p$  and the x-axis,  $\cos \phi = p \cdot e_x$ . The orientation of the trajectory is tracked using the angle  $\theta$  defined by  $\cos \theta = (r \cdot e_x)/|r|$ , where  $e_x$  is the unit vector aligned with the x-axis.

## 3.3 Results & Discussion

### 3.3.1 *E. coli* trajectories

Representative *E. coli* trajectories in buffer (Newtonian) and carboxy-methyl cellulose (CMC, MW =  $7.0 \times 10^5$ , c = 500 ppm) solutions are shown in Fig. 3.1(a) and 3.1(b), respectively. In buffer solution, cells swim in various directions, executing a random walk and frequently change direction, typical of the run-and-tumble mechanism [28]. Figure 3.1(b) reveals a very different behavior. If I replace the Newtonian fluid by the CMC solution, the cell paths are smoother and straighter, exhibiting changes in direction less frequently. I further illustrate these changes in swimming behavior by examining sample trajectories (time interval of 2 seconds) in buffer (Fig. 3.1c) and CMC (Fig. 3.1d) solutions. I identify tumbles (arrows in Fig. 3.1c and d) in the sample trajectories by tracking sudden changes in direction and simultaneous drops in speed. Surprisingly, I find that cell trajectories in the CMC solutions are nearly devoid of tumbles compared to the buffer case. Figure 3.1(e,f) shows the instantaneous cell body orientation  $\phi$  during sample trajectories for a fixed distance ( $\sim 10 \mu\text{m}$ ). The data shows that  $\phi$  is also strikingly different for cells swimming in polymeric solutions. Figure 3.1(e) shows that, in buffer solution, the orientation of the cell body oscillates significantly along its path. These two-dimensional lateral oscillations of the cell body, known as wobbling, are projections of the cell's three-dimensional helical trajectory [34, 35]. In the CMC solution, however, this oscillation (wobbling) significantly diminishes, and  $\phi$  remains relatively constant (Fig. 3.1f). This hints to a change in the *E. coli* swimming kinematics such as the pitch or angle of the cell helical path. Overall, the results shown in Fig. 3.1 indicate that the presence of even small amounts of polymer in liquids can significantly affect the motility of microorganisms and, in the case of *E. coli*, suppresses tumbles and body oscillations.

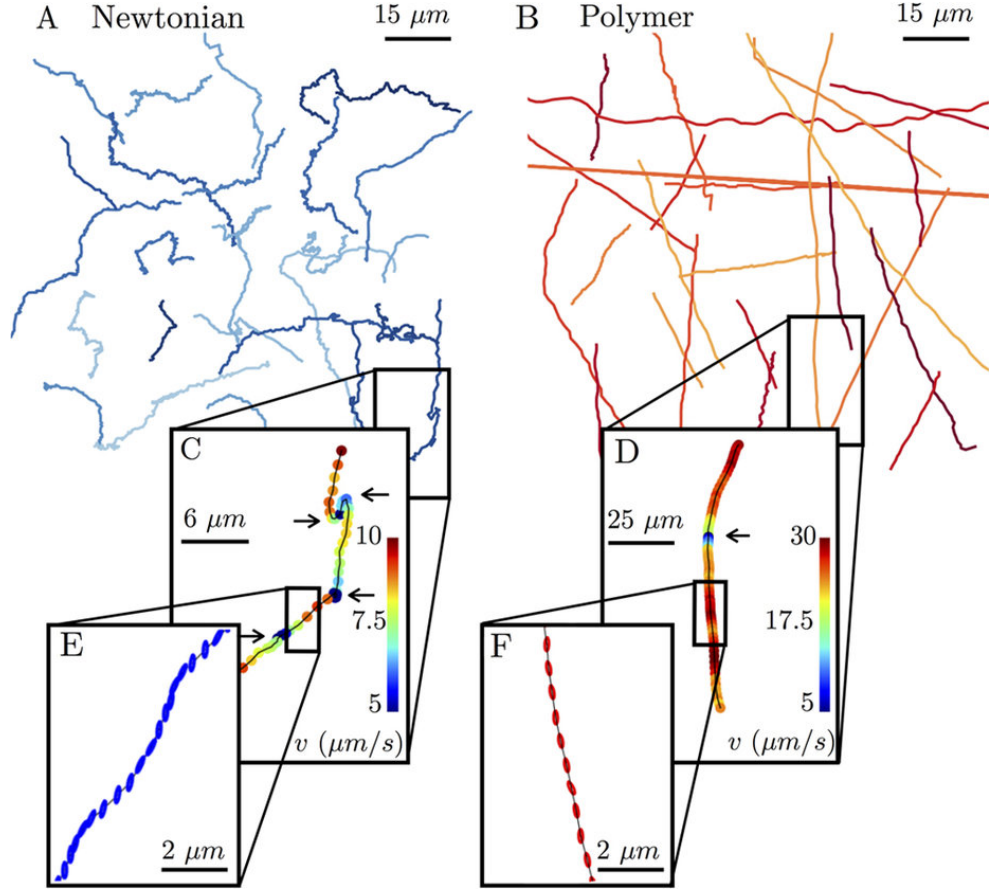


Figure 3.1: Kinematics of swimming *E. coli* cells in both Newtonian and viscoelastic fluids. (A) Trajectories of *E. coli* cells in buffer ( $1.0 \text{ mPa}\cdot\text{s}$ ) and (B) in polymeric solution (CMC  $\text{MW} = 7.0 \times 10^5$ ,  $c = 500 \text{ ppm}$ ,  $c^* = 10^4$ ,  $\mu = 19 \text{ mPa}\cdot\text{s}$ ). Cells in polymer solution move remarkably straighter compared to cells in buffer. Sample cell trajectories in (C) buffer and (D) polymeric solutions exhibit run-and-tumble i. e. nearly straight lines connected at random angles (tumbles denoted by arrows). (E) The cell body orientation oscillates or ‘wobbles’ in the buffer solution. (F) Wobbles diminish in the polymer solution.

To quantify the above observations, I calculate the *E. coli* instantaneous velocity  $v$  and its magnitude  $|v|$  as a function of time from the tracking data. The velocity vector is defined over a time interval of  $t = 1/15$  s, which is large enough to average over  $\phi$  yet small enough to define an average swimming orientation  $\theta$  between tumbles (Fig. 3.2a). Figure 3.2b shows examples of velocity magnitudes  $|v|$  as a function of time for buffer and CMC solutions ( $c = 500$  ppm). The data shows that cells swimming in CMC solutions execute tumbles (denoted by arrows) less frequently than in buffer (Newtonian) solutions. Here, the cell in buffer tumbles 5 times in the span of 6 seconds. In contrast, the cell in polymeric solution (CMC) tumbles only twice in the same time span.

The sample velocity records in Fig. 3.2(b) show that an individual *E. coli* swims faster in CMC solution ( $25 \mu\text{m/s}$ ) than in the buffer ( $10 \mu\text{m/s}$ ) even though the CMC solution has a viscosity that is over an order of magnitude ( $\mu \approx 20 \text{ mPa s}$ ) larger than that of the buffer ( $\mu = 1 \text{ mPa s}$ ). Figure 3.2(c) shows that the mean instantaneous cell velocity  $\langle v \rangle$  (averaged over hundreds of individual cells) increases with polymer concentration from about  $8.3 \mu\text{m/s}$  in buffer solution to  $12.4 \mu\text{m/s}$  in CMC solutions ( $c = 500$  ppm); the speed in buffer is consistent with previous measurements [36]. This enhancement in  $\langle v \rangle$  with polymer concentration is somewhat counterintuitive, since the viscosity increases as polymer is added to the fluid (Appendix B.1). I note that in a Newtonian fluid the viscous torque on the cell flagella bundle  $\tau_b$  is proportional to  $\mu\omega$ , where  $\omega$  is the bundle rotation rate. For *E. coli* swimming at constant motor torque  $\tau_m$  [31], the torque balance yields  $\tau_m \sim \tau_b$ , and thus  $\tau_m$  is also proportional to  $\mu\omega$ . In highly viscous environments corresponding to swimming at low Reynolds number, Stokes equations hold and thus the speed varies with the frequency  $v \propto \omega$  [11, 34, 37, 38]. Therefore, as viscosity increases, the bundle rotation rate  $\omega$  and correspondingly the forward velocity should decrease as  $\mu^{-1}$ . The increase in average velocity  $\langle v \rangle$  with polymer concentration is thus unexpected.

Similar increases in cell velocity with polymer concentration have been previously reported [37, 39]. It has been argued that cell velocity is augmented by the presence of a gel-like network which exerts an anisotropic viscous drag on the cell [40]. In the experiments, however, the CMC (polymeric) solutions are considered dilute ( $c = 5\%$  of the overlap concentration) in the sense that polymer networks are not present. Thus the anisotropic viscosity argument given by [40] does not explain my results. More recently, Martinez *et al.* [25] argued that shear-thinning viscosity of semi-dilute polymeric solutions was responsible for enhancing the *E. coli* swimming velocity. Here, I will

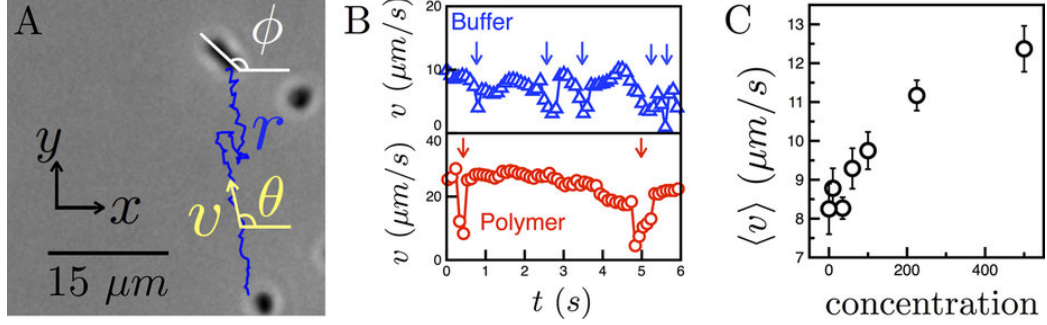


Figure 3.2: Swimming speeds of *E. coli* in buffer and polymeric solutions. (A) Velocity  $v$ , average cell orientation  $\theta$ , and instantaneous cell body orientation  $\phi$  are defined as shown. (B) Temporal variations in the cell body speeds in buffer and polymeric solutions ( $c = 500$  ppm) reveal tumbles (arrows) via sudden drops in  $v$ . The cell in buffer swims at a lower velocity and tumbles more frequently compared to the cell in the polymer solution. (C) The mean cell velocity increases from 8.3 to 12.4  $\mu\text{m/s}$  with increasing polymer concentration.

show an alternative explanation. Namely, the increase in swimming speed can also be due to extra elastic stresses.

### 3.3.2 Statistical measures of cell motility

Next, I quantify the effective translational ( $D_T$ ) and rotational ( $D_R$ ) diffusivity of swimming *E. coli* by computing the mean-squared displacement (MSD) and the mean-squared angular displacement (MSAD) from tracking data, as shown in Fig. 3.3(a) and 3.3(b). The mean-squared displacement is defined as  $\text{MSD}(\Delta t) = |r(t_0 + \Delta t) - r(t_0)|^2$ . For a random walk, the MSD is  $4D_T\Delta t$  in two dimensions, where  $D_T$  is the effective translational diffusion coefficient. For a swimming *E. coli* at short time intervals, the MSD is proportional to  $\Delta t^2$  (Fig. 3.3a), indicating the cells swim ballistically during a run. For times much larger than the mean run time  $\tau_R$ , the cells tumble, decorrelating their motion. Thus for very large  $\Delta t \gg \tau_R$ , the motion is diffusive as seen in Fig. 3.3(a).

For *E. coli*, the dynamics can be captured using the relationship  $\text{MSD}(\Delta t) = 4D_T\Delta t(1 - e^{-(\Delta t/\tau)})$ , where  $\tau$  is a typical crossover time marking the transition from ballistic to diffusive motion. The crossover time depends on the mean run time  $\tau_R$  corrected by a factor that accounts for the mean cosine of the turning angle  $\alpha$  such that  $\tau = \tau_R/(1 - \alpha)$  [41]. The MSD is proportional to  $4D_T(\Delta t)^2/\tau$  for  $\Delta t \ll \tau_R$  and to  $4D_T\Delta t$  for  $\Delta t \gg \tau_R$ . By fitting this relationship to the MSD data in Fig. 3.3(a), I find that the translational diffusion coefficient  $D_T$  increases significantly from 10.8 to 101.6  $\mu\text{m}^2/\text{s}$  as polymer concentration (and viscosity) increases (Fig. 3.3c). The crossover time

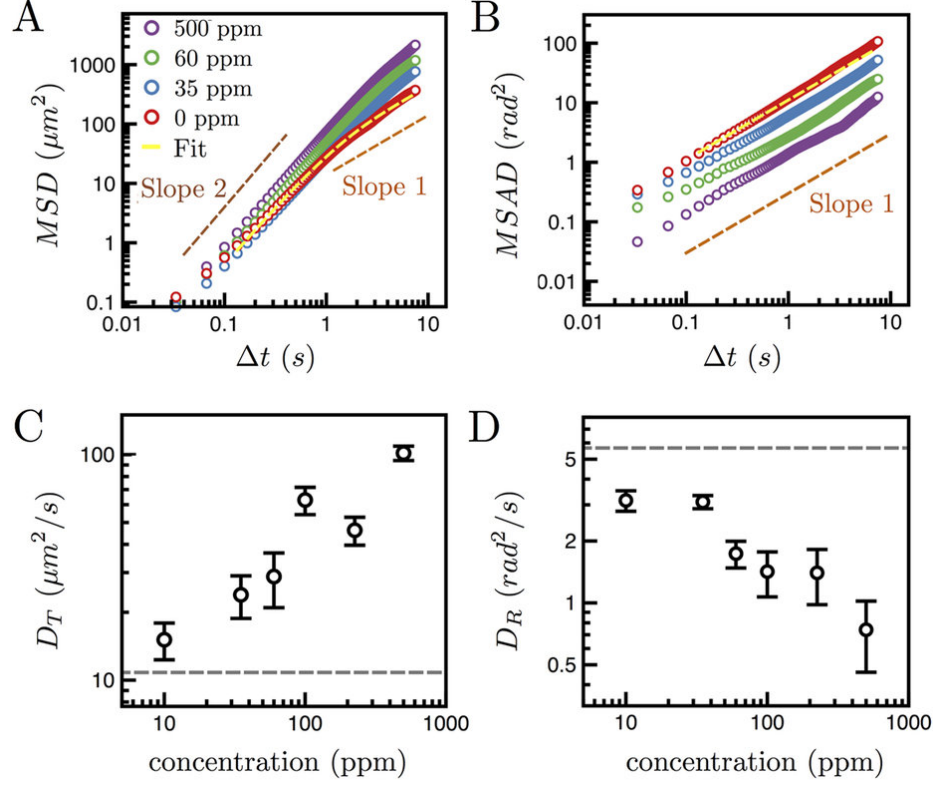


Figure 3.3: Statistical measures characterizing cell trajectories. (A) The mean-square displacement for cells in buffer and CMC solutions (concentration  $c = 0, 35, 60, 100$  ppm,  $\text{MW}=7 \times 10^5$ ). At short times,  $\Delta t < \tau_R$ , where  $\tau_R$  is the mean run time, the cell motion is ballistic, and  $\text{MSD} \propto (\Delta t)^2$ . At longer times,  $\Delta t > \tau_R$ , the cell motion is diffusive and  $\text{MSD} \propto \Delta t$ . As  $c$  increases, the magnitudes of the MSD curves increase. (B) The mean-square angular displacement of cells in buffer and polymeric solutions increases linearly over time, indicating diffusive reorientations. (C) The translational diffusion coefficient increases from  $10.8$  to  $101.6 \mu\text{m}^2/\text{s}$  as  $c$  increases. The result for buffer ( $c = 0$  ppm) provides a reference (dashed line). (D) The rotational diffusion coefficient decreases from  $5.6$  to  $0.7 \text{ rad}^2/\text{s}$  as  $c$  increases, reflecting suppressed tumbling in polymeric solutions.

$\tau$  also increases with polymer concentration from 0.9 to 4.8 s (Appendix B.3). This suggests an enhancement in mean cell run time, consistent with the observed suppressed tumbling in polymer solutions (Fig. 3.1).

Next, the *E. coli* rotational diffusivity is calculated through the mean-squared angular displacement, defined here as  $MSAD(\Delta t) = |\theta(t_0 + \Delta t) - \theta(t_0)|^2$ . I use the cell orientation  $\theta$  to construct the MSAD data, which is shown in Fig. 3.3b. Then, the data is fitted to  $MSAD = 2D_R\Delta t$  in order to obtain the effective rotational diffusion coefficient  $D_R$ . For the buffer solution case,  $D_R$  is approximately 5.6 rad<sup>2</sup>/s (Fig. 3.3d). For cells swimming in CMC solutions, the values of  $D_R$  diminish to 0.7 rad<sup>2</sup>/s ( $c = 500$  ppm). The decrease in rotational diffusivity is also consistent with the appearance of nearly straight trajectories in polymeric solutions (Fig. 3.1b).

To connect the time-averaged statistical quantities of swimming *E. coli* to their instantaneous kinematics, I measure the mean run and tumble times as shown in Fig. 3.4(a) and 3.4(b). Mean run time is defined as the time intervals between successive tumbles, identified here by rapid drops in velocity (Fig. 3.2b). I find as polymer (CMC) is added to the fluids, the run times increase from approximately 0.9 to 3.5 s (Fig. 3.4). This enhancement in run time is consistent with the nearly straight trajectories (c.f. Fig. 3.1b) and the reduction in rotational diffusivity in polymeric solutions. The mean tumble times (Fig. 3.4b) are defined as the mean time intervals between runs. This quantity also increases (from 0.2 to 0.4 s) with polymer concentration. This observed increase in both run and tumble times is in marked contrast to chemotactic cells in chemical gradients in which run times increase but tumble times remain constant [28]. Thus, the *E. coli* biochemical signaling network cannot solely explain my results, suggesting that the fluid rheology is affecting the cell motility behavior. I note that the mean run and tumble times are consistent with previous measurements [29].

In order to investigate which fluid properties contribute to the changes in *E. coli* run and tumble times, I measure the rotational diffusivity  $D_R$  in fluids with varying rheological properties. I note that  $D_R$  for an *E. coli* is inversely proportional to the mean time  $\tau_R$  (see Appendix B.4 for details) [41]. These fluids are polymeric solutions of CMC of different molecular weight (MW) and XG. Figure 3.4c shows the cell rotational diffusivity  $D_R$  as a function of fluid viscosity  $\mu$ . The data clearly shows that, for all solutions,  $D_R$  decreases with  $\mu$ . The agreement in the data for multiple fluids and two types of polymers indicates that  $D_R$  is independent of the variations in elasticity and

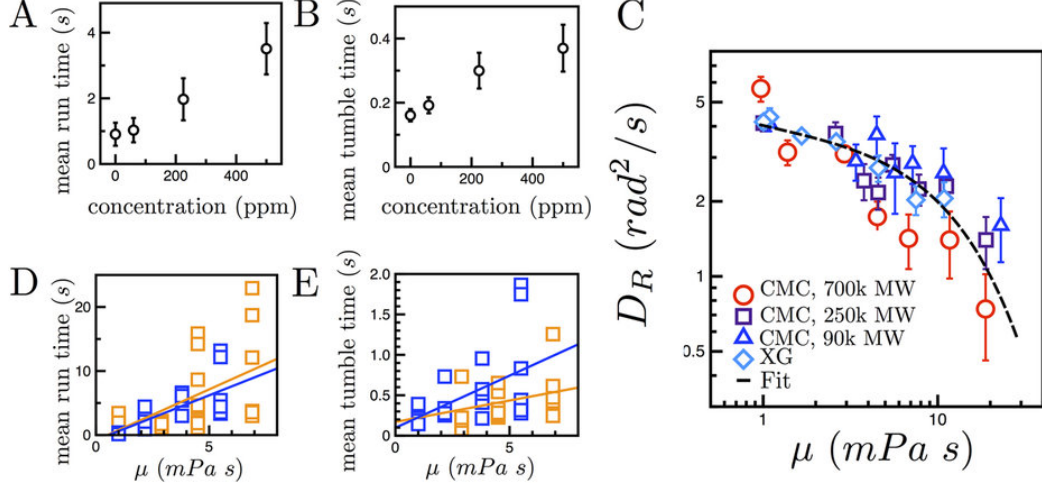


Figure 3.4: Viscosity suppresses tumbling. (A) The mean run time increases from 0.95 to 3.51 s as the CMC polymer concentration  $c$  increases (MW =  $7 \times 10^5$ ). (B) The mean tumble time also increases with  $c$  from 0.16 to 0.37 s. (C) The rotational diffusion coefficient decreases with viscosity for the CMC and XG solutions, indicating that suppressed tumbling is nearly independent of MW or molecule, and is captured by proposed model. (D) The mean run and (E) mean tumble times for individual tethered cells in Newtonian (PEG, blue squares) and viscoelastic (CMC, orange squares) fluids as a function of  $\mu$ . Lines correspond to regression analysis (Methods).

shear-thinning properties (Appendix B.1). The decrease in  $D_R$ , which scales as  $D_R \sim 1/\tau_R$ , thus indicates an increase in run times  $D_R$ , and the collapse in Fig. 3.4(c) strongly suggests that  $D_R$  predominately depends on fluid viscosity.

### 3.3.3 Enhancement in cell run time

To better understand the observed enhancement in run and tumble times with  $\mu$ , I perform experiments in which the run and tumble states of the cell can be directly visualized by the rotation of tethered *E. coli*. Sticky-flagellated mutant *E. coli* can tether to glass slides [31]. The resulting counter-clockwise (CCW) or clockwise (CW), rotation of cell bodies corresponds to the run or tumble state of the motor, respectively (Appendix B.2). Figures 3.4(d) and 3.4(e) show the mean run and tumble times as a function of viscosity for individual cells in viscoelastic (CMC) and Newtonian (PEG) fluids. The mean run and tumble times tend to increase with viscosity for both fluids. Linear regression analysis reveals that this increase is statistically equivalent in the Newtonian and viscoelastic fluids (Appendix B.2). The tethering results bolster my observations that the changes in *E. coli* run and tumble times are mainly due to changes in viscous stresses. I propose that as viscous

stresses increase, the mechanical (viscous) load on the cell also increases which in turn affects the cell motor switching rates between run and tumble states. Previous experiments have in fact shown that mechanical loading can significantly affect motor switching rates [42, 43], where mechanical loads were introduced by attaching latex beads to the flagellar stubs.

To interpret these results (Fig. 3.4), I suggest a minimal model valid at high loads (as in my experiments) that treats motor switching as an activated process with rates controlled by effective energy barriers that need to be overcome for potential tumbles to occur [43, 44]. In the absence of external loading, the motor switching rate  $k^*$  depends on the chemical binding rate of a signaling molecule Che-Y to the cell motor. Assuming that viscous drag on the cell flagella presents an additional energy barrier to switch from one state to the other, the switching rate  $k$  is modified to  $k \propto k^* \exp(-\beta M/k_B T)$ , where  $M$  is a characteristic external torque generated by viscous drag on the flagella and  $\beta$  is a characteristic angle determined by the internal details of the coupling between the flagella and motor necessary to switch states (Appendix B.2). As fluid viscosity increases, the torque  $M$  increases, and the switching rate decreases by a factor  $\exp(-\beta M/k_B T)$ , consistent with the observed enhancement in run and tumble times (Fig. 3.4a-b,d-e).

As the motor switching rates diminish with increased viscous loading, the cell rotational diffusion  $D_R$  is suppressed (Fig. 3.4c). This decrease in  $D_R$  may be interpreted as follows. The rotational diffusivity of an *E. coli* is a sum of its Brownian rotational diffusivity  $D_R^0$ , arising due to passive thermal motion, and its active rotational diffusivity due to tumbles [41]. The Brownian rotational diffusion of a particle is  $D_R^0 = k_B T / f_0 \mu$ , where  $f_0$  is the geometry-dependent resistivity according to the Stokes-Einstein relationship. Assuming that the *E. coli* body is an ellipsoid (2  $\mu\text{m}$  long and 1  $\mu\text{m}$  wide),  $f_0$  is approximately 9.45  $\mu\text{m}^3$  [45]. If the mean run time increases as  $\exp(\beta M/k_B T)$  and the torque  $M$  is proportional to viscosity  $\mu$ , then the rotational diffusion coefficient follows  $D_R = D_R^0 + A^* k^* e^{-\beta M/k_B T} = (k_B T) / (f_0 \mu) + A e^{-B \mu}$ . By fixing  $f_0$  to 9.45  $\mu\text{m}^3$  and temperature  $T$  to 22  $^\circ\text{C}$ , I fit this equation to the data in Fig. 3.4c and obtain  $A = 3.85 \text{ rad}^2/\text{s}$  and  $B = 68.3 (\text{Pa s})^{-1}$ . The parameter  $A$  is a constant rotational diffusion based on the cells intrinsic motor switching rate  $k^*$ . The parameter  $B$ , defined here as  $B = \beta M/k_B T \mu$ , corresponds to a motor torque  $M = 650 \text{ pN nm}$  in water [34] and a characteristic angle  $\beta = 0.025^\circ$  (Appendix B.2). The model seems to capture the main features of the  $D_R$  versus viscosity data and further supports the idea that the decrease in rotational diffusion of swimming *E. coli* is due mainly to mechanical loading of the motor



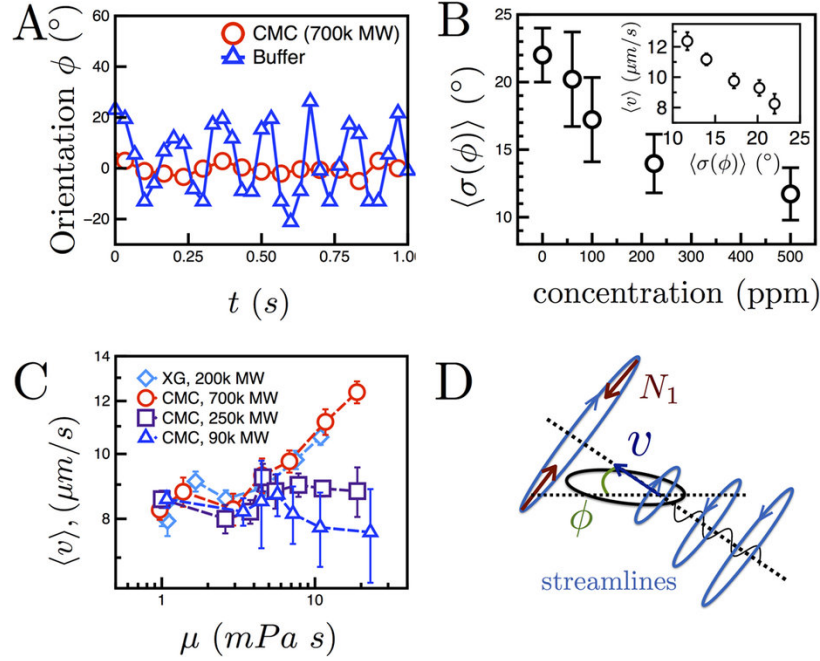


Figure 3.5: Elasticity suppresses wobbling while increasing cell velocity. (A) The body orientation  $\phi$  versus time for a cell in buffer and polymer solutions (CMC, MW =  $7 \times 10^5$ ,  $c = 500$  ppm). In buffer, the cell wobbling amplitude is significantly larger than in the polymer solution. (B) The degree of wobbling,  $\langle\sigma(\phi)\rangle$ , decreases from 22.0 to 11.7 as the CMC polymer concentration increases. (Inset) Mean cell velocity decreases with  $\langle\sigma(\phi)\rangle$ , illustrating that cells which wobble less swim faster. (C) Mean cell velocity versus viscosity for solutions of CMC of varying molecular weight and XG. The velocity increases with  $\mu$  for the largest MW of CMC but remains nearly constant in the lowest MW. (D) As *E. coli* swim, they generate a fluid flow with curved streamlines [46]. This shear can stretch polymers, producing first normal stress differences  $N_1$ . Under these curved streamlines, a volume force ( $N_1/r$ ) points inward to the cell body, suppressing wobbling, and allowing cells to translate at higher  $v$ .

via viscous drag.

### 3.3.4 Enhancement in *E. coli* swimming speed and wobbling suppression

Next, I investigate the enhancement of cell velocity with increasing polymer concentration (Fig. 3.2c). The increase in polymer (CMC) concentration leads to an increase in fluid viscosity  $\mu$  and elasticity (Appendix B.1). Here I argue that the observed increase in cell velocity is due to elastic stresses, which suppress cell wobbling (as shown in Fig. 3.1 (e,f)) and allow the cells to translate more efficiently. A decrease in *E. coli* wobbling has been previously observed in polymeric solutions [34],

but the connection to cell swimming speed has not been made. I begin by tracking the orientation of the cell body  $\phi$  relative to the direction of its trajectory in buffer and CMC ( $c = 500$  ppm, MW =  $7.0 \times 10^5$ ) solutions (Fig 3.5a). The estimated wobble angles are approximately  $20^\circ$  and  $5^\circ$  in buffer and CMC solutions, respectively. There is, therefore, a significant suppression of wobbling as polymer concentration is increased. I can further characterize this suppression by computing the mean standard deviation of  $\phi$ ,  $\langle\sigma(\phi)\rangle$ , over many cells. This quantity  $\langle\sigma(\phi)\rangle$  characterizes the degree of wobbling. Figure 3.5b shows that the quantity  $\langle\sigma(\phi)\rangle$  decreases from  $22.0^\circ$  to  $11.7^\circ$  with increasing CMC polymer concentration. The decrease in  $\langle\sigma(\phi)\rangle$  signifies a change in the cell swimming kinematic or stroke. Also, Fig. 3.5(b, inset) shows that the cell velocity  $\langle v \rangle$  is inversely proportional to the degree of wobbling  $\langle\sigma(\phi)\rangle$ ; that is, a suppression in wobbling leads to an increase in cell velocity.

To distinguish between elastic and viscous effects, I measure *E. coli* mean cell velocity  $\langle v \rangle$  and degree of wobbling  $\langle\sigma(\phi)\rangle$  in CMC and XG solutions. Figure 3.5(c) shows  $\langle v \rangle$  as a function of fluid viscosity  $\mu$  for CMC solutions of varying MW and a XG solution. While  $\langle v \rangle$  increases with  $\mu$  for the highest molecular weight CMC and XG solutions, the relative enhancement in  $\langle v \rangle$  diminishes as the CMC molecular weight (and thus elasticity) decreases. This is evident if one considers  $\mu = 11$  mPa s, where  $\langle v \rangle$  clearly decreases with the MW of CMC. This observation suggests that *E. coli* swimming speed  $\langle v \rangle$  is not a function of fluid viscosity. Also, it appears that shear-thinning effects are negligible since the values of  $\langle v \rangle$  for the highest molecular weight CMC (weakly shear-thinning, power law index = 0.7) and XG (strongly shear-thinning, power law index = 0.5) solution in Fig. 3.5(c) are indistinguishable. The increase in  $\langle v \rangle$  with CMC molecular weight (MW) is also consistent with a simultaneous decrease in wobbling (Appendix B.5). I conclude that the suppression of cell wobbling due to fluid elasticity results in an increase in cell swimming velocity  $\langle v \rangle$ .

What may cause fluid elasticity to suppress wobbling and thereby increase  $\langle v \rangle$ ? I suggest a mechanism supported by my experimental observations by which this is accomplished. As a single *E. coli* swims through a fluid, it generates a flow with curved streamlines [46] due to the rotating flagella and the concomitant counter-rotation of its body, as shown schematically in Fig. 3.5d. In flow, shear can stretch flexible polymer molecules [47] (such as CMC) and generate first normal stress differences  $N_1$ . The combination of shear and curved streamlines produce a (volume) force  $N_1/r$ , which points inward in the radial direction ( $r$ ). I propose that this force, which for an *E. coli*

cell points into the cell body (Fig. 3.5d) and perpendicular to the cell’s swimming direction, causes the cell body to align with the projected direction of motion. The resultant decrease in wobbling amplitude would ultimately change the form (shape) of the swimming trajectory and increase the cell swimming velocity  $\langle v \rangle$ . Thus, I propose that  $\langle v \rangle$  increases with polymer concentration (Fig. 3.2c) primarily because of the appearance of the force  $N_1/r$ , which is able to suppress wobbling  $\phi$  and cells that wobble less inherently swim faster. The combination of reduced wobbling (and thus higher  $\langle v \rangle$ ) with enhanced run times results in straighter, longer trajectories in polymeric solutions (Fig. 3.1b).

### 3.3.5 Polymer dynamics in bacterial-generated flows

This argument however is contingent on the expectation that swimming *E. coli* cells can actually generate flow fields strong enough to stretch polymer molecules and induce elastic stresses in a fluid. In order to gain further insight and verify that this is the case, I directly visualize the interaction of model polymer molecules and tethered *E. coli*.  $\lambda$ -DNA molecules are fluorescently stained and suspended in a buffer solution with mutant *E. coli* cells (Methods). These mutants contain sticky-flagella that can be tethered with ease and additionally also only ‘run’. As a result, there is a stable, three dimensional, time-dependent flow generated by the CCW-rotation of the tethered *E. coli* cell. I track the configurations of nearby DNA molecules over time, an example of which is shown in Fig. 3.6(a). Also shown in Fig. 3.6(a) are the cell body and a nearby DNA molecule tracks over time. The sample snapshots ( $\Delta t = 0.4$  s) qualitatively show that the DNA molecular configuration evolves over time: it begins as a sphere, elongates and curves around the streamlines. These representative snapshots provide evidence that flows generated by moving *E. coli* are capable of stretching nearby polymer molecules, and thus induce elastic stresses in polymeric solutions.

To quantify the above observations, I measure the molecule (DNA) stretch length  $\ell$  for two cases: (i) the absence of cells (i.e., no flow) and (ii) near a tethered cell, approximately  $5 \mu\text{m}$  away from the cell. The distributions of DNA stretch lengths – normalized by the  $\lambda$ -DNA contour length ( $\ell_c = 22.0 \mu\text{m}$  [48]) – are shown in Fig. 3.6 (b) for both cases. In the absence of cells, the polymer molecules are in equilibrium and their configurations fluctuate randomly due to Brownian forces. The observed minimum  $\ell/\ell_c$  in Fig. 3.6b corresponds to a length  $l$  of approximately  $1.4 \mu\text{m}$ , consistent with the length ( $2R_g$ ) of a polymer with the inferred radius of gyration,  $R_g \approx 0.7 \mu\text{m}$  [48]. The peak in

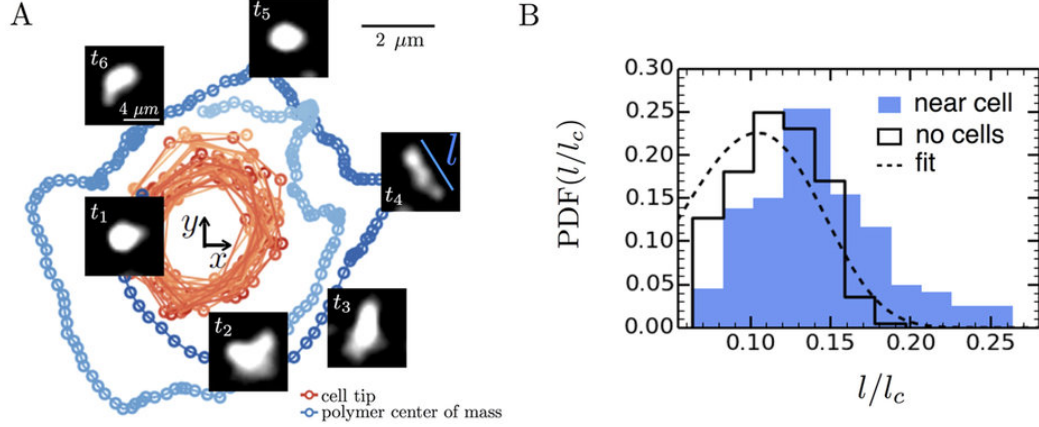


Figure 3.6: Polymer stretching by a tethered *E. coli* cell. (A) The tethered cell rotates counter-clockwise (CCW) in a steady, circular trajectory. An untethered polymer molecule near the cell also rotates CCW due to hydrodynamic interactions with the cell. Sample configurations of the polymer ( $t = 0.4$  s) show extension and alignment with the flow. (B) The distribution of the normalized lengths for the polymer near the tethered cell ( $2.5 \mu\text{m}$ ) is shifted to the right of the distribution in the absence of cells, suggesting that cell-generated flows stretch polymers and produce elastic stresses. The dashed line is the fit of the distribution for a self-avoiding chain at equilibrium (Appendix B.7) [49,50].

the distribution is followed by a rapid decay, which seems to follow the exponential decay of the theoretical end-to-end distance distribution (dashed line in Fig. 3.6b) of a self-avoiding polymer chain at equilibrium [49] and is also consistent with previous experimental measurements of  $\lambda$ -DNA [48, 50]. Compared to the DNA at equilibrium case (in the absence of cells), the length distribution of a polymer near a cell broadens and extends to higher values, reaching a maximum of approximately  $7R_g$  (Fig. 3.6b). For the DNA, this observed shift in the distribution corresponds to an applied force of approximately 4.5 fN (Appendix B.6) and is in reasonable agreement with expected viscous extensional forces generated by the tethered cell (Appendix B.2). The shift illustrates that the flow generated by the motion of the *E. coli* body in a fluid is indeed able to stretch polymer molecules beyond their equilibrium configuration.

To compare the DNA polymer extension by the tethered *E. coli* (Fig. 3.6) to the potential polymer extension by freely-swimming *E. coli* (Fig. 3.5), I estimate the Weissenberg number  $Wi$  for both experiments. The Weissenberg number  $Wi = \lambda \dot{\gamma}$ , where  $\lambda$  and  $\dot{\gamma}$  are the fluid relaxation time and applied shear rates. I find that the  $Wi$  of the CMC and DNA polymer experiments are comparable, at approximately 13 and 8 respectively (SI7). This suggests that the CMC polymers near swimming cells exhibit similar stretching to the DNA polymer (Fig. 3.6) and may generate

elastic stresses.

My experiments highlight the complementary roles played by the elastic and viscous properties of complex fluids through which *E. coli* swim. For freely swimming *E. coli*, the stretching of nearby polymer molecules can lead to extra elastic stresses in the fluid [47], which act to align the cell body, reduce the degree of wobbling (Fig. 3.5b), and ultimately enhance cell velocity (Fig. 3.5). This increase in cell velocity with elasticity combined with the observed suppression of cell tumbles due to enhanced viscous loading (Fig. 3.4a) dramatically enhances the overall diffusivity and transport properties of bacterial cells (Fig. 3.3a,c) in fluids with small amounts of polymer.

### 3.4 Conclusions

Fluid properties such as viscosity and elasticity have been shown to significantly affect the motility of microorganisms. In this article, I investigated the effects of fluid material properties on the motility of *E. coli*. Using polymeric solutions of varying molecular weight, I found that the viscosity and elasticity can independently alter the swimming and transport of bacteria. In particular, I find that fluid viscosity suppresses cell tumbling, while fluid elasticity increases cell velocity. I also found that the flow generated by swimming bacteria influences the dynamics of polymers in solution, in such a way that the cells motility is enhanced. Direct visualization of individual tethered cells and nearby polymers reveals that cell-generated flows can indeed stretch and align polymer molecules, actively inducing local elastic stresses, which in turn act on the cell. These results complement recent simulations that predict unusual stretching in model polymers in the presence of multiple bacteria [51]. More broadly, my experiments highlight the need to consider the interactions between single polymer molecules and individual swimming microorganisms. These interactions and their emergent feedback mechanisms are crucial to many outstanding issues in engineering, biology, and medicine, such as the design of swimming micro-robots [12, 52] and the possible means to control biofilm formations [3, 4, 6, 14, 53]. Finally, my work emphasizes the need to study microorganisms in their natural, non-ideal environment, where complex material properties dramatically alter their macroscopic transport behavior.

# Bibliography

- [1] Cosson J. 1996. **A moving image of flagella: News and views on the mechanisms involved in axonemal beating.** *Cell Biology International* 20:83-94.
- [2] Liu R, Ochman H. 2007. **Stepwise formation of the bacterial flagellar system.** *Proceedings of the National Academy of Sciences* 104:17.
- [3] Josenhans C, Suerbaum S. 2002. **The role of motility as a virulence factor in bacteria.** *Int. J. Med. Microbiol.* 291:605-614.
- [4] Costerton JW, Stewart PS, Greenberg EP. 1999. **Bacterial biofilms: A common cause of persistent infections.** *Science* 284:1318-1322.
- [5] Ottemann KM, Lowenthal AC. 2002. **Helicobacter pylori uses motility for initial colonization and to obtain robust infection.** *Infect. Immun.* 70:1984-1990.
- [6] Livorsi DJ, Stenehjem E, Stephens DS. 2011. **Virulence factors of gram-negative bacteria in sepsis with a focus on Neisseria meningitidis.** *Contrib. Microbiol.* 17:31-47.
- [7] Durham WM, *et al.*, 2013. **Turbulence drives microscale patches of motile phytoplankton.** *Nature Communications* 4:2148.
- [8] Valentine DL, *et al.*. 2010. **Propane respiration jump-starts microbial response to a deep oil spill.** *Science* 330:208.
- [9] Lauga E. 2009. **Life at high Deborah number.** *EPL* 86:64001.
- [10] Shen XN, Arratia PE. 2011. **Undulatory swimming in viscoelastic fluids.** *Physical Review Letters* 106:208101.

- [11] Yeomans JM, Pushkin DO, Shum H. 2014. **An introduction to the hydrodynamics of swimming microorganisms.** *Eur. Phys. J. Special Topics* 223:1771-1785.
- [12] Qiu T, *et al.* 2014. **Swimming by reciprocal motion at low Reynolds number.** *Nature Communications* 5:5119.
- [13] Celli JP, *et al.* 2009. **Helicobacter pylori moves through mucus by reducing mucin viscoelasticity.** *Proceedings of the National Academy of Sciences* 106:14321-14326.
- [14] Lewis K. 2007. **Persister cells, dormancy and infectious disease.** *Nat. Rev. Microbiol.* 5:48-56.
- [15] Fauci L, Dillon R. 2006. **Biofluidmechanics of reproduction.** *Annu. Rev. Fluid Mech* 38:371-394.
- [16] Lai SK, Wang Y, Wirtz D, Hanes J. 2009. **Micro-and macrorheology of mucus.** *Adv. Drug Deliver. Rev.* 61:86-100.
- [17] Espinosa-Garcia J, Lauga E, Zenit R. 2013. **Fluid elasticity increases the locomotion of flexible swimmers.** *Physics of Fluids* 25:031701.
- [18] Liu B, Powers TR, Breuer KS. 2011. **Force-free swimming of a model helical flagellum in viscoelastic fluids.** *Proceedings of the National Academy of Sciences* 108:19516-19520.
- [19] Spagnolie SE, Liu B, Powers TR. 2013. **Locomotion of helical bodies in viscoelastic fluids: Enhanced swimming at large helical amplitudes.** *Physical Review Letters* 111:068101.
- [20] Thomases B, Guy RD. 2014. **Mechanisms of elastic enhancement and hindrance for finite-length undulatory swimmers in viscoelastic fluids.** *Physical Review Letters* 113:98102.
- [21] Teran J, Fauci L, Shelley M. 2010. **Viscoelastic fluid response can increase the speed and efficiency of a free swimmer.** *Physical Review Letters* 104:038101.
- [22] Lauga E. 2007. **Propulsion in a viscoelastic fluid.** *Physics of Fluids* 19:083104.
- [23] Qin B *et al.* 2015. **Flagellar Kinematics and Swimming of Algal Cells in Viscoelastic Fluids.** *Scientific Reports* 5:9190.

- [24] Gagnon DA, Keim NC, Arratia PE. 2014. **Undulatory swimming in shear-thinning fluids: experiments with *Caenorhabditis elegans*.** *J. Fluid Mech.* 758:R3.
- [25] Martinez V, *et al.*. 2014. **Flagellated bacterial motility in polymer solutions.** *Proceedings of the National Academy of Sciences* 111:17771-17776.
- [26] Vélez-Cordero J, Lauga E. 2012. **Waving transport and propulsion in a generalized Newtonian fluid.** *J. Fluid Mech.* 199:37-50.
- [27] Polin M, *et al.* 2009. **Chlamydomonas swims with two “gears” in a eukaryotic version of run-and-tumble locomotion.** *Science* 325:487-490.
- [28] Berg HC. 2004. ***E. coli* in Motion.** Springer-Verlag New York, Inc., 175 Fifth Avenue, New York, NY 10010, USA.
- [29] Berg HC, Brown DA. 1972. **Chemotaxis in *Escherichia coli* analysed by three-dimensional tracking.** *Nature* 239: 500-504.
- [30] Saragosti J, Silberzan P, Buguin A. 2012. **Modeling *E. coli* tumbles by rotational diffusion: Implications for chemotaxis.** *PLoS ONE* 7:e35412.
- [31] Sowa Y, Berry RM. 2008. **Bacterial flagellar motor.** *Quarterly Reviews of Biophysics* 41:103-132.
- [32] Sillankorva SM, Oliveira H, Azeredo J. 2012. **Bacteriophages and their role in food safety.** *Int. J. Microbiology* 2012.
- [33] Koser AE, Pan L, Keim NC, Arratia PE. 2013. **Measuring material relaxation and creep recovery in a microfluidic device.** *Lab on a Chip* 13:1850-1853.
- [34] Darnton NC, Turner L, Rojevsky S, Berg HC. 2006. **On torque and tumbling in swimming *Escherichia coli*.** *Journal of Bacteriology* 189:1756-1764.
- [35] Hyon Y, *et al.* 2012. **The wiggling trajectories of bacteria.** *Journal of Fluid Mechanics* 705:58-76.
- [36] Amsler CD, Cho M, Matsumura P. 1993. **Multiple factors underlying the maximum motility of *Escherichia coli* as cultures enter post-exponential growth.** *J. Bacteriol.* 175:6238-6244.



- [37] Berg HC, Turner L. 1979. **Movement of microorganisms in viscous environments.** *Nature* 278:349-351.
- [38] Rodenborn, B *et al.*. 2013. **Propulsion of microorganisms by a helical flagellum.** *Proceedings of the National Academy of Sciences* 110:E338-E347.
- [39] Schneider WR, Doetsch RN. 1974. **Effect of viscosity on bacterial motility.** *J. Bacteriology* 117:696-701.
- [40] Magariyama Y, Kudo S. 2002. **A mathematical explanation of an increase in bacterial swimming speed with viscosity in linear-polymer solutions.** *Biophysical Journal* 83:733-739.
- [41] Lovely PS, Dahlquist FW. 1975. **Statistical measures of bacterial motility and chemotaxis.** *J. theor. Biol.* 50:477-496.
- [42] Fahrner KA, Ryu WS, Berg HC. 2003. **Biomechanics: Bacterial flagellar switching under load.** *Nature* 423:938.
- [43] Yuan J, Fahrner KA, Berg HC. 2009. **Switching of the bacterial flagellar motor near zero load.** *J. Mol. Biol.* 390:394-400.
- [44] Duke TAJ, Novère NL, Bray D. 2001. **Conformational spread in a ring of proteins: A stochastic approach to allostery.** *J. Mol. Biol.* 308:541-553.
- [45] Perrin F. 1934. **Le mouvement Brownien et la réalité moléculaire.** *J. Phys. Rad. Ser.* 5:497-511.
- [46] Watari N, Larson RG. 1998. **The hydrodynamics of a run-and-tumble bacterium propelled by polymorphic helical flagella.** *Biophysical Journal* 98:12-17.
- [47] Pakdel P, McKinley GH. 1996. **Elastic instability and curved streamlines.** *Physical Review Letters* 77:2459.
- [48] Smith DF, Babcock HP, Chu, S. 1999. **Single-polymer dynamics in steady shear flow.** *Science* 283:1724-1727.
- [49] de Gennes PG. 1979. **Scaling Concepts in Polymer Physics.** *Cornell University Press.*

- [50] Valle F, Favre M, De Los Rios P, Rosa A, Dietler G. 2005. **Scaling exponents and probability distributions of DNA end-to-end distance.** *Physical Review Letters* 95:158105.
- [51] Kaiser A, Lowen H. 2014. **Unusual swelling of a polymer in a bacterial bath.** *The Journal of chemical physics* 141:044903.
- [52] Peyer KE, Zhang L, Nelson BJ. 2013. **Bio-inspired magnetic swimming microrobots for biomedical applications.** *Nanoscale* 5:1259-1272.
- [53] Drescher K, Shen Y, Bassler BL, Stone HA. 2013. **Biofilm streamers cause catastrophic disruption of flow with consequences for environmental and medical systems.** *Proceedings of the National Academy of Sciences* 110:4345-4350.
- [54] Crocker J, Grier D. 1996. **Methods of digital video microscopy for colloidal studies.** *J. Colloid. Interf. Sci.* 179:298-310.

# Chapter 4

## Phase dynamics in active fluids: The growth and form of active-passive phase boundaries in dense swarms of bacteria.

### 4.1 Introduction

Understanding and predicting which phases of matter emerge in nature has been a driving question of scientists for centuries. Classically, thermodynamics describes if certain phases will appear and kinetic theory describes how. For instance, an out-of-equilibrium phase-separated system of passive particles relaxes toward thermal equilibrium by the flux of particles across phase boundaries at a rate set by the gradient in chemical potential,  $J = \nabla\mu$ . For systems of active particles, that is self-propelling particles, no such unifying framework has been established.

Active particles are an essential component of living materials, which convert chemical energy into particle motion at scales that range from cargo-carrying myosin motors of the cytoplasm [1], propulsive-flagella of cells [2], and to wound healing [3] in collections of cells. The internal supply

and injection of energy within the material continually drives the system out-of-equilibrium. These materials are unable to relax to a thermodynamic equilibrium state, and over the past few decades, scientists have uncovered dynamic quasi-steady states of active matter, such as asters [4], waves [5], and dynamic collective flows [6, 7] that appear at high particle densities and particle velocities.

Recently, experimental studies have observed organization of active materials into seemingly phase-separated regions. These observations include the formation of liquid-crystal order of motor-activated microtubules during cell mitosis [8], the formation of membrane-less organelles that resemble liquid-liquid phase transitions in the active cytoplasm [9], the aggregation of swimming bacteria within polymer solutions [10], and the clustering of synthetic rheotactic particles into dense and dilute phases [11]. Similar dense and dilute phase separations has been observed in simulations of active Brownian spheres [12, 13], even in the absence of any attractive particle interactions. Theories [14, 15] have introduced an active contribution to the pressure, due to the self-propulsion of the swimmers, that explains the origin of this active phase separation process in the absence of any hydrodynamic interactions and collective flows. Collective flows naturally emerge in many active materials, including swarming bacteria.

Swarming bacteria are a common and beautiful model system of active matter [16–25]. Bacteria live in fluids and on surfaces [18, 26]. At surfaces such as soft agar gels, many Gram-negative flagellated bacteria – including *Escherichia coli* [20, 21], *Pseudomonas aeruginosa*, *Vibrio parahaemolyticus*, *Bacillus subtilis* [24], and *Serratia marcescens* [22, 23] – differentiate into ‘swarmer cells’, by elongating their cell body (from 2  $\mu\text{m}$  to 5–10  $\mu\text{m}$ ), expressing numerous flagella (10–100), and collectively moving in dynamic bacterial ‘rafts’ or densely-packed clusters of aligned cells that merge and dissolve in time [16–18, 24]. These dense packs (20 cells) move at velocities more than twice the speed of individual cells (40 and 15  $\mu\text{m/s}$ ) [24], allowing the bacterial colony as a whole to expand rapidly, at rates of 2–10 m/s - much higher than other surface motility forms, such as twitching, gliding, and spreading at  $\sim 0.1$  m/s [18]. Unlike these other forms of motility, swarming exhibits fascinating collective motions with patterns of jets and swirls [19, 22, 24]. This collective motion is implicated in increased antibiotic resistance [17, 27, 28], which could be due to the isolated clustering of damaged cells within swarms [29]. The clustering and transport of fungal spores [30] and other bacterial species [31] within swarms can provide mutual assistance and cooperation in gaining new environments [17, 32]. In contrast, when swarms of different strains meet, as in the

bacteria *Proteus*, they compete, forming between them a sharp boundary [17,28]. Thus, the role of boundaries - whether created or annihilated by swarming bacteria - play an important role in their motility and function.

Despite its importance, the influence of collective flows on the stability and propagation of boundaries is largely unknown. Equally important is the question how do boundaries affect collective flows? This unknown boundary-flow interaction is central to understanding the growth and form of active phase boundaries and the structure and dynamics of transient states in active environments.

To this end, I investigate the structure and dynamics of an active-passive interface in a swarm of *Serratia marcescens*. The active-passive interface is created in a non-chemical and controllable way by quenching a region of the swarm by exposing it to UV light, which permanently damages or kills the cells. After exposure, the swarming bacteria dissolve the passive phase of bacteria and the system evolves from an active/passive phase-separated system into a homogenous mixture. I define a dynamic order parameter that characterizes the mean position and width of the interface over time. For a flat interface, the mean boundary position propagates at a relatively constant velocity, which suggest that particle flux across the interface is driven by an active pressure and fluid flow. For interfaces with corners, the mean interface speed increases with the interface curvature over time. I find that the interface stabilizes the dynamic flow of the bacterial, generating larger and longer-lasting vortex structures compared to the bulk. The vortices, in return, etch the interface, molding the interface's structure and curvature. I find that the interface velocity correlates with the interface curvature and bacterial flow, suggesting an active analog to the Gibbs-Thompson boundary. My results have important implications for understanding transitions between equilibrium-like states in active materials and for understanding how bacteria shape boundaries, compete for new environments, and mix particulates, such as damaged/dead bacteria, extracellular polymers, vesicles, and other microbial species.

## 4.2 Methods

My active-passive interfaces are created in swarms of *Serratia marcescens*. *Serratia marcescens* are a canonical organism for swarming studies [22,23]. *Serratia marcescens* are flagellated rod-shaped cells with a width of 1  $\mu\text{m}$  and a length of 6-7  $\mu\text{m}$  when swarming. Swarms of *Serratia marcescens* (ATCC

274) are grown on agar substrates. Agar plates are inoculated with cells from a frozen glycerol stock and are incubated at 34 degrees Celsius. From the inoculation sight, a bacterial colony forms and grows outward. After 8 to 16 hours, swarming motility is observed at the expanding edge of the cell colony, as shown in Fig. 4.1a.

At this edge, the cells are a monolayer thick and exhibit local orientational order that resembles a nematic liquid crystal, as shown in (Fig. 4.1aii). Figure 4.1aiii shows that this orientational structure includes defects, a common feature of active nematic systems [7,12].

It is in this region of the swarm that I create an active-passive phase-separated system. To do this, I essentially quench a portion of the swarm by exposing it to UV light (Fig. 4.1b), which damages and kills bacterial cells. These immobile cells form a passive phase that shares a sharp boundary with the surrounding unexposed swarm. Passive phases of select size and shape are made by adjusting the UV-light aperture. In this way, passive phases are created within the swarm without the use of chemicals or mechanical stimuli, as to minimally invade the unexposed, active region of the swarm.

To quantify the collective motion of the cells, I measure a cross-grained bacterial velocity field using particle image velocity. A sample velocity field displays long-range correlations, as shown in Fig. 4.1ci, and an array of clock-wise and counter-clockwise vortices and jets. The mean velocity speed increases with increasing distance to the colony edge, reaching a pseudo-steady dynamic state in the range of 50 to 500  $\mu\text{m}$  from the edge [20,22]. In this range, I measure mean speeds of 24-32  $\mu\text{m/s}$ .

After exposure, the active and passive phases interact through the boundary. Sample velocity fields in Fig. 4.1cii show that there is no motion in that octagon-shaped region of the swarm that has been exposed to UV light. The unexposed region of the swarm, in contrast, remains active with collective flows near and far from the exposure boundary.

Zooming in at the boundary (4.1d and c), sample snapshots of the velocity field and streamlines reveal the dynamic motion of individual vortices. Vortices at the surface (blue line) can detach and move away (green, orange), while vortices from the bulk collide and attach it (brown). Others appear to split and move along the interface (light blue and dark blue), while some simply fade away (purple). The boundary is relatively stagnant during its interaction with a single vortex.

Over time, passive bacteria at the interface are convected into the active phase, and the size

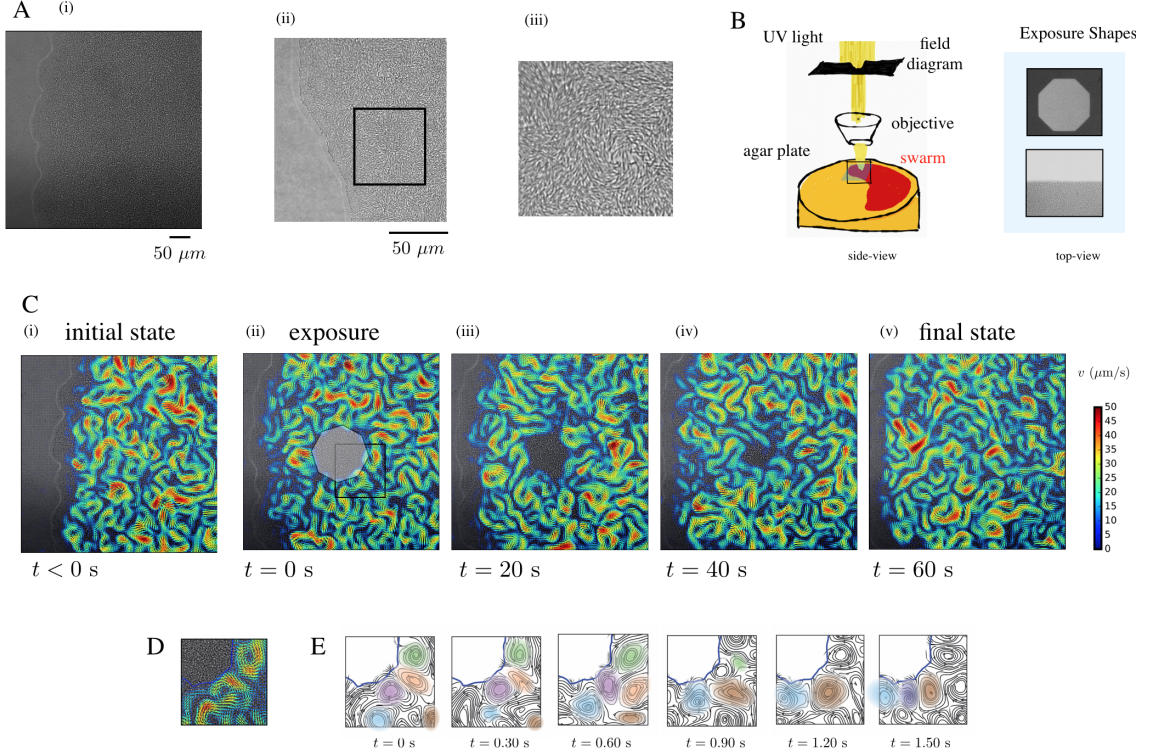


Figure 4.1: (A) The bacteria *Serratia marcescens* are grown on agar substrates, forming bacterial colonies that contain swarming cells at the expanding edge. (Aii) At this edge, cells are a monolayer thick, exhibit local body orientational order (Aiii). (B) Within this active swarming state, passive phases are created by exposing regions of the swarm to UV light (overlaid octagon), which damages cells motility and creates a region of immobile cells that behave as passive particles that is approximately  $120\ \mu\text{m}$  in size. (C) At the colony edge, cells exhibit collective motions, highlighted by the jets and swirls of the overlaid velocity fields that are measured from particle image velocimetry. After exposure, the active and passive phases interact through the induced phase boundary. As time passes, the size of the passive phase shrinks as immobile bacteria at the boundary are convected away. At approximately  $t = 60\ \text{s}$ , the passive phase vanishes and the swarm reaches an active phase that mirrors the initial state. Snapshots of the velocity field (D) and streamlines (E) at the interface reveal the dynamic motion of individual vortices. For instance, vortices in the bulk can collide and attach to the interface (brown), while vortices at the surface can detach and move away (green, orange). Others are seen to split and move along the interface (light and dark blue), while some simply fade away (purple).

of the passive region shrinks. At approximately 60 s, the initially 120  $\mu\text{m}$  sized passive phase has completely dissolved away and the swarm reaches an active state that mirrors its initial one.

My observations show that the UV-light exposure creates a quenched region of immobile bacteria within an active swarm of bacteria. Separating these two regions is a boundary. This boundary shares striking similarities with interfaces between two chemical species in passive thermodynamics. Although I have the same bacteria in each phase, they are different ‘chemical species’ in respect to their ability to self-propel. In this way, I have created an active-passive phase interface that samples a gradient in activity. Figure 4.1 showcases the transient relaxation of this active-passive phase-separated state into a homogenous mixture of active and passive bacteria. I use these experimental method as a platform to characterize the growth and form of active-passive interfaces.

## 4.3 Results and Discussion

### 4.3.1 Active-Passive Phase Order Parameter

In this section, I examine the structure and dynamics of the active-passive interface. To identify the interface, I define an order parameter  $\phi$  that distinguishes between the active and passive phases. In the active phase, bacteria self-propel, driving local fluctuations in bacterial concentration and corresponding fluctuations in the image pixel intensities  $|\Delta I|$ . In the passive phase, the bacteria do no move, and there are no fluctuations in concentration or image intensities. The intensity fluctuations  $|\Delta I|$ , which reflect fluctuations in bacterial concentration, therefore provide a robust means of distinguishing the active and passive phases.

I use a normalized measure of the intensity fluctuation  $|\Delta I|$  to define an order parameter field in space and time:

$$\phi(x, y, t) = \frac{2|\Delta I(x, y, t)| - |\Delta I_A| - |\Delta I_P|}{|\Delta I_A| - |\Delta I_P|} \quad (4.1)$$

Here,  $|\Delta I_A|$  and  $|\Delta I_P|$  are the mean intensity fluctuations in the active and passive phases far from the boundary. The order parameter  $\phi(x, y, t)$  varies from -1 to 1, with -1 corresponding to the passive phase and 1 corresponding to the active phase.

The phase boundary is defined over space for each time by the contour  $\phi(x, y, t) = 0$ . Figure 4.2a shows the position of the interface for the octagonal exposure in Fig. 4.1 at 10 second intervals.



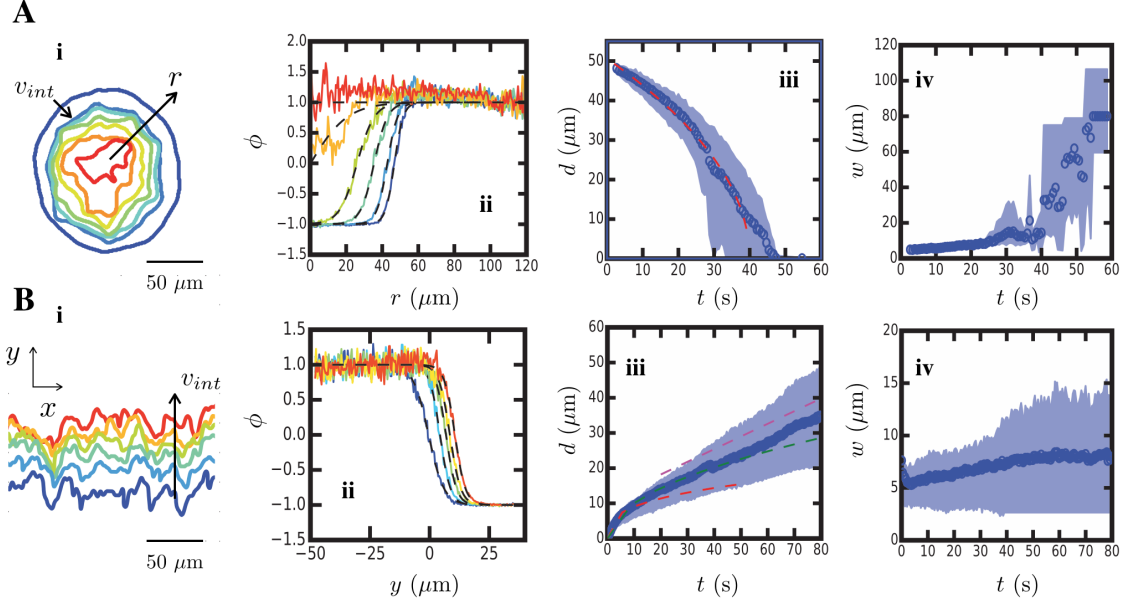


Figure 4.2: The active-passive phases evolve in space and time. (A and B) In the active phase, bacteria self-propel, driving local fluctuations in bacterial concentration and corresponding fluctuations in image pixel intensities  $|\Delta I|$ . I define an order parameter in Eq'n 4.1 based on  $|\Delta I|$ , so that  $\phi = 1$  and  $\phi = -1$  correspond to active and passive phases, respectively. The phase boundary is defined in space by the contour  $\phi(x, y, t) = 0$  and sample boundaries for the flat and octagonal exposures at 10 second intervals are shown in Ai and Bi. To obtain a corresponding phase profile for each time, the order parameter is averaged along  $x$  for the flat exposure and azimuthally for the octagonal exposure. (Aii and Bii) The phase profiles smoothly transition from 1 to -1 as it passes through the active-passive interface (profiles correspond to the same time as contours). The mean interface position  $d(t)$  and width  $w(t)$  are obtained by fitting the phase profiles to  $\phi(y, t) = \tanh[(y - d(t))/w(t)]$ . The mean, minimum, and maximum fitting parameters are gathered from four experiments and are shown over time (Aiii, Aiv, Biii, Biv). (Aiii and Aiv) The active phase dissolves the flat passive phase so that the mean interface position  $d$  increases in time, reaching a relatively constant velocity of approximately  $0.4 \mu\text{m/s}$  for  $t > 5$  s. For reference, the dynamic scalings  $t^{1/3}$ ,  $t^{1/2}$ , and  $t$  are shown as green, red, and pink lines, respectively. The boundary width  $w$  is roughly  $7 \mu\text{m}$  and constant in time. The active phase dissolves the octagonal-shaped passive phase so that the azimuthally averaged position of the interface decreases in time. The position scales as  $(t_0 - t)^{1/2}$ , where  $t_0$  is the time the passive region disappears. (F) For  $t < 40$  s, the mean boundary width  $w$  is between 5 and  $10 \mu\text{m}$ . At  $t \approx 40$  s, the size of the passive phase,  $2d \sim 20 \mu\text{m}$ , is approximately the width of the interface. For  $t > 40$  s, the width rapidly increases as the passive domain dissolves entirely.

Initially, the boundary positions reflect the shape of the octagonal exposure. Over time, the passive region shrinks and the shape of the boundary deforms. Some corners smooth away while others persist. At approximately 40 seconds, when the passive region is roughly 40  $\mu\text{m}$  wide, the passive region dissolves more rapidly and irregularly until it completely fades away.

Figure 4.2b shows the evolution of a flat interface that was created using an exposure with a long straight edge. The boundaries are also shown at 10 second intervals. In this case, I find also find that the interface propagates (up) as the passive phase dissolves into the active phase. Although the UV exposure has a flat edge, the active-passive phase boundary is not. Instead, the phase boundary is rough. This roughness appears to be set by the vortical flows of bacteria, which appear to etch and smooth the interface boundary. I examine this flow-interface interaction in more detail in the following sections.

Along the phase boundary contour, the active-passive interface is not infinitely shape but is instead fuzzy, possessing an intrinsic width  $w$ . Intrinsic widths are a feature of all passive phase boundaries. To examine the interface's intrinsic width, I calculate spatially-averaged phase profiles over time for the flat and octagonal exposures.

For the octagonal interface (Fig. 4.2a<sub>ii</sub>), the phase profile  $\phi(r, t)$  is obtained by averaging the order parameter  $\phi$  along  $\theta$  at each distance  $r$ . Initially, the approximate radius of the of the passive region is approximately 50  $\mu\text{m}$ , so that  $\phi = -1$  for  $r \ll 50 \mu\text{m}$  and  $\phi = 1$  for  $r \gg 50 \mu\text{m}$ . The active-passive interface moves as the passive region dissolves away. For  $t > 40$  seconds,  $\phi > -1$ , which signals the disappearance of the passive phase. At  $t = 50$  seconds, the entire field is active ( $\phi \approx 1$ ).

For the flat interface, the phase profile  $\phi(y, t)$  is obtained by averaging the order parameter  $\phi$  along  $x$  for each distance  $y$ . Sample phase profiles are shown in Fig. 4.2b<sub>ii</sub> at 10 second time intervals. Here,  $y = 0 \mu\text{m}$  corresponds to the initial position of the interface. At  $t = 0$  s, the phase profile  $\phi$  is relatively constant at  $\phi = 1$  for  $y \ll 0 \mu\text{m}$ , which corresponds to the active phase. For  $y \gg 0 \mu\text{m}$ ,  $\phi = -1$ , which corresponds to the passive phase. The active-passive interface corresponds to the range  $-10 < y < 10 \mu\text{m}$  in which  $\phi$  smoothly transitions from 1 to -1. The position of the interface moves as time passes.

The mean interface positions  $d(t)$  and widths  $w(t)$  are obtained as a function of time  $t$  by fitting

the phase profiles to

$$\phi(y, t) = \tanh[(y-d(t))/w(t)]. \quad (4.2)$$

This model captures the phase profile data, which supports the existence of an active/passive phase interface in my experiments.

Figures 4.2a<sub>iii</sub> and iv and 4.2b<sub>iii</sub> and iv plot the mean interface position and width over time for the octagon and flat cases. These figures include the mean, minimum, and maximum values gathered over four experiments.

For the octagonal exposure, the active phase dissolves the passive phase so that the azimuthally-averaged position  $d$  of the interface decreases in time. The position  $d$  scales as  $(t_0 - t)^{1/2}$ , where  $t_0$  is the time the passive region disappears. For  $t < 40$  s, the mean boundary width  $w$  varies between 5 and 10  $\mu\text{m}$ . At  $t \approx 40$  s, the width is approximately 20  $\mu\text{m}$ , which corresponds to the approximate size of the passive phase  $2d$ . For  $t > 40$  s, the width rapidly increases as the passive domain dissolves entirely.

For the flat interface, the mean interface position  $d$  increases with time  $t$ . After an initial transient, the interface position  $d$  increases linearly in time at a constant velocity of 0.4  $\mu\text{m/s}$  for  $t > 5$  s. For reference,  $d \sim t^n$  scalings are shown for  $n = 1/3$ ,  $1/2$  and  $1$  by the green, red, and pink lines in Fig. 4.2a<sub>iii</sub>, respectively. The boundary width  $w$  is approximately constant at 7  $\mu\text{m}$  for  $0 < t < 80$  seconds.

Together, the dynamic scalings of the interface position and width are fingerprints of the underlying physical mechanism that govern the growth and form of the interface. For a propagating interface in passive materials, if the order parameter is conserved, the velocity of the interface  $v_{\text{int}}$  is set by transport of the order parameter through the interface driven by the gradient in chemical potential  $\mu$ , such that  $v_{\text{int}} \propto J_{\text{in}} - J_{\text{out}} \propto [\partial\mu]_{\text{out}}^{\text{in}}$ , where  $J_{\text{in}}$  and  $J_{\text{out}}$  are the flux of the order parameter in and out of the boundary [33]. For passive interfaces, the chemical potential  $\mu$  is proportional to the interface curvature  $\mathcal{C}$ . For example, for a condensed phase surrounded by its vapor, regions of convex curvature have relatively higher  $\mu$  compared to a flat regions, whereas, regions of concave curvature have relatively smaller  $\mu$  [34]. This condition is the Gibbs-Thomson boundary condition. These conditions are the basis of the Cahn-Hilliard model and lead to an interface position  $L$  that scales as  $L \sim t^{1/3}$ . If transport of the order parameter is coupled to fluid flow, the interface position

scales as  $L \sim t$  [33].

I find that the mean position of the flat active-passive interface scales linearly in time and has a constant interface width. This implies that the active interface dynamics are not diffusive. Instead, these results suggest that transport of the passive bacteria is driven by an active chemical potential and coupled to the fluid flow. Furthermore, the observation that the interface width is constant also implies that the surface is in a pseudo-steady state with a corresponding surface tension. In passive fluids, the energy is supplied by thermal fluctuations. In my system, in addition to thermal energy, there is an energy supply from the active swarming bacteria. Because the interface width  $w$  is constant, there must be a pseudo-steady constant supply of energy that maintains the interface deformation. To examine the energy at the interface, estimate an active surface tension, and understand the interface's growth and form, I next consider the bacterial flow at the interface and how it varies from the bulk active state.

### 4.3.2 Boundary-Flow interaction

In this section I consider the interaction between the interface and the collective flow of bacteria. To investigate how the interface affects the collective flow, I begin by examining the bacterial velocity fields for varying distances from the active-passive interface. A sample vorticity field in Fig. 4.3a highlights the variation in collective flow across the flat interface (blue line). The bulk active phase contains collective flow and vortical structures that are entirely absent in the passive phase. At the interface between the two phases, a number of clockwise and counterclockwise vortices pattern the surface. There is clearly a gradient in velocity and vorticity across the interface and the interface does not appear to disturb the flow for distances beyond a vortex size ( $L \sim 20 \mu\text{m}$ ).

To examine these gradients more closely, for varying distances from the interface, I plot the instantaneous profiles of the vorticity  $\omega$ , velocity magnitude  $|v|$ , and the cosine of the velocity orientation  $\cos\theta$  as a function of  $x$ . Since the interface position is changing in time, I identify the distance from the interface in a moving frame  $Y(t) = d(t) - y$ , where  $d(t)$  is the mean position of the interface (Fig. 4.2). At the interface ( $Y = 0 \mu\text{m}$ ), the vorticity magnitude is nearly zero, as shown in Fig. 4.3bi. Further into the bulk at  $Y = 20 \mu\text{m}$ , the vorticity profile fluctuates from negative to positive along  $x$  with magnitudes up to 10 1/s. The velocity profile (Fig. 4.3bii) is also near zero at the interface and increases as  $Y$  increases. The velocity orientations (Fig. 4.3biii) samples

all direction, ranging from  $\pi < \theta < -\pi$ . The instantaneous peaks and valleys in  $\omega$ ,  $|v|$ , and  $\cos(\theta)$  reflect the corresponding clockwise and counter-clockwise vortical structures of the flow.

To examine the flow's time-averaged structure, I calculate the velocity autocorrelation in space for various  $Y$ . Here, I define the normalized spatial correlation of the velocity director  $\mathbf{v} = v/|v|$  as  $C_v(\Delta x) = \langle \mathbf{v}(\Delta x) \cdot \mathbf{v}(x_0 + \Delta x) \rangle / \langle \mathbf{v}(\Delta x)^2 \rangle$ , where the brackets denote an average over time and reference location  $\Delta x_0$ .

As shown in Fig. 4.3c, near the interface ( $Y = 30 \mu\text{m}$ ), the correlation exhibits oscillations, with six peaks in the span of  $150 \mu\text{m}$ . These oscillations are consistent with a pair-wise ordering of vortices approximately  $20 \mu\text{m}$  in size. In the bulk ( $Y > 30 \mu\text{m}$ ), the correlation magnitudes are smaller compared to the interface, suggesting a reduction in the vortex order. The correlations do not appear to oscillate at a single wavelength.

To compare the flow's structure with the interface structure, I measure the static structure factor of the interface. Here, I define the static structure factor over time as  $|\Delta h_q(t)|^2$ , where  $\Delta h_q(t)$  are the Fourier modes of the height fluctuations  $\Delta h(t, x)$ . The height fluctuations are defined in space and time as  $\Delta h(t, x) = h(t, x) - d(t)$ , where  $h(t, x)$  is the height profile along  $x$  (Fig. 4.2) and  $d(t)$  is the mean interface position so that the Fourier modes of the height fluctuations are

$$\Delta h_q(t) = \frac{1}{L_x} \int_0^{L_x} \Delta h(x, t) e^{-iqx} dx. \quad (4.3)$$

Here,  $L_x$  is the length of the interface (approximately  $200 \mu\text{m}$ ) and  $q = n\pi x/L_x$  are the wave numbers. The smallest  $q$  is  $0.015 \mu\text{m}^{-1}$ , which corresponds to the system size. The largest  $q$  I consider is  $1.0 \mu\text{m}^{-1}$ , which corresponds to wavelengths of  $1 \mu\text{m}$ , approximately half the length of one cell. The interface profile  $h(t, x)$  can be reconstructed from the Fourier modes as  $h(t, x) = \sum_q h_q e^{iqx}$ .

The time-averaged structure factor  $\langle |\Delta h_q|^2 \rangle$  is measured for four experiments and the mean is shown in Fig. 4.4Ai. The static structure exhibits a peak at  $q = 0.15 \mu\text{m}^{-1}$ , which correspond to an approximate wavelength  $L = \pi/0.15 \mu\text{m} \approx 20 \mu\text{m}$ . This wavelength corresponds to the same one for the velocity autocorrelation of the flow (Fig. 4.3c), which suggests that the flow may be deforming the interface and imprinting its structure to the surface.

For the case of a passive fluid-fluid interface excited by thermal noise, equipartition commands

$$\langle \Delta h_q^2 \rangle = \frac{1}{\kappa A q^2} \quad (4.4)$$

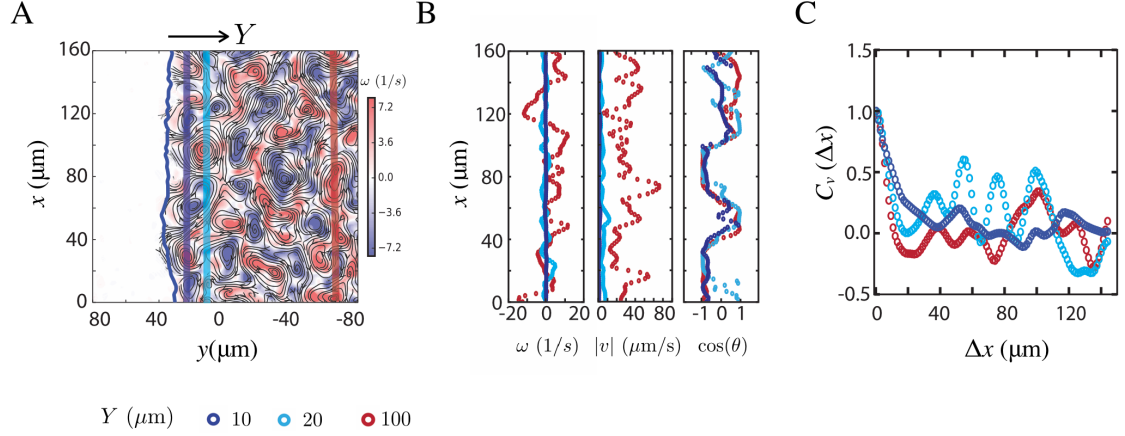


Figure 4.3: The interface and active/passive phases interact. (A) A sample vorticity field of the flat interface at  $t = 4$  s highlights the counter-clockwise and clockwise vortex structures that decorate the bulk active phase and the active-passive phase boundary (overlaid blue line). (B) Instantaneous profiles of the vorticity  $\omega$ , velocity magnitude  $|v|$ , and the cosine  $\theta$  of the velocity orientation as a function of  $x$  for various distances from the interface  $Y = d - y$ . The vorticity and velocity magnitudes are nearly zero at the interface ( $Y = 0$ ) and increase with increasing  $Y$ . The vorticity fluctuates from negative to positive along  $x$ , indicative of the counter-clockwise and clockwise vortex structures of the flow. The corresponding velocity magnitudes exhibits peaks between vortices and the cosine of velocity orientation varies from -1 to 1. (C) The normalized spatial correlation of the velocity director  $\mathbf{v} = v/|v|$  along  $x$ , averaged over time and reference locations  $x_0$ . Near the interface ( $Y = 30$   $\mu\text{m}$ ), the correlation exhibits strong oscillations, with an amplitude of 0.5 and a wavelength of approximately 20  $\mu\text{m}$ . The wavelength, 20  $\mu\text{m}$ , highlights the characteristic vortex size, and the amplitude indicates a significant ordering of vortices along the interface for distances up to 150  $\mu\text{m}$ . In the bulk ( $Y > 30$   $\mu\text{m}$ ), the correlation magnitudes are smaller compared to the interface, revealing a reduction in the vortex size. The correlations does not appear to oscillate at single wavelength.

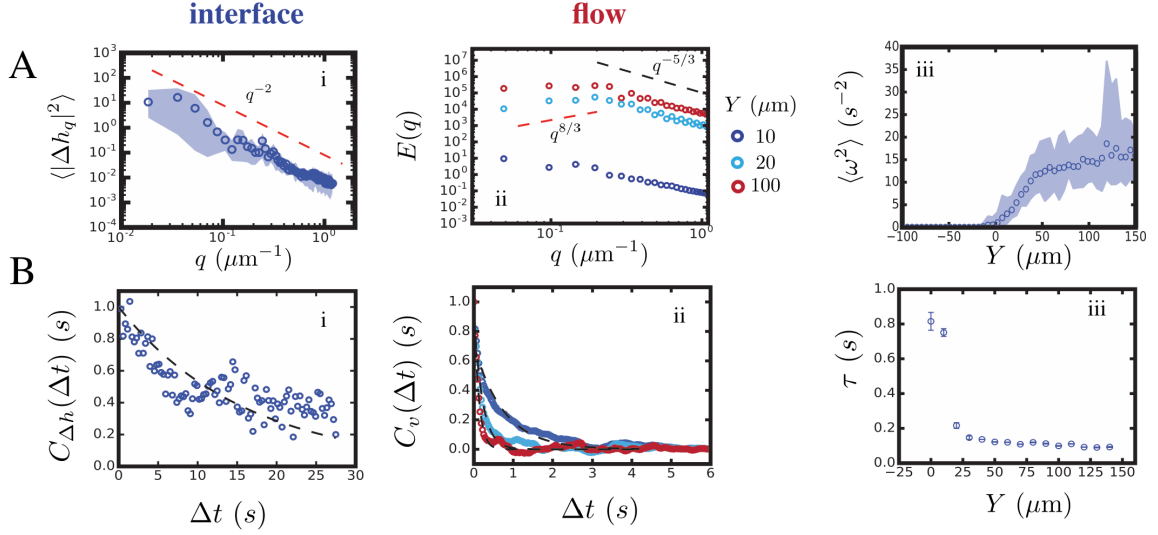


Figure 4.4: (A) Interface and flow structure. (Ai) To quantify the interface structure, I measure the structure factor  $|\Delta h_q(t)|^2$ , where  $\Delta h_q(t)$  is the Fourier modes of the height fluctuations  $\Delta h(t, x)$ . The static structure exhibits a peak at  $q = 0.15 \mu\text{m}^{-1}$ , which corresponds to length  $20 \mu\text{m}$ . The red line is the  $q^{-2}$  scaling. Fitting the data to Eq'n 4.4 yields a surface stiffness of  $5 \mu\text{m}^{-2}$ . The form of the energy spectrum varies with  $Y$ . (Aii) To quantify how the interface influences the flow structure, I measure the flow energy spectrum (Eq'n 4.5) for various  $Y$ . The magnitude of the energy spectrum increases with  $Y$ , since the vorticity magnitudes are higher in the bulk compared to the interface. This is shown in Diii, where the mean vorticity square  $\langle \omega^2 \rangle$  (averaged along  $x$ ) is plotted as a function of  $Y$ . The form of the energy spectrum varies with  $Y$  (Aii). At the interface ( $Y = 0 \mu\text{m}$ ), the energy spectrum, excepts a peak near  $q = 0.15 \mu\text{m}^{-1}$ , which corresponds to the peak in the static structure of the interface and the vortex size  $20 \mu\text{m}$ . Further from the interface at  $Y = 30 \mu\text{m}$ , the energy spectrum is more spread out for  $q < 0.2 \mu\text{m}^{-1}$ , revealing that characteristic vortex sizes do not have one dominant size but range over  $15 < L < 70 \mu\text{m}$ . The red and black lines are the scalings  $q^{5/3}$  and  $q^{-8/3}$ , respectively. (B) Interface and flow dynamics. The temporal evolution of the interface and flow. The height autocorrelation (Bi, Eq'n 4.6) decays in time more slowly than the velocity autocorrelations (Bii, Eq'n 4.7). By fitting the correlations to  $\exp(-\Delta t/\tau)$ , I obtain a characteristic decay time  $\tau$  of 16 s for the interface and 0.8 s for the flow near the interface ( $Y < 20 \mu\text{m}$ ). (Biii) The velocity correlation time scales decreases to 0.2 s for  $Y > 20 \mu\text{m}$ , suggesting that vortices near the boundary persist for longer times than in the bulk.

where  $\kappa$  is the surface stiffness and  $A$  is the interface's area. I find that in the active passive interface the static structure factor scales as  $\langle |\Delta h_q|^2 \rangle \sim q^{-2}$  (red line in Fig. 4.4Ai), which suggests there is a quasi-steady supply of energy deforming interface over a wide range of wavelengths.

To estimate an active surface stiffness, I fit the data to Eq'n 4.4. I use the interfacial area  $h \times L_X$ , with  $h = 1 \mu\text{m}$ , the width of a single cell since the swarm layer is approximately one cell layer thick. I find that  $\kappa$  is approximately  $4.5 \mu\text{m}^{-2}$ . This value is much smaller than the interfacial stiffness of water in air ( $1.7 \times 10^7 \mu\text{m}^{-2}$ ) but is similar to the stiffness phase-separated systems involving colloids, which range from 0.1 to  $20 \mu\text{m}^{-2}$  [35–39].

In a passive liquid-vapor interface, the surface tension is  $\gamma = \kappa k_B T$ , where  $k_B$  is the Boltzmann constant and  $T$  is the thermal temperature. In a passive fluid, thermal fluctuations drive interfaces with Gaussian white noise at an energy magnitude  $k_B T$ . In my active fluid, in addition to thermal energy, there is an energy supply from the active swarming bacteria. To examine the energy supply by the bacteria, I calculate the energy spectrum  $E(q)$  for various  $Y$ . The energy spectrum is calculated as the Fourier transform of the velocity autocorrelation in space

$$E(q) = \int_0^{L_x} (\Delta x) \cdot v(x_0 + \Delta x) e^{iqx} dx. \quad (4.5)$$

As shown in Fig. 4.4ii, the magnitude of the energy spectrum increases with  $Y$ : this is consistent with the increase in vorticity magnitudes with  $Y$  shown in Fig. 4.3bi. Figure 4.4iii explicitly shows the dependence of the mean vorticity square  $\langle \omega^2 \rangle$  (averaged along  $x$  and  $t$ ) as a function of  $Y$ . At the interface,  $\langle \omega^2 \rangle$  rapidly increases from 0  $1/\text{s}^2$  (in the passive phase) to 15  $1/\text{s}^2$  for  $Y > 50 \mu\text{m}$  (in the active phase), highlighting a gradient in vortical energy at the interface.

Not only the magnitude but also the form of the energy spectrum varies with  $Y$ . At the interface ( $Y = 10 \mu\text{m}$ ), the energy spectrum exhibits a peak near  $q = 0.15 \mu\text{m}^{-1}$ , which corresponds to the peak in the static structure of the interface and the vortex size  $20 \mu\text{m}$ . Further from the interface at  $Y = 30 \mu\text{m}$ , the energy spectrum is more spread out for  $q < 0.2 \mu\text{m}^{-1}$ , revealing that characteristic vortex sizes do not have one dominant size but ranges over  $15 < L < 70 \mu\text{m}$ .

The observed increase and decrease in the energy spectrum with is a unique characteristic of active fluids and is attributed to the injection of energy at the particle level [6]. In Fig. 4.4aii, I include two scalings that were observed in experiments of swimming *Bacillus subtilis* [6] in two-dimensional microfluidic devices for comparison: there scalings are  $E(q) \sim q^{5/3}$  for small  $q$  and



$E(q) \sim q^{-8/3}$  for large  $q$ . I note that for passive 2D Kolmogorov-Kraichnan turbulence,  $E(q) \sim q^{-5/3}$  [40].

My data suggests (Fig. 4.3c and 4.4aii) that the interface selects a dominant vortex size, 20  $\mu\text{m}$ , from the range of vortex sizes in the bulk. This vortex size corresponds to the characteristic wavelength of the interface structure (Fig. 4.4ai) and highlights a coupling between the interface and flow structure.

I next consider the temporal evolution of the interface and flow. For the active-passive interface, I measure the interface autocorrelation in time, defined here by

$$\langle C_{\Delta h}(\Delta t) \rangle = \frac{\langle \Delta h(t_0) \Delta h(t_0 + \Delta t) \rangle}{\langle |\Delta h(t_0)|^2 \rangle}, \quad (4.6)$$

where the correlation is averaged over reference locations and reference times  $t_0$ . The autocorrelation decays in time is shown in Fig. 4.4bi. I fit the data to  $\exp(-\Delta t/\tau)$  to obtain a characteristic decay time  $\tau$  of 16 s. For an over-damped passive fluid-fluid interface, as described by capillary wave theory [38], correlations in the interface structure decay at a single exponential rate  $\Gamma$ . A single exponential decay captures the main features of the data of an active-passive interface, consistent with dynamics in a phase-separated passive system.

For the flow, I measure the velocity director  $\mathbf{v}$  autocorrelation in time for various  $Y$ , defined here as

$$C_v(\Delta t) = \frac{\langle \mathbf{v}(t_0) \Delta \mathbf{v}(t_0 + \Delta t) \rangle}{\langle \mathbf{v}(t_0)^2 \rangle}, \quad (4.7)$$

As shown in Fig. 4.4bii,  $C_t(\Delta t)$  decays slowest near the interface  $Y < 20 \mu\text{m}$ . I fit the data to  $\exp(-\Delta t/\tau)$  at each  $Y$  to obtain a characteristic decay time  $\tau$  as a function  $Y$ . I find that  $\tau = 0.8$  s for the flow near the interface ( $Y < 20 \mu\text{m}$ ) and decreases to 0.2 s for  $Y > 20 \mu\text{m}$  (Fig. 4.4biii). This indicates that the velocity correlation and associated vortices persist for longer times than in the bulk and suggests that the interface stabilizes vortex structures.

The stabilization of vortical flows at phase boundaries has recently been observed in recent simulations [41] involving mixtures of active and passive sphere. In this case, the boundary induced vortical flows, which do not exist in the bulk and which drive particle flux through the boundary. My results uncover a new means in which phase interfaces can stabilize vortical flows: in active bacterial swarms with collective motion, the interface promotes a particular vortex size and increases vortex

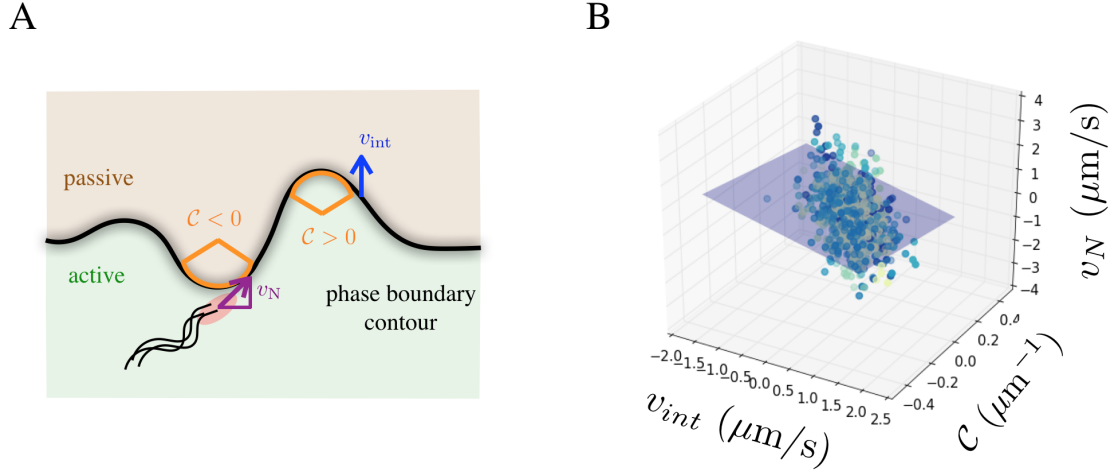


Figure 4.5: Phase interface velocity depends on interface curvature and bacterial flow. (A) A definition sketch denoting the direction of the interface curvature  $C$ , interface speed  $v_{int}$ , and tangential component of bacterial flow  $v_N$ . (B) A 3d scatter plot of local interface speed  $v_{int}$ , local interface curvature  $C$ , and bacterial flow  $v_N$  along the interface at 2 second intervals throughout the experiment. The collapse to a plane suggests an active analog of the Gibbs-Thomson boundary condition.

life span.

### 4.3.3 The growth and form of active interfaces: Connecting kinetics, thermodynamics, and mechanics

After examining the structure and dynamics of the active-passive interface and the collective motion at the boundary, I strive to understand what drives the local propagation of the interface, that is what sets the local interface velocity  $v_{int}$ .

In passive systems, the local interface velocity -through the Gibbs-Thomson boundary condition- is proportional to the interface curvature. In passive systems, the interface curvature is proportional to the gradient in chemical potential across the interface. I ask if there exists an active Gibbs-Thomson boundary condition analog in my active system, that is does the interface velocity depend upon the curvature of the interface?

My system has the unique feature that the interface structure is coupled to active flow and emergent vortices (Figs. 4.3, 4.4, and 4.5). In my system, however, it is unclear what plays the role of an active chemical potential or how the transport of passive particles out of the passive region is

coupled to flow/activity. To this end, I postulate the existence of a plane-

$$v_N = a + bv_{int} + c\mathcal{C} \quad (4.8)$$

such that the local interface velocity depends on the interface curvature  $\mathcal{C}$  and the tangential flow of bacteria  $v_N$ , as denoted in Fig. 4.5a.

To test this idea, I plot a three-dimensional scatter plot of the local interface speed  $v_{int}$ , local interface curvature  $\mathcal{C}$ , and normal component of bacterial flow  $v_N$  along the interface at various times throughout the experiment for the flat interface case. As shown in Fig. 4.5b, I find that the data collapses unto a plane, suggesting a correlation among the variables. The plane is a least squares fit defined by the slopes  $a = 0.2 \mu\text{m/s}$ ,  $b = -0.5$ , and  $c = -1.15 \mu\text{m}^2/\text{s}$  in equation 4.8.

I find that the interface velocity is negatively correlated with curvature. Regions of negative curvature move into passive phase relatively fastest, while regions of highest curvature tend to move the slowest (see Fig. 4.5a). In addition, the interface velocity is negatively correlated with the normal component of the flow. This suggests that for the interface to move into the passive phase there is a flow of bacteria across the interface and into the bulk active phase.

The data is scatted about the plane, however, for an active, noisy, far-from equilibrium the existence the data remarkably collapses about a plane, suggesting an underlying active Gibbs-Thomson boundary condition driving the interface growth and form.

## 4.4 Conclusions

Many motile bacteria swim in fluids and swarm at surfaces, injecting energy internally into their ambient environment. How this internally-injected energy deforms phase boundaries and, likewise, how the presence of boundaries influences the emergent collective motion of bacteria is largely unknown. To this end, I investigated the interface between an active phase of swarming bacteria and a passive phase of immobilized bacteria. I created this interface by locally immobilizing a portion of an active swarm with UV light. The interface is unstable: the swarming bacteria dissolve

the phase of passive bacteria and the system evolves from an active/passive phase-separated system into a homogenous mixture. I measure the position and width of the interface over time and the corresponding velocity fields of the bacteria. I find that the interface stabilizes the dynamic flow of the bacterial, generating larger and longer-lasting vortex structures compared to the bulk. The vortices, in return, etch the interface, molding the interface's structure and curvature. The local interface curvature correlations with the local interface velocity, suggesting an active analog of the Gibbs-Thomson boundary condition. My results have important implications for understanding transitions between equilibrium-like states in active materials and for understanding how bacteria shape boundaries, compete for new environments, and mix particulates, such as damaged/dead bacteria, extracellular polymers, vesicles, and other microbial species.

# Bibliography

- [1] Howard J. 2001. **Mechanics of motor proteins and the cytoskeleton.** *Sinauer Associates.*
- [2] Berg HC. 2003. **The rotary motor of bacterial flagella.** *Biochemistry* 72:19.
- [3] Vedula DRK, Ravasio A, Lim CT, Ladoux B. 2013. **Collective cell migration: a mechanistic perspective.** *Physiology* 28:370-379.
- [4] Ndlec F, Surrey T, Maggs, AC, Leibler S. 1997. **Self-organization of microtubules and motors.** *Nature* 389:305-308.
- [5] Schaller V, Weber C, Semmrich C, Frey E. 2010. **Polar patterns of driven filaments.** *Nature* 467:73-77.
- [6] Wensink HH, *et al.*. 2012. **Meso-scale turbulence in living fluids.** *Proceedings of the National Academy of Sciences* 109:14308-14313.
- [7] Sanchez T, Chen DT, DeCamp SJ, Heymann M, Dogic Z. 2012. **Sponantaneous motion in hierarchically assembled active matter.** *Nature* 491:431-434.
- [8] Brugues, J, Nuzzo V, Mazur E, Needleman DJ. 2012. **Nucleation and transport organize microtubules in metaphase spindles.** *Cell* 149:554-564.
- [9] Lee CF Brangwynne CP, Gharakhani J, Hyman AA, Julicher F. 2013. **Spatial organization of the cell cytoplasm by position-dependent phase separation.** *Physical Review Letters* 111:088101.
- [10] Schwarz-Linek J, *et al.*. 2012. **Phase separation and rotor sel-assembly in active particle suspensions.** *Proceedings of the National Academy of Sciences* 109:4052-4057.

- [11] Palacci J, Sacanna S, Steinberg AP, Pine DJ, Chaikin PM. 2013. **Living crystals of light-activated colloidal surfers.** *Science* 339:936-940.
- [12] Thompson A, Tailleur J, Cates M, Blythe R. 2011. **Lattice models of nonequilibrium bacterial dynamics.** *Journal of Statistical Mechanics: Theory and Experiment* P02029.
- [13] Redner G, Hagan MF, Baskaran A. 2013. **Structure and dynamics of a phase-separating active colloidal fluid.** *Physical Review Letters* 110:055701.
- [14] Yang X, Manning ML, Marchetti MC. 2013. **Aggregation and segregation of confined active particles.** *Soft Matter* 10:6477-6484.
- [15] Takatori SC, Yan W, Brady JF. 2014. **Swim pressure: stress generation in active matter.** *Physical Review Letters* 113:028103.
- [16] Kearns DB. 2010. **A field guide to bacterial swarming motility.** *Nature Reviews Microbiology* 8:634-644.
- [17] Harshey RM, Patridge JD. 2015. **Shelter in a Swarm.** *Journal of molecular biology* 427:3683-3694.
- [18] Harshey RM. 2003. **Bacterial motility on a surface: many ways to a common goal.** *Annual Reviews in Microbiology* 57:249-273.
- [19] Copeland MF, Weibel DB. 2009. **Bacterial swarming: a model system for studying dynamic self-assembly.** *Soft Matter* 5:1174-1187.
- [20] Darnton NC, Turner L, Rojevsky S, Berg HC. 2010. **Dynamics of bacterial swarms.** *Biophysical journal* 98:2082-2090.
- [21] Wu Y, Hosu BG, Berg HC. 2011. **Microbubbles reveal chiral fluid flows in bacterial swarms.** *Proceedings of the National Academy of Sciences* 108:4147-4151.
- [22] Steager EB, Kim CB, Kim MJ. 2011. **Dynamics of pattern formation in bacterial swarms.** *Physics of Fluids* 20:073601.
- [23] Alberti L, Harshey RM. 1990. **Differentiation of *Serratia marcescens* 274 into swimmer and swarmer cells.** *Journal of bacteriology* 172:4322-4328.

- [24] Zhang HP, Be'er A, Florin EL, Swinney HL. 2010. **Collective motion and density fluctuations in bacterial colonies.** *Proceedings of the National Academy of Sciences* 107:13626-13630.
- [25] Marchetti M, *et al.*. 2013. **Hydrodynamics of soft active matter.** *Reviews of Modern Physics* 85:1143.
- [26] Persat A, *et al.*. 2015. **The mechanical world of bacteria.** *Cell* 161:988-997.
- [27] Butler MT, Wang Q, Harshey RM. 2010. **Cell density and mobility protect swarming bacteria against antibiotics.** *Proceedings of the National Academy of Sciences* 107:3776-3781.
- [28] Roth D, *et al.*. 2013. **Cell density and mobility protect swarming bacteria against antibiotics.** *Proceedings of the National Academy of Sciences* 107:3776-3781.
- [29] Bensity S, Ben-Jacob E, Ariel G, Be'er A. 2015. **Antibiotic-induced anomalous statistics of collective bacterial swarming.** *Physical review letters* 114:018105.
- [30] Ingham CJ, Kalisman O, Finkelshtein A, Ben-Jacob E. 2011. **Mutually facilitated dispersal between the nonmotile fungus *Aspergillus fumigatus* and the swarming bacterium *Paenibacillus vortex*.** *Proceedings of the National Academy of Science* 108:19731-19736.
- [31] Finkelshtein A, Roth D, Jacob EB, Ingham CJ. 2015. **Bacterial swarms recruit cargo bacteria to pave the way in toxic environments.** *MBio* 6:e00074-00015.
- [32] Ben-Jacob E, Finkelshtein A, Ariel G, Ingham C. 2016. **Multispecies Swarms of Social Microorganisms as Moving Ecosystems.** *Trends in microbiology* 24:257-269.
- [33] Bray A. 2003. **Coarsening dynamics of phase-separating systems.** *Philosophical Transactions of the Royal Society of London A: Mathematical, Physical and Engineering Sciences* 361:781-792.
- [34] McLean JP, *et al.*. 1997. **Decay of isolated surface features driven by the Gibbs-Thomson effect in an analytic model and a simulation.** *Physical Review B* 55:1811.
- [35] Hernandez-Guzman J, Weeks ER. 2009. **The equilibrium intrinsic crystal-liquid interface of colloids.** *Proceedings of the National Academy of Sciences* 106:15198-15202.

- [36] Gasser U, Weeks ER, Schofield A, Pusey P, Weitz D. 2001. **Real-space imaging of nucleation and growth in colloidal crystallization.** *Science* 292:258-262.
- [37] Barry E, Dogic Z. 2010. **Entropy driven self-assembly of nonamphiphilic colloidal membranes.** *Proceedings of the National Academy of Sciences* 107:10348-10353.
- [38] Aarts DG, Schmidt M, Lekkerkerker HN. 2004. **Direct visual observation of thermal capillary waves.** *Science* 304:847-850.
- [39] Hennequin Y, *et al.* 2006. **Drop formation by thermal fluctuations at an ultralow surface tensions.** *Physical Review Letters* 97:244502.
- [40] Kraichnan RH, Montgomery D. 1980. **Two-dimensional turbulence.** *Reports on Progress in Physics* 43:547.
- [41] Wysocki A, Winkler RG, Gompper G. 2016. **Traveling fronts in active-passive particle mixtures.** *arXiv:1601.00850*.



# Chapter 5

## Summary & Perspectives

### 5.1 Summary

Understanding how the micro- and meso-scale swimmer-fluid interactions affect the bulk material behavior provides a stage for controlling active bio- and geophysical environments as well as engineering new, active materials. The aim of this work is to contribute to two outstanding questions in the field of active fluids: (i) how the two-way coupling between swimmer and fluid at micro-scales affects the dynamics and properties at macro-scales and (ii) to what extent passive mechanics and thermodynamics techniques can be applied to active systems? To this end, I have explored the dynamics of particles, polymers, and phases in experiments with model active fluids of bacterial suspensions and have uncovered many new and fascinating features of active materials, as summarized in the following.

*Chapter 2 - Particle dynamics in active fluids: The role of particle size on particle diffusion in aqueous *E. coli* suspensions.* I investigated the dynamics of swimming *E. coli* suspended in Newtonian fluids by using tracer particles of varying size. For dilute suspensions of bacteria in Newtonian fluids, I found that larger particles can diffuse faster than smaller particles - a feature absent in passive fluids. This anomalous particle-size dependence is due to an interplay between the active dynamics of the *E. coli* and the passive Brownian motion of the particle and has broad implications for particle transport in active fluids ranging from geophysical to biophysical

settings.

***Chapter 3 - Polymer dynamics in active fluids: how swimming *E. coli* and polymer molecules interact.*** I probed *E. coli* swimming dynamics in non-Newtonian fluids, namely, polymeric solutions. I found that even small amounts of polymer in solution can drastically change *E. coli* dynamics: cells tumble less and their velocity increases, leading to an enhancement in cell translational diffusion and a sharp decline in rotational diffusion. I showed that tumbling suppression is due to fluid viscosity while the enhancement in swimming speed is mainly due to fluid elasticity. Visualization of single fluorescently-labeled DNA polymers reveals that the flow generated by individual *E. coli* is sufficiently strong to stretch polymer molecules and induce elastic stresses in the fluid, which in turn can act on the cell in such a way to enhance its transport. These results show that the transport and spread of chemotactic cells can be independently modified and controlled by the fluid material properties.

***Chapter 4 - Phase dynamics in active fluids: The growth and form of active-passive phase boundaries in dense swarms of bacteria.*** I tested the use of constitutive equations and thermodynamic equations of state to active fluids, by examining the structure and dynamics of an active-passive phase separated system. I created this interface in a bacterial swarm, by transforming regions of the swarm into passive phases by exposing them to UV light, which locally immobilizes the bacteria. I find that the interface stabilizes the collective motion of the bacteria, generating larger and longer-lasting vortex structures compared to the bulk. The vortices, in return, etch the interface, generating interface curvature and setting the interface's structure. The local interface curvature correlates with the local interface velocity, suggesting an active analog of the Gibbs-Thomson boundary condition.

These results identify new avenues of transport, which include an anomalous particle-size dependence on particle diffusion in active fluids, an enhancement in bacterial diffusion in polymeric solutions, and the dissolution of passive materials by active swarms. In addition, the results have implications for the bulk rheology of active materials, how material properties are defined and measured in active fluids, and the thermodynamics and kinetics of active materials.

## 5.2 Future Recommendations

This work has uncovered a number of dynamical regimes in active fluids at scales ranging from polymers ( $< 1\mu\text{m}$ ), particles ( $1\text{-}10\ \mu\text{m}$ ), and phase-separated mixtures ( $> 100\ \mu\text{m}$ ). These unconventional dynamics have broad implications for particle transport in active fluids and suggest means to control the material properties of active soft environments. In the following, I highlight these implications and provide my recommendations for extending this work.

### *Diffusion to Sedimentation: Role of hydrodynamic interactions*

By investigating the diffusion of passive particles in active fluids, I found that particle diffusivity - unexpectedly - is non-monotonic in particle size [1]. This unexpected dependence highlights the interplay between passive and active components in a living fluid and their mediation through hydrodynamic interactions. In passive fluids, the role of hydrodynamic interactions on particle transport, which may be negligible at dilute concentrations, becomes increasingly more important as particles interact at higher concentrations. Understanding the role of hydrodynamic interactions on particle transport has been a long-standing challenge in passive fluids. In passive fluids, hydrodynamic interactions suppress particle diffusivity [4, 5]. Hydrodynamic interactions also play a role in the sedimentation of a dilute colloidal suspension: a single particle sediments at a velocity that is proportional to its size; while at higher particle concentrations, hydrodynamic interactions cause the mean particle sedimentation velocity to decrease [2] and can drive large density fluctuations. This phenomena has been the focus of intense research and debate [3, 6, 7] but is understood to be due to long-range hydrodynamic interactions [2] combined with a Debye-like screening of particle's velocity disturbances [8]. Given the importance of particle diffusion and sedimentation in our understanding of passive fluids, an exciting new focus of research would be particle sedimentation in active fluids. Because particle diffusivity is non-monotonic in size in active fluids, it opens up the possibility that particle sedimentation velocities may also have a non-monotonic dependence: can smaller particles sediment faster than larger particles? As in passive fluids, it would be interesting to investigate the hydrodynamic interactions between passive particles sedimenting in active fluids: do bacteria enhance or hinder particle interactions? These questions may have important implications for the sedimentation and transport of sediment and toxins in microbe-filled lakes and oceans [9].

### *Rheology of active polymeric fluids*

My investigation [10] of *E. coli* swimming dynamics in polymer solutions highlights a fascinating coupling between microbe motility and fluid rheology. I found that bacteria can stretch individual polymer molecules, increasing their average end-to-end distance. This finding suggests that increased polymer stretching may lead to an additional elastic stress in active polymeric fluids. An important next step is to understand how this bacteria-mediated stretching influences the time-dependent rheology of the fluid: do bacteria enhance or hinder the relaxation of individual polymers and how does this bacteria-polymer interaction influence the relaxation time of the bulk fluid? Microfluidic-based rheology methods are an appealing experimental design to investigate the rheology of active polymeric fluids. Microfluidic techniques allow for the simultaneous visualization of the microstructure and measurement of steady [11] and time-dependent [3] bulk material properties. By measuring polymer configurations through fluorescently-stained polymers [13, 14] or tethered polymer experiments [15], the end-to-end statistics of polymers can be measured under the influence of swimming bacteria and under applied flow. Furthermore, the polymers influence the dynamic of the swimming *E. coli* (speed, diffusivity) [10], which could simultaneously be measured in a microfluidic device. How this two-way coupling influences the bulk rheology is new ground for exploration. An important application may be in understanding the formation of biofilms [16], in which bacterial colonies excrete and assemble polymer molecules into protective shelters that are both soft and active.

### *Swarms: Particle transport and fluid rheology*

The interesting particle and polymer dynamics observed in dilute bacterial suspensions [1] naturally lends weight to the case of dense suspensions. In dense suspensions, bacteria exhibit collective motions with emergent vortical flows. This introduces a new length scale - or spectrum of length scales - that particles in dense suspensions would sample. It would be interesting to investigate how the non-monotonic particle size dependence in dilute suspensions is influenced by collective flows at higher bacterial concentrations. This has biological implications including how bacteria communicate: bacteria package of chemical-signal into micron-sized vesicles [17], which are observed throughout biofilms [18]. It would be interesting to explore the connection between vesicle size, collective motion, and the biochemical adaptability of bacteria.

Lastly, the role of extracellular polymers in the collective dynamics of bacteria is an ample area of research. I have found that polymer molecules enhance the speed and diffusivity of non-interacting swimming bacteria [10]. It would be interesting to explore the role of polymer molecules in the collective motions of bacteria and how elastic stresses may enhance or hinder their collective transport. Recent observations have shown that extracellular polymers are important in aligning and directing flows of bacteria on surfaces [19]. Thus, an exciting avenue of research would be to investigate the bio-mechanical coupling between bacteria polymer excretion and swimming dynamics which may allow bacteria to collectively invade and gain new territories on surfaces and in fluid.

## 5.3 Perspectives

Centuries ago, Antony van Leeuwenhoek reported that - in a drop of pond water beneath his microscope - danced a vast array of ‘wee animacles’ and ‘cavorting beasts’ [20]. These ‘wee animacles’ included single cells, whose existence uncovered the building block of life and forged our understanding of modern biology. Their ‘cavortings’ – that is self-propulsion – distinguished these single- and multi-celled organisms from their colloidal counterparts, passive particles enslaved to their fluctuating Brownian environments. The drop of pond water, itself, remained a largely unexamined, seemingly simple, dull and common fluid.

This work [1, 10] – in conjunction with investigations over the last two decades – however reveal that drops of pond water or - more generally - suspensions of self-propelling particles, so called ‘living’ or ‘active’ fluids, behave like no other fluids we know [21]. For instance, in a suspension of passive, colloidal spheres, an increase in particle diameter decreases the particle diffusivity. In a suspension of active, motile bacteria, an increase in particle diameter can *enhance* their diffusivity [1], a phenomena not seen in passive fluids. Clearly, the presence of life creates unusual and unexpected material properties. A living fluid, it seems, is as unique and distinct from a passive fluid as a living microbe is from a passive colloid.

While deciphering the underlying physical mechanisms that govern the dynamics and mechanics of active fluids may seem as daunting as characterizing the diversity of microbes within them, powerful techniques developed in passive mechanics and thermodynamics have been immensely successful in understanding the mechanical properties of materials that also contain a terrifically diverse set

of complex passive building blocks or microstructures [22, 23]. Classically, as in the case of passive albeit complex fluids, the bulk response at large hydrodynamic scales is described through the use of constitutive equations describing the features of the fluid, such as the stress and pressure, in terms of variables such as the deformation and deformation rate. These constitutive equations are related to the microstructure of the complex fluid using concepts from statistical physics and kinetic theory. For example, the bulk polymeric stress in a flowing polymer suspension can be related to the ensemble averaged mean stretch of the polymers provided polymer-polymer and polymer-solvent interactions are known. The success of these techniques in passive complex fluids raises an important question: to what extent can passive mechanics and thermodynamics techniques be applied to active systems?

In this regard, I have found that the flow generated by *E. coli* is sufficiently strong to stretch polymer molecules [10] – imparting an active component to the polymer end-to-end distance and elastic stress. In addition, by examining an active-passive phase separated system in a bacterial swarm, I have uncovered an equilibrium-like transient relaxation in active swarms (Chapter 4). The phase boundary velocity depends on the interface curvature and the flow of the active bacteria in such a way to suggest an active analog of the Gibbs-Thomson boundary condition.

“Living matter, while not eluding the “laws of physics” as established up to date, is likely to involve “other laws of physics” hitherto unknown, which however, once they have been revealed, will form just as integral a part of science as the former,” wrote Erwin Schrödinger [24] in 1944. It is in this sentiment that while we search for tools in conventional passive materials to understand active ones, we should be excited to uncover entirely new physical mechanisms – not or not yet seen in passive fluids. In this way, we will obtain insight that will transform our understanding of matter – living and non-living – as a whole.

# Bibliography

- [1] Patteson AE, Gopinath A, Purohit PK, Arratia PE. 2016. **Particle diffusion in active fluids is non-monotonic in size.** *Soft Matter* 12:2365-2372.
- [2] Batchelor GK. 1972. **Sedimentation in a dilute dispersion of spheres.** *J. Fluid Mech.* 52:245-68.
- [3] Guazzelli E, Hinch J. 2010. **Fluctuations and instability in sedimentation.** *Annual review of fluid mechanics* 43:97-116.
- [4] Batchelor GK. 1976. **Brownian diffusion of particles with hydrodynamic interaction.** *J. Fluid Mech.* 74:1-29.
- [5] Qiu X, Wu XL, Xue, JZ, Pine DJ, Weitz DA, Chaikin PM. 1990. **Hydrodynamic Interactions in Concentrated Suspensions.** *Physical Review Letters* 65:4.
- [6] Davis RH. 1996. **Hydrodynamic diffusion of suspended particles: a symposium.** *J. Fluid Mech.* 310:325-335.
- [7] Piazza R. 2014. **Settled and unsettled issues in particle settling.** *Rep. Prog. Phys.* 77:056602.
- [8] Shaqfeh ESG, Koch DL. 1980. **Screening in sedimenting suspensions.** *J. Fluid Mech.* 224:275-303.
- [9] Stocker R, Seymour JR. 2012. **Ecology and Physics of Bacterial Chemotaxis in the Ocean.** *Microbiol. Mol. Biol. Rev.* 76:792.
- [10] Patteson AE, Gopinath A, Goulian M, Arratia PE. 2016. **Running and tumbling with *E. coli* in polymeric solutions.** *Scientific Reports* 5:15761.

- [11] Nordstrom KN, Verneuil E, Arratia PE, Basu A, Zhang Z, Yodh AG, Gollub JP, Durian DJ. 2010. **Microfluidic Rheology of Soft Colloids above and below Jamming.** *Phys. Rev. Lett.* 105:175701.
- [12] Koser AE, Pan L, Keim NC, Arratia PE. 2013. **Measuring material relaxation and creep recovery in a microfluidic device.** *Lab Chip* 13:1850.
- [13] Liu Y, Steinberg V. 2010. **Molecular sensor of elastic stress in a random flow.** *Eur. Phys. Lett.* 90:44002.
- [14] Smith DE, Babcock HP, Chu S. 1999. **Single-polymer dynamics in steady shear flow.** *Science* 283:1724.
- [15] Doyle PS, Ladoux B, Viovy J-L. 2000. **Dynamics of a tethered polymer in shear flow.** *Phys. Rev. Lett.* 84:20.
- [16] O'Toole G, Kaplan HB, Kolter R. 2000. **Biofilm formation as microbial development.** *Annu. Rev. Microbiol.* 54:49-79.
- [17] Mashburn LM, Whiteley M. 2005. **Membrane vesicles traffic signals and facilitate group activities in a prokaryote.** *Nature* 437:03925.
- [18] Schooling SR, Beveridge TJ. 2006. **Membrane Vesicles: an Overlooked Component of the Matrices of Biofilms.** *J. Bacteriology* 188:5945-5957.
- [19] Gloag ES, Turnbull L, Huang A, *et al.* 2012. **Self-organization of bacterial biofilms is facilitated by extracellular DNA.** *PNAS* 110:11541-11546.
- [20] Dobell C. 1932. **Antony van Leeuwenhoek and his "little animals".** *London: John Bale, Sons & Danielsson.*
- [21] Patteson, AE, Gopinath A, Arratia PE. 2016. **Active colloids in complex fluids.** *Current Opinion in Colloidal & Interfacial Science* 21:86-96.
- [22] Brady JF, Bossis G. 1988. **Stokesian dynamics.** *Annual Rev. Fluid Mech.* 20:111-57.
- [23] Squires TM, Mason TG. 2009. **Fluid mechanics of microrheology.** *Annual Rev. Fluid Mech.* 42:413.
- [24] Schrödinger E. 1992. **What is life?** *Cambridge University Press.*



# Appendices

# Appendix A

## Supplementary Materials for particle dynamics in *E. coli* suspensions

### A.1 Role of confinement and interfacial effects

The thickness of the film,  $h_f$ , is about  $100 \pm 20$  microns with the particle (tracer) diameter  $d$  ranging from  $0.6 - 39 \mu\text{m}$ . Thus the ratio  $h_f/d \sim 150 - 3$ . Given that the ratio is large for all except the largest particle, I consider possible confinement effects for the largest 39 micron particles. An upper bound for the thermal diffusivity in the absence of bacteria can be obtained by assuming that the particle spans the film and diffuses in the plane of the film using the Saffman-Delbruck [1] estimate. According to this theory, the diffusivity of a sphere (diameter  $d \sim h_f$ ) completely confined in a free-standing film with viscosity  $\mu$  surrounded by air with viscosity  $\mu_a$

is given approximately by

$$D_0^f \approx \frac{k_B T_0}{3\pi\mu d} \left( \frac{3}{4} \left[ \ln\left(2\frac{\mu}{\mu_a}\right) - 0.5772 \right] \right).$$

Note that even the largest 39 micron particle is not as confined as the expression assumes since the particle does not span the film. Furthermore I note that the diffusivity  $D_0^f \sim d^{-1}$ , a functionality similar to the free thermal diffusivity  $D_0$ . Plugging in values for the viscosities of film,  $\mu$  and air  $\mu_a$ , I find  $D_0^f \approx 0.05 \mu\text{m}^2/\text{s}$  for the 39 micron particle. For the lowest bacterial concentration I used, the effective diffusivity of the tracer particle is approximately  $0.1 \mu\text{m}^2/\text{s}$ , still higher than  $D_0^f$ . At concentrations greater than  $1.5 \times 10^9$  cells/mL, the effective diffusivity is an order of magnitude higher and the particle diffusion is dominated by activity and not by confinement.

Particles are only tracked while in the plane of focus. For small particles ( $d < 3 \mu\text{m}$ ), the sedimentation velocities are low ( $< 0.3 \mu\text{m}/\text{s}$ ) and the particles do not sediment significantly over the time scale of the experiment. The sedimentation velocity of the  $39 \mu\text{m}$  polystyrene particle in water is  $\approx 50 \mu\text{m}/\text{s}$ . Before taking data, I allow the  $39 \mu\text{m}$  to settle near the bottom of the film. While the particle is close to the surface, there is still a film of liquid and hence the comments in the previous paragraph still apply - *i.e.*, the effective diffusion is still dominated by activity. Any draining of the fluid that results in the particle breaching the surface occurs over scales much larger than the experimental times.

Finally, I consider the possible deformation of the interface from the particle due to the weight of the particle by estimating maximum induced curvatures. The settling particle exerts a force  $F_g = \frac{1}{6}\pi g\mu\Delta\rho d^3$  on the interface. Here,  $\Delta\rho \approx 0.05 \times 10^3 \text{ kg}/\text{m}^3$  and  $g \approx 9.8 \text{ m}/\text{s}^2$ . This force acts on a surface with projected area of roughly  $A = \pi d^2/4$ . The pressure exerted,  $F_g/A$ , is less than the capillary pressure  $4\sigma/d$

suggesting that any surface deformation occurs with curvatures smaller than the particle curvature. Specifically for the 39 micron particle, the ratio  $(F_g d / 4\sigma A)$  is less than  $10^{-5}$ .

## A.2 Role of concentration on particle dynamics

### A.2.1 Collapse of particle distributions

To probe the effect of bacteria-particle interactions on long time particle displacements, I measure the van-Hove distribution - the probability distribution function (PDF) of particle displacements  $\Delta x$  - for varying concentrations of *E. coli* and different particle sizes. Shown in Fig. A.1(a) are the PDF's of 2  $\mu\text{m}$  particles measured over a fixed time interval  $\Delta t = 2$  s. The PDF curves are nearly Gaussian (dashed lines are fits) indicating diffusive behavior with widths that increase as the concentration increases. When  $c = 0$  cells/mL, the width of the distribution yields  $D_0 \approx 0.2 \mu\text{m}^2/\text{s}$ , consistent with the Stokes-Einstein prediction for a freely diffusing tracer. In the presence of bacteria, while still approximately Gaussian, the PDF's exhibit deviations at the tail end, particularly a relative enhancement compared to the Gaussian fit. The tail-end deviations from Gaussianity tend to decrease at the highest bacterial concentration,  $c = 7.5 \times 10^9$  cells/mL. These observations are consistent with previous experimental [2] and theoretical [3] studies of swimming microorganisms. These studies have shown that while the tail ends of particle displacement distribution function in the bulk [4] exhibit strong deviations from Gaussianity, the tail ends of the distribution function in a fluid film converge towards Gaussianity [2].

As shown in Fig. A.1(b), I can collapse the PDF curves of particle displacements over time in the presence of *E. coli* ( $c = 1.5 \times 10^9$  cells/mL), when the displacement

$\Delta x$  is rescaled by  $\Delta x / \langle \sqrt{\Delta x} \rangle^2$ .

The Gaussian nature of the particle distributions is further exemplified by the non-Gaussianity parameter NGP [5], which is defined as a function of time  $\tau$  as

$$\text{NGP}(\tau) = \frac{\langle \Delta x(\tau) \rangle^4}{3 \langle \Delta x(\tau)^2 \rangle^2} - 1,$$

where the brackets denote ensemble averages. For a Gaussian distribution, the NGP equals zero at all times, and thereby quantifies the deviation of a distribution from a Gaussian one over time. For the 2  $\mu\text{m}$  particle distributions shown Fig. A.2, I have calculated the NGP in the absence ( $c = 0$  cells/mL) and presence of bacteria ( $c = 0.75$  and  $1.5 \times 10^9$  cells/mL), as shown in Fig. A.1. As expected, in the absence of bacteria, when the system is in thermal equilibrium, the NGP is approximately zero ( $\sim 0.1$ ) at all times. For  $c > 0$  cells/mL, the NGP values are still close to zero, which indicates that the distributions behave in a Gaussian way.

### A.2.2 Effective diffusivity and cross-over time

I fit the MSD curves in Fig. 2.2(a) to the solution for generic Langevin dynamics - eqn (2.1) [6]. This allows us to estimate  $D_{\text{eff}}$  and  $\tau$ . When the tracer size is held constant, both  $D_{\text{eff}}$  (Fig. A.3(a)) and  $\tau$  (Fig. A.3(b)) increase with *E. coli* concentration.

For very dilute concentrations  $\phi \ll 1$ , tracer-bacteria interactions are mainly binary [7] and I expect the enhancement to the diffusivity to scale linearly with concentration. An alternate way to explain the linear dependence is to note that at low concentrations and in the absence of collective motion or anomalous density fluctuations, fluctuations in bacterial concentration scale by the central limit theorem as  $\sqrt{c}$ . The impulse due to these fluctuations sets the length scale characterizing

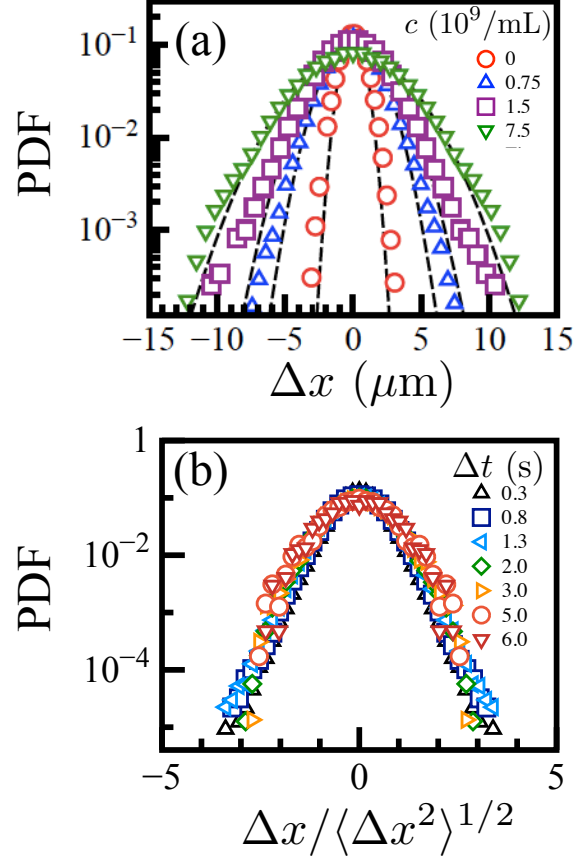


Figure A.1: (a) The probability distribution of  $2 \mu\text{m}$  particle displacements  $\text{PDF}(\Delta x, \Delta t, c)$  at  $\Delta t = 2$  s for varying bacterial concentrations  $c$ . Dashed lines are fits to a Gaussian. (b) The collapse of the probability distribution at different time steps in a bacterial suspension with concentration  $c = 7.5 \times 10^9$  cells/mL.

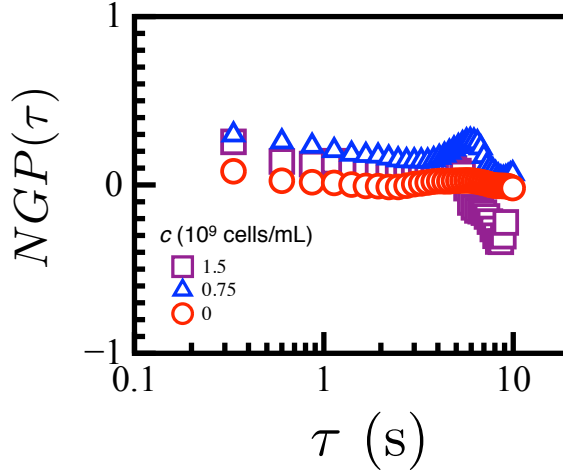


Figure A.2: The non-Gaussianity parameter of  $2 \mu\text{m}$  tracers particles over time  $\tau$  in the absence ( $c = 0$  cells/mL) and presence of *E. coli* ( $c = 0.75$  and  $3.0 \times 10^9$  cells/mL).

bacteria-tracer encounters; this length scale scales as  $\sqrt{c}$  and thus the diffusivity scales as the square of this length  $D_A \sim O(c)$ . Indeed, our estimated values of  $D_{\text{eff}}$  increases linearly with bacterial concentration  $c$ , as shown by the dashed-line in Fig. A.3(a). The variation of  $\tau$  with concentration, however, does not follow a linear form. Instead, Fig 3(b) suggests possible saturation of  $\tau$  for suspensions of higher concentrations (but still dilute).

### A.2.3 Comparison to previous experiments

The enhanced diffusion of passive particles in suspensions of swimming microorganisms has been previously verified in a variety of experimental techniques, including particle tracking methods in films [2], dye transport in microfluidic [8], and differential dynamic microscopy in three-dimensional chambers [9]. Previous investigators have proposed a linear relationship between the enhanced diffusivity and bacteria concentration to interpret their results [7, 9, 10] i.e.,  $D_{\text{eff}} = D_0 + \beta U c$  where  $D_0$  is the thermal diffusivity that follows the Stokes-Einstein relationship,  $U$  is the character-

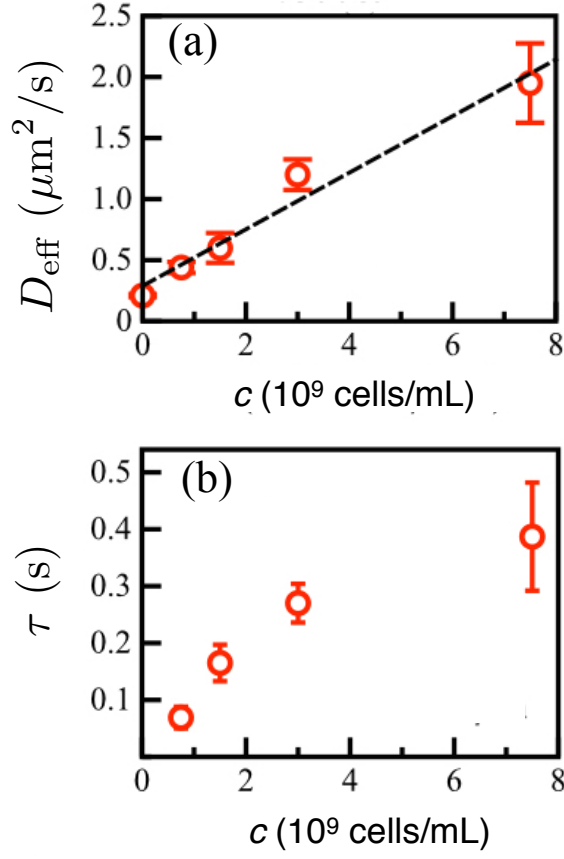


Figure A.3: (a) Effective diffusivities,  $D_{\text{eff}}$  for  $2 \mu\text{m}$  particles, as a function of bacteria concentration,  $c$ . The trend is roughly linear, with a fitted slope (dashed line) consistent with previous results. (b) The corresponding crossover time  $\tau$  increases monotonically with  $c$ .



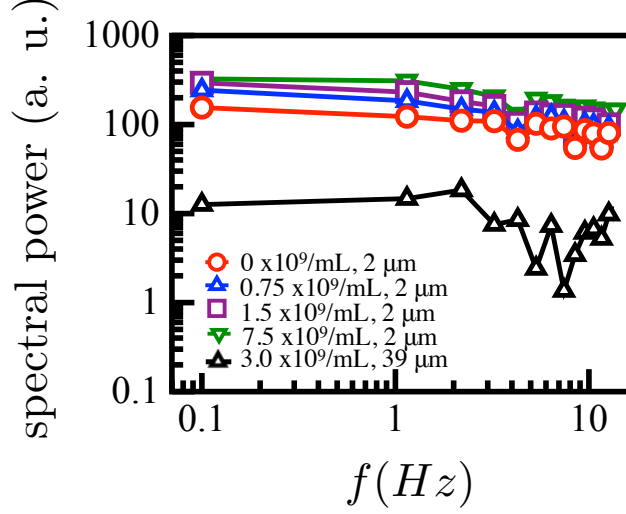


Figure A.4: Spectral density of particle speeds at varying *E. coli* concentrations of 0, 0.75, 1.5, and  $7.5 \times 10^9$  cells/mL and particle diameters of  $2 \mu\text{m}$  and  $39 \mu\text{m}$ .

istic swimming speed (self-propulsive speed) of the microorganism and the quantity  $Uc$  has been called the active flux  $J_A$  [9, 10]. By dimensional arguments, it is clear that  $\beta$  has units  $(\text{length})^4$ . Previous experimental investigations with *E. coli* have assumed  $\beta$  is constant and has a magnitude between 5 to  $13 \mu\text{m}^4$  [7–10]. A linear fit to Fig. A.3(a) yields  $\beta \approx 9 \mu\text{m}^4$  yields a reasonable fit consistent with the previous measurements mentioned above.

I also note discrepancies that support the contention that  $\beta$  is not really a constant, but varies with particle size. Following the theory by Kasyap *et al.* [7], I rewrite  $\beta = L^4 \bar{D}_A$ , where  $L$  is the total length of the bacteria ( $7.6 \mu\text{m}$  for cell body and flagella) and  $\bar{D}_A$  is a particle size-dependent dimensionless diffusivity which decays to zero at small particle diameter.

#### A.2.4 Spectral analysis

To quantify the velocity fluctuations, I measure the speed  $v$  of individual particles as a function of time, where the speed  $v = \Delta \mathbf{r} / \Delta t$  is set by the frame rate  $\Delta t = 1/30$  s. Next, a one-sided power spectra is then determined for each particle in a frequency range of 0.1 to 15 Hz, which corresponds to  $2\Delta t$  to 10 s. The power spectra are normalized by  $N/2$ , where  $N$  is the number of data points. To determine an ensemble average within an experimental sample, I average the power spectra over individual particles, which have the same frequency binning intervals. As shown in Fig. A.4, the power spectra are reasonably flat for varying *E. coli* concentrations and particle diameters. At equilibrium, the magnitude of the random thermal forcing, which appears as white noise, sets the temperature  $T$  [6], such that  $\lim_{t \rightarrow \infty} \overline{v(t)v(t)} = \frac{k_B T}{m}$ , where  $m$  is the mass of the particle. In the infinite time limit, the initial conditions are forgotten.

Here, I find that the experimentally measured magnitudes of the power spectra increases with *E. coli* concentration for  $d = 2 \mu\text{m}$ . As predicted by the infinite time limit, the increase in the magnitudes is consistent with an enhanced effective temperature (Fig. A.5(a)). For  $d = 39 \mu\text{m}$ , the power spectra magnitude is reduced. This is expected since the increase in the variance of the particle speeds - i.e, the enhancement in the temperature is insufficient to overcome the increased mass.

### A.3 MSD for a diffusing tracer

I consider a simple model of a spherical particle that undergoes an continuously diffusive process (due to both thermal and active effects) involving a sequence of small runs and random re-orientations. This is the case when the tracer is buffeted

around by interactions with bacteria. These assumptions are consistent with the sample trajectories shown in Fig. A.5.

Let the tracer be located at  $\mathbf{r}(t)$  at time  $t$  and oriented with an angle  $\theta(t)$ . For ease of analysis, I let the tracer move at a characteristic constant speed  $v$  between significant reorientations. The speed may be formally considered a function of the concentration of the bacteria and the tracer size. The position and orientation of the tracer follows  $d\mathbf{r}/dt = v\mathbf{t}(t)$  and  $d\theta/dt = \eta(t)$ . Here,  $\eta(t)$  is a zero-mean, delta-correlated Gaussian random variable such that  $\langle \eta(t)\eta(t') \rangle = 2D_R\delta(t - t')$  and  $\mathbf{t}$  is the instantaneous, local tangent to the trajectory. Note that here  $D_R$  is *not equal to*  $D_R^0$ , the rotational diffusivity in the absence of bacteria and purely due to Brownian effects. Application of the central limit theorem shows that  $\Delta\theta$  has zero mean and is distributed following a Gaussian profile. The pdf (probability density function),  $\psi$  is given by  $\psi(t, \Delta\theta) = (1/4\pi t D_R)^{1/2} \exp(-\frac{\Delta\theta^2}{4\pi t D_R})$  which may then be readily used to calculate averages. The mean square displacement (MSD) is obtained by evaluation of the following integral expression  $\langle |\mathbf{r}(t + \Delta t) - \mathbf{r}(t)|^2 \rangle = v^2 \int_t^{t+\Delta t} dt' \int_t^{t+\Delta t} dt'' \langle \cos[\theta(t') - \theta(t'')] \rangle$  and is found to be  $\text{MSD}(\Delta t) = 2(v^2/D_R) \left( t - \frac{1 - e^{-\Delta t D_R}}{D_R} \right)$ .

The effective translational diffusivity is obtained by now rewriting this expression. First, I introduce an average run time  $\tau \equiv D_R^{-1}$ , that characterizes the time for the MSD to transition from ballistic to diffusive behavior and is related to the time for the particle to forget its initial orientation. I then introduce an effective diffusivity  $D_{\text{eff}}$  that is the sum of its value at zero concentration and an excess concentration dependent *active* diffusivity  $D_{\text{eff}} = D_0 + D_A(c)$ . To leading order for small concentration  $D_A$  is linear in bacterial concentration  $c$  when no collective motion exists. Adjusted

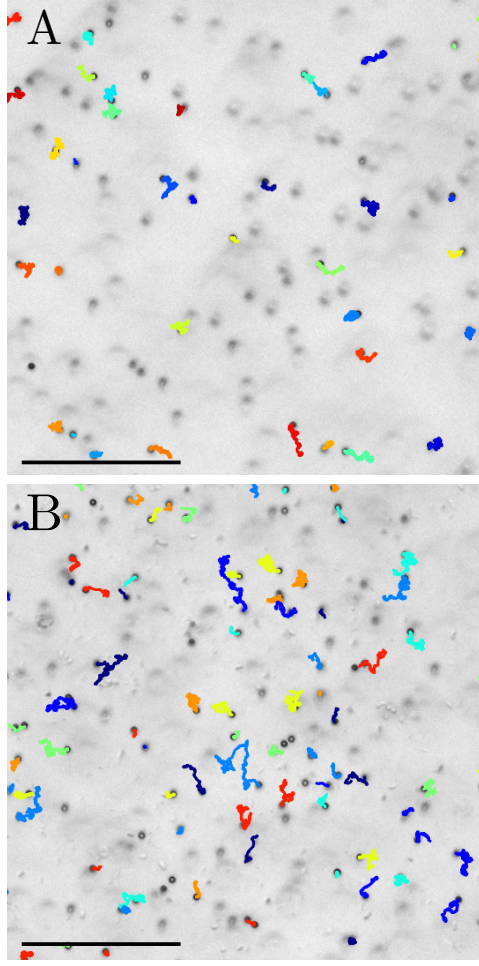


Figure A.5: Enhanced particle diffusion due to bacteria activity. Trajectories of  $2\text{ }\mu\text{m}$  particles in a film of fluid (a) without and (b) with bacteria ( $c = 0.75 \times 10^9\text{ cells/mL}$ ) reveal that particles in the presence of bacteria undergo larger magnitudes of displacement. Scale bars are  $50\text{ }\mu\text{m}$ .

for the two dimensional nature of the motion, the MSD then writes as

$$\text{MSD}(\Delta t) = 4(D_0 + D_A)\Delta t \left(1 - \frac{\tau}{\Delta t} \left(1 - e^{-\frac{\Delta t}{\tau}}\right)\right). \quad (\text{A.1})$$

Treating  $\tau$  as a function of concentration, I take the limit of  $c \rightarrow 0$  to obtain the formal solution in the limit of zero concentration

$$\text{MSD}(\Delta t)(c=0) = 4D_0\Delta t \left(1 - \frac{\tau_0}{\Delta t} (1 - e^{-\Delta t/\tau_0})\right)$$

where  $\tau_0 = \tau(c=0)$ . Eqn (A.1) is valid in both active and passive limits and has indeed be used to investigate diffusion of tracers in active fluids and biofilms [2, 11]. The long lag time limit taken when  $\Delta t/\tau \gg 1$ , gives us the asymptotic expression

$$\text{MSD}(\Delta t \gg \tau) \sim 4(D_0 + D_A)\Delta t - 4(D_0 + D_A)\tau$$

with corrections that are exponentially small. In the short lag time limit as  $\Delta t/\tau \ll 1$ , I find the asymptotic expansion  $\text{MSD}(\Delta t \ll \tau) \sim 2(D_{\text{eff}})(\Delta t)^2/\tau$ .

An alternate analytical expression for the MSD has been derived previously and used to interpret the diffusion of active photo-colloids [12–14]:

$$\text{MSD}(\Delta t) = 4(D_0 + D_A)\Delta t - 4D_A\tau(1 - e^{-\Delta t/\tau}). \quad (\text{A.2})$$

Comparison of eqn (A.2) with eqn (A.1) reveals the following features. First the long time effective diffusivities  $D_{\text{eff}}$  predicted by the two expressions in the limit  $\Delta t/\tau \rightarrow \infty$  are the same. Since  $D_A = D_{\text{eff}} - D_0$  and  $D_0$  is defined (and not a fitting parameter), the values of the active diffusivity obtained from both forms are the same. The short time asymptote of (A.1) and (A.2) for small lag time are however different. Equation (A.2) yields  $\text{MSD} \sim 4(D_0 + D_A)\Delta t - 4D_A\tau\Delta t/\tau \sim 4D_0\Delta t$  in contrast to the superdiffusive (ballistic to leading order) asymptotic form from (A.1). Furthermore in the limit of zero bacterial concentration when  $D_A = 0$ , eqn (A.2) does not reduce to the formal solution to the Langevin equation.

I have used both eqn (A.1) and (A.2) to fit my data. Since  $D_0$  is not a fitting parameter but is given by the analytical Stokes-Einstein relationship, I fit for  $D_A$

and  $\tau$ . I find that eqn (A.1) gives a better fit for  $\tau$  for the two smallest particle sizes at small times. For other cases, both equations yield comparable values of  $\tau$ . The values of  $D_A$  obtained from the long time asymptotes are the same for (A.1) and (A.2). Because of these considerations, I have chosen to use the MSD expression given by eqn (A.1) to analyze the data.

## A.4 Previous theory for small and large Peclet number

Kasyap, Koch and Wu [7] recently presented a analytical theory supplemented by simulations of the diffusion of passive, Brownian tracer particles in three dimensional suspensions of *E. coli* bacteria. They present an explicit expression for the hydrodynamic particle diffusivity  $\overline{D}_A$  resulting from bacteria-particle interactions. Their analytical theory assumes that encounters are binary, ignores steric interactions (which were however considered in more detailed simulations) and uses two additional simplifications - first that orientations of bacterium before and after a tumble are uncorrelated and second, that the fluid velocity disturbance created by each bacterium is small compared to its swimming speed,  $U$ .

Both the analytical theory and the simulations show that the scaled hydrodynamic diffusivity,  $\overline{D}_A = (D_{\text{eff}} - D_0)/cL^4U$  is controlled by the two dimensionless parameters - the Peclet number,  $\text{Pe} \equiv UL/D_0$  (the ratio of the time scale of bacterial swimming to the tracer diffusion time and  $\tau_* \equiv U\omega_T^{-1}/L$ , (the inverse of the tumble frequency  $\omega_T$  to the time a bacterium takes to swim a distance equal to its length  $L$ ). In all the experiments, I use the same strain of bacteria; thus,  $\tau_*$  is held fixed. The theory predicts that  $\overline{D}_A$  is a monotonically increasing function of  $\tau_*$  but a non-monotonic

function of  $Pe$ . Below, I briefly summarize the theoretical predictions for small  $Pe \ll 1$  and large  $Pe \gg 1$ .

Provided  $\tau_* \geq O(1)$ , as in my experiments, theory suggests that  $\overline{D}_A \sim \sqrt{Pe}$  for  $Pe \ll 1$ . Thus the active diffusivity  $D_A \sim cUL^4(UL/D_0)^{\frac{1}{2}}$ ; in terms of particle size  $d$ , this predicts  $D_A \sim \sqrt{d}$ . I do not access this small Peclet number regime in my experiments.

The asymptotic result for very large values of  $\tau_* \gg 1$  with  $Pe \gg 1$  corresponds to non-Brownian tracers in a suspension of non-tumbling bacteria. Both their analytical theory and simulations predict the enhancement in diffusivity to asymptote to constant values that are independent of the Peclet numbers as well as  $\tau^*$ . For finite values of  $\tau^*$  the value of  $\overline{D}_A$  as  $Pe \rightarrow \infty$  depends only on  $\tau^*$  and follows  $\overline{D}_A \approx \frac{\alpha^2}{192\pi M^2} f(\tau_*)$ , where  $\alpha$  and  $M$  are bacteria related geometry parameters and  $f(\tau_*)$  is a scalar function and controls the time scale over which the velocity disturbances induced by swimming bacteria stay correlated. The cells I use are wild type (strain MG1655) with run times of roughly 1 second and  $\tau_* = 1.8$ . From Fig. A.5(b), I find that for the largest Peclet number I attain,  $\overline{D}_A \approx 3.0 \times 10^{-3}$ . This is consistent with asymptotic limits of  $\overline{D}_A \approx 3.4 \times 10^{-3}$  and  $4.2 \times 10^{-3}$  for  $\alpha = 2/7$  [15] and  $M = 0.18$  at  $\tau_* = 1$  and 4, respectively [7].

## A.5 Qualitative estimate for the maximum effective particle diffusivity $D_{\text{eff}}$

My experimental data suggests that both the existence and location of the peak can be tuned by adjusting  $c$  and  $d$  as independent parameters. I now consider a minimal model that yields a quantitative prediction for the existence as well as the location

of the peak in  $D_{\text{eff}}$ .

I first rewrite  $D_{\text{eff}}$  to explicitly incorporate its linear dependence on  $c$ :

$$D_{\text{eff}} = D_0 + (cL^3UL)\overline{D}_A. \quad (\text{A.3})$$

Differentiating  $D_{\text{eff}}$  with respect to  $\text{Pe}$  yields

$$D'_{\text{eff}} = (UL) \left[ -\frac{1}{\text{Pe}^2} + (cL^3)\overline{D}'_A \right]. \quad (\text{A.4})$$

where primes denote differentiation. Setting eqn (A.4) to zero, I conclude that a extremum (shown to be a maximum from the data) in  $D_{\text{eff}}$  exists for

$$cL^3 = (\text{Pe}^2\overline{D}'_A)^{-1}. \quad (\text{A.5})$$

The collapsed universal curve (Fig. 2.5(b)) depends on both  $\text{Pe}$  and  $\tau^*$ ; in my case  $\tau^*$  is a constant. Using the experimentally collapse curve, I approximate the slope  $\overline{D}'_A$  by fitting the data (Fig. A.5(b)) to the form

$$\overline{D}_A(\text{Pe}) \approx \left[ A_0 - \frac{1}{2}A_1(\text{Pe}_A - \text{Pe})^2 \right]. \quad (\text{A.6})$$

Here  $A_0 = \overline{D}_A(\text{Pe}_A)$  with  $\text{Pe}_A$  being the Péclet number at which  $\overline{D}_A$  is a maximum. In the general case,  $A_0$ ,  $A_1$  and  $\text{Pe}_A$  would be functions of  $\tau^*$ . I fit the collapsed  $\overline{D}_A$  data (Fig. A.5(b)) for the range  $200 < \text{Pe} < 4000$  to eqn (A.6) and obtain  $\text{Pe}_A \approx 1000$  and  $A_1 \approx 5 \times 10^{-7}$ . From eqn (A.6), it follows that the slope is given by  $\overline{D}'_A(\text{Pe}) \approx A_1(\text{Pe}_A - \text{Pe})$ .

I next estimate the magnitude and location of the maximum  $D_{\text{eff}}$  by substituting eqn (A.6) into eqn (A.5). The Péclet number  $\text{Pe}_{\text{max}}$  at which  $D_{\text{eff}}$  is maximum is



given by the cubic equation

$$cL^3 A_1 (\text{Pe}_A - \text{Pe}_{\max}) = \text{Pe}_{\max}^{-2}. \quad (\text{A.7})$$

I am interested in how  $\text{Pe}_{\max}$  changes with  $c$  and so I seek an approximate asymptotic real and physically valid solution for  $\text{Pe}_{\max}$ .

Let  $\delta\text{Pe}$  be a measure of the deviation from  $\text{Pe}_A$  defined through  $\text{Pe}_{\max} = \text{Pe}_A - \delta\text{Pe}$ . Note that  $\text{Pe}_{\max} < \text{Pe}_A$  so that by definition  $\delta\text{Pe} > 0$ . I substitute  $\text{Pe}_{\max} = \text{Pe}_A - \delta\text{Pe}$  into eqn (A.7), Taylor expand the right and left hand sides, simplify the resulting expansions by utilizing the conditions  $\text{Pe}_{\max}^2 \gg 1$  and  $\delta\text{Pe} \ll \text{Pe}_A$  and finally retain terms to  $O(\delta\text{Pe})$ . This then gives us the equation

$$(\text{Pe}_A^3 cL^3 A_1 - 2) \delta\text{Pe} \approx \text{Pe}_A. \quad (\text{A.8})$$

The constraint that  $\delta\text{Pe} > 0$  results in the inequality  $\text{Pe}_A^3 cL^3 A_1 > 2$  for a valid solution to exist. Furthermore, eqn (A.8) provides the shift in the peak,  $\delta\text{Pe}$  relative to  $\text{Pe}_A$ , when it exists. Using the expression for  $\delta\text{Pe}$  from eqn (A.8) I obtain expressions for the location of the peak  $\text{Pe}_{\max}$  and thereby its dependence on  $c$ ,  $\text{Pe}_{\max} = \text{Pe}_A \left[ 1 - \left( \frac{1}{\text{Pe}_A^3 cL^3 A_1 - 2} \right) \right]$ , and  $d_{\text{eff}}^{\max} = d_A \left[ 1 - \left( \frac{1}{\text{Pe}_A^3 cL^3 A_1 - 2} \right) \right]$  is the corresponding location in particle size  $d_{\text{eff}}^{\max}$  where  $d_A$  is the particle diameter corresponding to  $\text{Pe}_A$ . In my case, plugging in  $A_1 \approx 5 \times 10^{-7}$  and  $\text{Pe}_A \approx 1000$ , yields

$$d_{\text{eff}}^{\max} = d_A \left[ 1 - \left( \frac{1}{5cL^3 - 2} \right) \right] \quad (\text{A.9})$$

Note that as  $c$  increases,  $d_{\text{eff}}^{\max}$  increases, consistent with my experimental observations (Fig. A.3(a)).

The magnitude of the maximum effective diffusivity  $D_{\text{eff}}^{\max}$  is thus evaluated as

$$\frac{D_{\text{eff}}^{\text{max}}}{UL} = \frac{1}{\text{Pe}_A} + cL^3 \left( A_0 - \frac{A_1}{A_2} \right) \text{ where } A_2 = \frac{2}{\text{Pe}_A^2} \left( \text{Pe}_A^3 cL^3 A_1 - 2 \right)^2.$$

# Bibliography

- [1] Saffman PG, Delbruck M. 1975. **Brownian motion in biological membranes.** *Proceedings of the National Academy of Sciences* 72:3111-3113
- [2] Kurtuldu H, Guasto JS, Johnson KA, Gollub GP. 2011. **Enhancement of biomixing by swimming algal cells in two-dimensional films.** *Proceedings of the National Academy of Sciences* 108:10391.
- [3] Zaid IM, Dunkel J, Yeomans J.M. 2011. **Lévy fluctuations and mixing in dilute suspensions of algae and bacteria.** *J. R. Soc. Interface* 8:1314-1331.
- [4] Leptos KC, Guasto JS, Gollub JP, Pesci AI, Goldstein RE. 2009. **Dynamics of Enhanced Tracer Diffusion in Suspensions of Swimming Eukaryotic Microorganisms.** *Physical Review Letters* 103:198103 .
- [5] Toyota T, Head DA, Schmidt CF, Mizuno D. 2011. **Non-Gaussian athermal fluctuations in active gels.** *Soft Matter* 7:3234.
- [6] Pathria PK. 1996. **Statistical Mechanics.** *Butterworth, Oxford.*
- [7] Kasyap TV, Koch DL, Wu M. 2014. **Hydrodynamic tracer diffusion in suspensions of swimming bacteria.** *Physics of Fluids* 26:081901.
- [8] Kim MJ, Breuer KS. 2004. **Enhanced diffusion due to motile bacteria.** *Physics of Fluids* 16:L78.
- [9] Jepson A, Martinez VA, Schwarz-Linek J, Morozov A, Poon WC. 2013. **Enhanced diffusion of nonswimmers in a three-dimensional bath of motile bacteria.** *Physical Review E* 88:041002.

- [10] Mino G, Mallouk TE, Darnige T, Hoyos M, Dauchet J, Dunstan J, Soto R, Wang Y, Rousselet A, Clement E. 2011. **Enhanced diffusion due to active swimmers at a solid surface.** *Physical Review Letters* 106:048102 .
- [11] Vaccari L, Allan DB, Sharifi-Mood N, Singh AR, Leheny RL, Stebe KJ. 2015. **Films of bacteria at interfaces: three stages of behaviour.** *Soft Matter* 11:6062-6074.
- [12] Palacci J, Cottin-Bizonne C, Ybert C, Bocquet L. 2010. **Sedimentation and Effective Temperature of Active Colloidal Suspensions.** *Physical Review Letters* 105:088304.
- [13] Koumakis N, Maggi C, Di Leonardo R. 2014. **Directed transport of active particles over asymmetric energy barriers .** *Soft Matter* 10:5695.
- [14] Maggi C, Paoluzzi M, Pellicciotta N, Lepore A, Angelani L, Di Leonardo R. 2014. **Generalized Energy Equipartition in Harmonic Oscillators Driven by Active Baths.** *Physical Review Letters* 113:238303.
- [15] Berg H, Turner L. 1995. **Cells of *Escherichia coli* swim either end forward.** *Proceedings of the National Academy of Sciences* 92:477-479.

# Appendix B

## Supplementary Materials for swimming *E. coli* in polymer solutions

### B.1 Rheological characterization of solutions

#### B.1.1 Shear viscosity and elasticity of CMC solutions

The shear viscosity of the carboxymethyl cellulose solutions is measured with a cone-and-plate rheometer, over a range of shear rates 10 to 1000  $\text{s}^{-1}$ . For dilute suspensions ( $c = 10$  ppm), the fluid is nearly Newtonian. However, at higher concentrations, the solutions are shear thinning. I define an effective viscosity experienced by the bacterial cell as the average shear viscosity over the shear rates of 10-100  $\text{s}^{-1}$ . This range of shear rates was chosen since it corresponds to *E. coli* flagellar bundle rates (50-100  $\text{s}^{-1}$ ) [1, 2]. As shown in Fig. B.1, the viscosity increases from 1.0 to 20.0 mPa  $\cdot$  s with polymer concentration for polymer molecular weight  $9.0 \times 10^4$ ,  $2.5 \times 10^5$ , and  $7.0 \times 10^5$ .

At low concentrations, the shear viscosity is nearly constant with shear rate. At higher concentrations, particular for MW=  $7.0 \times 10^5$ , the shear viscosity begins to decrease with increasing shear rate (Fig. B.1a). The shear-thinning viscosity  $\eta$  can be described by a model power law fluid, such

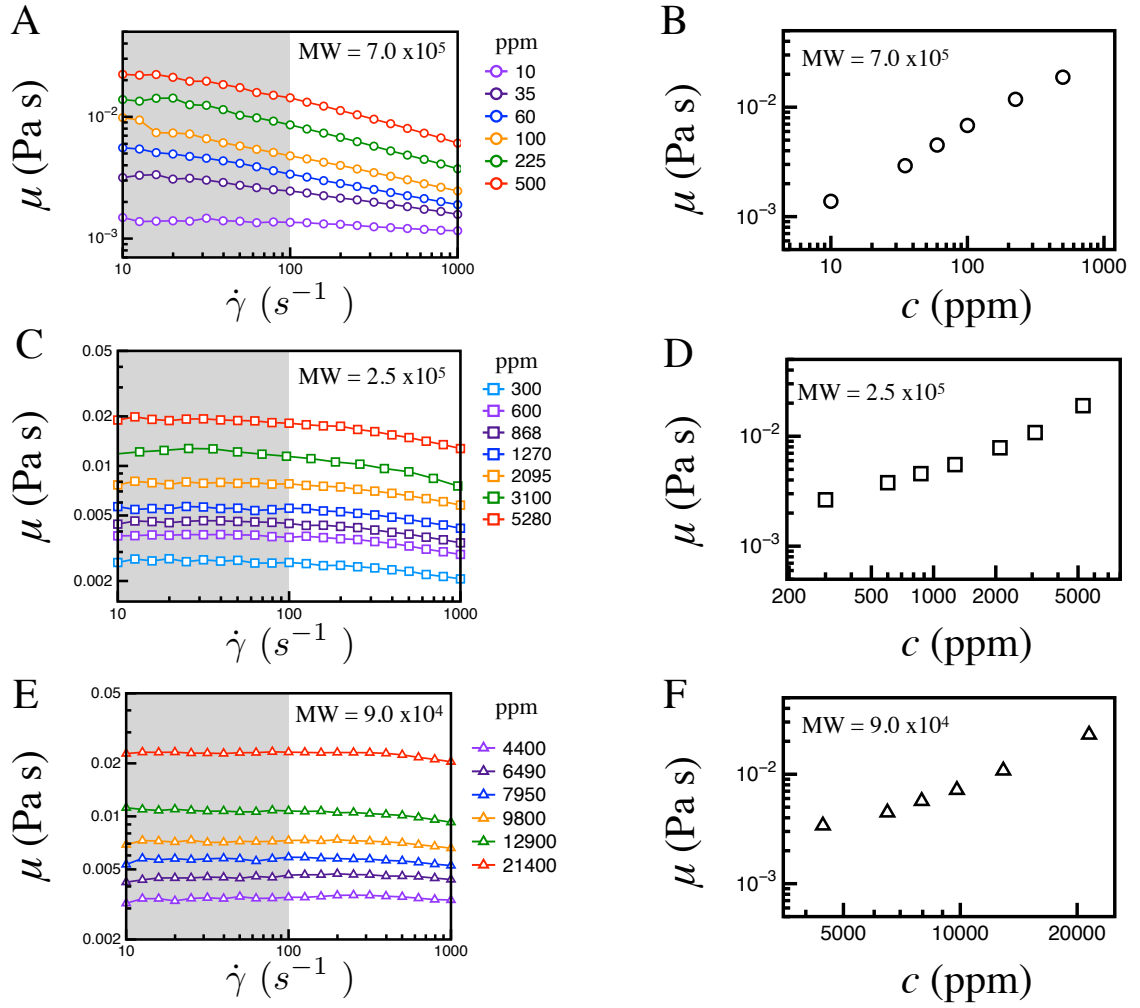


Figure B.1: Shear viscosity of CMC solutions. (A) Shear viscosity of CMC ( $MW = 7.0 \times 10^5$ ) at polymer concentrations ranging from 10 to 500 ppm. (B) The shear viscosity magnitude, defined as the mean shear viscosity over 10-100  $s^{-1}$ , increases from 1.0 to 20.0  $mPa \cdot s$  as the polymer concentration increases. The shear viscosities for  $MW = 2.5 \times 10^5$  (C, D) and  $MW = 9.0 \times 10^4$  (E, F) also range from 1.0 to 20.0  $mPa \cdot s$ .

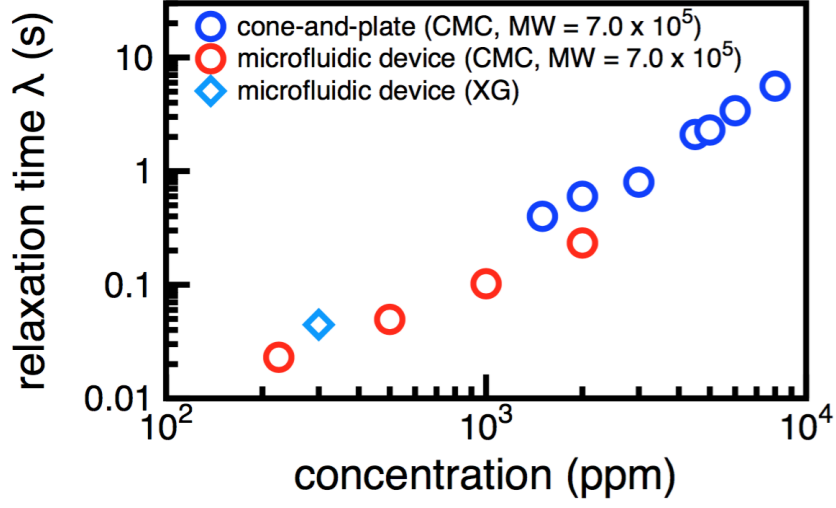


Figure B.2: The relaxation times for CMC ( $MW = 7.0 \times 10^5$ ) and XG solutions versus concentration as determined by a microfluidic device are consistent with relaxation time measurements at higher concentrations in a cone-and-plate rheometer [4].

that  $\eta = \kappa \dot{\gamma}^{n-1}$ , where  $n$  is the shear-thinning index. At the highest concentration ( $c = 500$  ppm,  $MW = 7.0 \times 10^5$ ), the shear-thinning index reaches a minimum of 0.70, as shown in Table B.1.

Table B.1: Rheological properties of CMC ( $MW = 7.0 \times 10^5$ ) solutions

$c$ (ppm)	$\mu$ (mPa $\cdot$ s)	$n$	$\lambda$ (ms)
0	0.97	N/A	-
10	1.38	0.95	-
35	2.92	0.84	-
60	4.51	0.77	-
100	6.81	0.73	-
225	11.8	0.72	23.0
500	18.8	0.77	49.5

The fluid elasticity is quantified by measuring the relaxation time,  $\lambda$  of the CMC solutions ( $MW = 7.0 \times 10^5$ ). This time scale is determined via a creep recovery test in a microfluidic device [3]. I find that the relaxation times increase from 0.02 seconds to 2.0 seconds as the polymer concentration

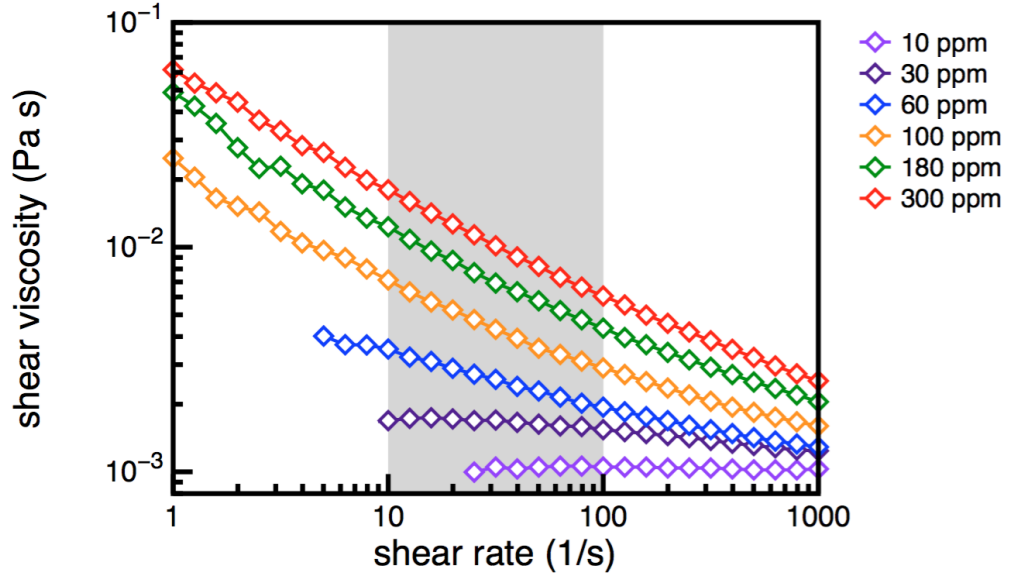


Figure B.3: Shear viscosity versus shear rate for Xanthan Gum solutions. The viscosity significantly shear thins, particularly in the region of interest,  $\dot{\gamma} = 10 - 100 \text{ s}^{-1}$ . At the highest concentration, the shear-thinning index  $n$  reaches a minimum of 0.50.

varies from 200 to 4000 ppm, as shown in Fig. B.2. The relaxation times I measure in the microfluidic device are qualitatively consistent with measurements made independently in a macroscopic cone-and-plate rheometer [4] and provides a measure of the elasticity in the highest concentrated CMC solutions used with *E. coli* ( $c = 225, 500 \text{ ppm}$ ).

## XG Rheology

As mentioned in the previous section, the relaxation times  $\lambda$  are determined via a creep recovery test in a in-house microfluidic device. I find that for the highest XG concentration ( $c = 300 \text{ ppm}$ ),  $\lambda$  is approximately 44 ms, as shown in Fig. B.2.

The shear viscosities of XG solutions are measure in a cone and plate rheometer. As shown in Fig. B.3, the viscosity significantly shear thins, particularly in the region of interest,  $\dot{\gamma} = 10 - 100 \text{ s}^{-1}$ . At the highest concentration, the shear-thinning index  $n$  reaches a minimum of 0.50 (Table B.2).



Table B.2: Rheological properties of XG

$c$ (ppm)	$n$
10	1.01
30	0.92
60	0.76
100	0.64
180	0.57
100	0.51

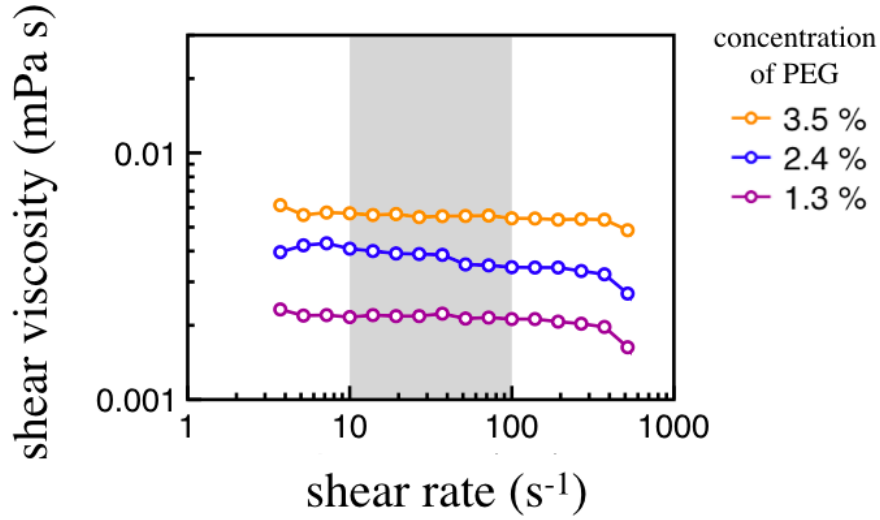


Figure B.4: Shear viscosity of PEG solutions at polymer concentrations ranging from 1.3 to 10% by weight. The shear viscosity magnitude increases from 2 mPa·s to 30 mPa·s. There is negligible change in viscosity with shear rate, exhibiting Newtonian behavior.

### Rheology of PEG solutions

The shear viscosities of PEG solutions are measured with a cone-and-plate rheometer. For the range of concentrations used ( $c = 1.3\text{-}10\%$  by weight), the shear viscosity increases from 2 to 30 mPa·s, as shown in Fig. B.4. Furthermore, shear viscosity is nearly constant with shear rate, indicating that PEG solutions provide a model Newtonian fluid.

## B.2 Methods

### Prepping and tracking cells suspended in thin film

Suspensions of *E. coli* are prepared by growing the cells (wild type K12 MG1655) to saturation ( $10^9$  cells/mL) in culture media (LB broth, Sigma-Aldrich). The saturated culture is gently cleaned by centrifugation and re-suspended in the fluid of choice at dilute concentrations ( $5 \times 10^7$  cells/mL).

Experiments are performed in a thin fluid film by placing a 2- $\mu$ L drop of cell-polymer/cell-buffer suspension in an adjustable wire frame and stretching the film to measured thickness 80  $\mu$ m. The film interfaces are nearly stress-free which minimizes velocity gradients transverse to the film. *E. coli* are imaged with phase-contrast microscopy, and videos are taken at 30 frames per second. The positions of the cell body  $r(t)$  are gathered over time  $t$  via standard particle tracking techniques [54].

### Run and tumble times of tethered cells

During the run or tumble states, the cell motor rotates in a counter clockwise (CCW) or clockwise (CW) direction, respectively, when viewed from behind. I use a sticky-flagellated mutant *E. coli* (strain MDG201) [31] to tether the cells to glass surfaces by their flagella. As the cell motor rotates, the body of the cell rotates about its tethered flagella in either a CCW or CW fashion, revealing the state of the motor. In SI Movie 2, sample tethered cells are shown in Newtonian fluids (solutions of PEG) and viscoelastic fluids (solutions of CMC). As the viscosity increases, the tethered cells exhibit two changes: (1) a decrease in rotational speed and (2) also an increase in both run (CCW) and tumble (CW) time intervals, measured from approximately 100 switching events.

For a cell in a Newtonian fluid, the torque on the motor is proportional to the frequency of rotation  $\omega$  and the viscosity  $\mu$ . For cells that operate at constant torque [28,31], an increase in viscosity should yield lower rotation rates, consistent with the observed decrease in rotation rates. In Fig 3.4 E, I see that the mean run and tumble times of individual cells tend to increase with viscosity for both the CMC and PEG solutions. The increase in run and tumbles times are verified by linear regressions, which reveal positive correlations among the time intervals and viscosity. Table 1 displays the slopes of the linear regressions. A t-test conducted at  $\alpha = 0.05$  ( $t_c=1.68$ ) indicate that the slopes are statistically the same between the PEG and CMC solutions for the run time ( $t=0.9$ , p-value=  $7 \times 10^7$ ) with viscosity and the tumbles times ( $t=1.0$ , p-value=  $2 \times 10^5$ ) with viscosity.

Furthermore, the presence of elasticity in the CMC does not significantly alter the run and tumble times. Instead, the increase in run and tumble times of tethered cells can statistically be accounted for by viscosity alone.

Table B.3: Results of linear regression analysis

	slope	$t_c$	t	p-value
CMC run time	1.59	1.68	0.86	$7 \times 10^{-7}$
PEG run time	1.11	1.68	0.86	$7 \times 10^{-7}$
CMC tumble time	0.053	1.68	1.04	$2 \times 10^{-5}$
PEG tumble time	0.099	1.68	1.04	$2 \times 10^{-5}$

## Fluorescently-stained DNA molecules

I fluorescently stain  $\lambda$ -DNA (MW=  $3 \times 10^7$ ) polymers to visualize the interaction of tethered cells with individual polymer molecules. Suspensions of  $\lambda$ -DNA are prepared by heating  $\lambda$ -DNA stock solution at a temperature of 65°C for 10 min and then quenching the sample in an ice bath for 3 minutes. The DNA molecules were stained with YOYO-1 iodide at a dye to base pair ratio of 1:4 and left to incubate at room temperature for one hour. The stained molecules were suspended in TE buffer with 4% (v/v) -mercaptoethanol, which reduces the amount of photo-bleaching. The final concentration is 0.10  $c^*$ , where  $c^* = 40 \mu\text{g/mL}$ .

The fluorescently stained  $\lambda$ -DNA polymer molecules are suspended in a buffer solution with mutant E. coli cells: These mutants, strain PL4, contain the sticky-flagella for tethering and also always ‘run’. Once a tethered cell is identified using bright field microscopy, the polymer molecules around the cells are visualized with fluorescence microscopy.

## Model for tumbling rates

The E. coli motor is a rotary motor comprised of the flagellar hook and several rings of proteins and is driven by an ion gradient acting across the cell membrane [31]. The flow of protons through the motor induces conformational changes in the stator proteins, which generate a torque on the rotor. The binding of a protein molecule Che-Y to the cell motor induces a conformational change of the

motor, thereby promoting the switching of the motor direction from CCW to CW and initiating a tumbling event. When Che-Y molecules unbind, the motor regains its original conformation and reverses direction again.

Duke *et al.* [44] proposed a thermal isomerization model to describe the switching dynamics in the absence of an external load. In this model, the motor switching rate is proportional to  $e^{-\Delta G/kT}$ , where  $\Delta G$  is the energy difference between the free energy of the barrier and the energy of the CCW or CW state. The binding of Che-Y molecules to the motor lowers the free energy barrier, setting the internal switching rate  $k^*$  [31,32,43,44]. I propose that in a viscous fluid, the motor experiences a mechanical load due to viscous drag on the flagella. In order to reverse the motor rotation direction, the motor must overcome this viscous torque  $M$ . I hypothesize that this effect results in an additional energy barrier that has to be overcome for an attempted switching event to be ultimately successful. The height of this barrier may be estimated as the product of an external fluid resistive torque (and therefore external viscosity) and an internal state variable related to motor configurations, a characteristic angle  $\beta$ . With these simplifications, the net motor switching rate becomes  $k^* e^{-M\beta/kT}$  and thus decreases with viscous torque on the flagella. Using this model, I predict the rotational diffusion of *E. coli* as a function of viscosity as  $D_R = D_R^0 + A * k^* e^{-/kT} = \frac{kT}{f_0\mu} + Ae^{-B\mu}$ , where the mechanical loading is due to viscous stresses on the motor. The parameter  $B$ , defined as  $B = /kT\mu$ , corresponds to a motor torque  $M = 650$  pN nm in water [34] and a characteristic angle  $\beta = 0.025^\circ$ . This characteristic angle reflects the orientational change in the configuration of a stator protein subunit during a switching event [43]. Since the flagellar motor contains many stator protein subunits, one should more generally interpret  $\beta$  as a weighted angle and  $\beta M$  as a weighted average amount of work performed by the stators to switch the motor.

## Estimate of force generated from tethered cells

The tangential flow field around a sphere of radius rotating about an axis with angular frequency  $\omega$  and evaluated in its mid-plane is given by  $v_\theta(r) \sim a\omega(a/r)^2$ . Assuming the DNA molecule is at distance  $R$ , the velocity gradient in the radial direction can be estimated and the shear rate is roughly given by  $|\gamma| \sim 2(a/R)^3\omega$ . The actual shear rate differs from the order of magnitude estimate due to the shape of the bacterial cell and the presence of the wall. Using  $a = 0.7 \mu\text{m}$ ,  $R_g = 2.4 \mu\text{m}$  and  $\omega = 0.9(2\pi)\text{s}^{-1}$ , I find  $|\gamma| \sim 2.8\text{s}^{-1}$ . The polymer stretches from the small deviation from the

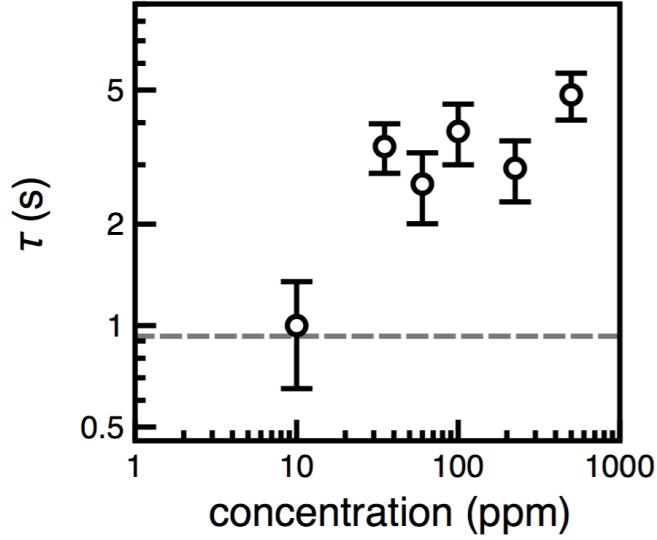


Figure B.5: The crossover time  $\tau$  increases from 0.9 to 4.8 s as polymer concentration increases up to 500 ppm (CMC, MW =  $7.0 \times 10^5$ ). The result for buffer is included for reference.

streamline on which the center of mass moves. Balancing the lateral (cross streamline) extension of the blob with radius of gyration  $R_g$  and persistence length  $L_p$  of approximately 50 nm with Brownian forces, I estimate the flow induced force due to the fluid of viscosity  $\eta$  extending the polymer as  $F = \zeta\gamma(2k_B T/k_\perp)^{1/2}$  where  $\zeta = 6\pi\eta R_g$  and  $k_\perp = kT/L_p\ell_c$  are the viscous drag coefficient and effective polymer stiffness respectively. Plugging in values, I find  $F \sim 49$  fN this estimate is an upper limit.

### B.3 MSD Crossover time increases with polymer concentration

For *E. coli*, the dynamics of its entire trajectory can be captured using the relationship  $MSD(\Delta t) = 4D_T\Delta t(1 - e^{-\Delta t/\tau})$ , where  $\tau$  is a typical crossover time marking the transition from ballistic and diffusive manner. The crossover time is related to the mean run time of the ballistic runs  $\tau_R$ . The MSD is proportional to  $4D_T(\Delta t)^2/\tau$  for  $\Delta t \ll \tau_R$  and to  $4D_T\Delta t$  for  $\Delta t \gg \tau_R$ . By fitting the MSD data in Fig. 3.3(a) to this relation, I find that the crossover time  $\tau$  increases with polymer concentration from 0.9 to 4.8 s, as shown in Fig. B.5.

## B.4 *E. coli* Rotational Diffusivity and Mean Run Time

The rotational diffusion  $D_R$  for a run-and-tumble particle depends on the mean tumble angle  $\alpha$  and the mean run time  $\tau$  as  $D_R = (1 - \cos\alpha)/\tau_R$  [5]. The tumble angles are defined by the angular change in direction from run to run, as shown in Fig. B.6a. Averaging over multiple tumbles and multiple cells, I find the mean tumble angle remains nearly constant with polymer concentration Fig. B.6b. The tumble angle depends on the effective torque acting on the cell body that rotates it about an axis different from the direction of motion- the rotation being due to the fact that the flagella are unbundled [1]. Specifically, the tumble angle is proportional to this tumble torque  $\tau_t$  and the tumble time. The tumble torque  $\tau_t$  is proportional to the fluid viscosity. In the experiments, the fluid viscosity varies by a factor of about 20. Thus, I expect the tumble torque to increase correspondingly by a factor of approximately 20 as well. However, this effect combined with the simultaneously observed increased in mean tumble times (Fig. 3.4b and 3.4e) results in a nearly constant mean tumble angle. A cell attempting to tumble in polymer solutions is successful and can thus change direction by the same amount as in a fluid without polymer. This suggests that the change in rotational diffusion of cells (Fig. 3.4c) is primarily due to the changes in run time and not changes in tumble angle.

## B.5 Suppression of Wobbling with Molecular Weight

Figure B.7a shows the mean cell velocity  $\langle v \rangle$  as a function of fluid viscosity for CMC solutions of different MW and a XG solution. While  $\langle v \rangle$  increases with  $\mu$  for the highest molecular weight CMC and XG solutions, the relative enhancement in  $v$  diminishes as the CMC molecular weight (and thus elasticity) decreases. This is evident if one selects a specific viscosity ( $\mu = 11$  mPa s, shaded in Fig. B.7a, where  $\langle v \rangle v$  clearly decreases with CMC molecular weight. The increase in  $\langle v \rangle$  with CMC molecular weight (MW) is consistent with the simultaneous decrease in wobbling  $\langle \sigma(\phi) \rangle$  with MW, shown in Fig. B.7b for  $\mu = 11$  mPa s. We note that *E. coli* swimming in the highest MW CMC and XG solutions show effectively the same degree of wobbling  $\langle \sigma(\phi) \rangle$  (and  $\langle v \rangle$ ) even though their power law indexes are quite different, which strongly indicates that shear-thinning viscosity effects

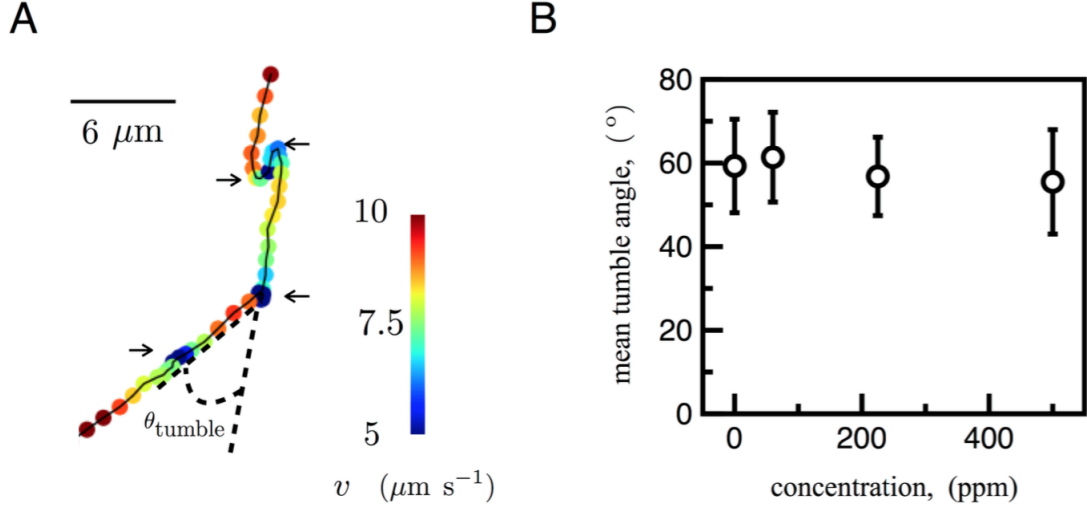


Figure B.6: (A) The tumble angles are defined by the angular change in direction from run to run. (B) The mean tumble angle, averaged over multiple tumbles in multiple cells, remains nearly constant with concentration.

are not important.

## B.6 Polymer dynamics due to flow generated by tethered cells

I quantify polymer extension by measuring an effective length of the polymer molecule,  $\ell$ , defined to be the maximum distance along two points of the cell's contour. This allows us to quantify the polymer extension in terms of a single dimensionless function – the distribution of  $\ell/\ell_c$  – where  $\ell_c$  is the contour length of (typically  $22.0 \mu\text{m}$  for my DNA polymer) [14]. Note that this is not the same as the end-to-end distance and so statistics of this normalized length yield order of magnitude estimates. For weak flow fields, an estimate of the fluid force resulting in polymer stretching can be estimated by examining the distribution of  $\ell/\ell_c$  over a time for which the polymer feels the constant flow gradients. While the actual flow field is time dependent, one may assume that sampling and reorientations are sufficiently quick. In my case, this would correspond to sampling the lengths when the polymer is at the same distance from the tethered cell. For ease of analysis, I assume that the statistical properties of the end-to-end distance are comparable to that of  $\ell/\ell_c$  of the DNA blob. Hence I now study the

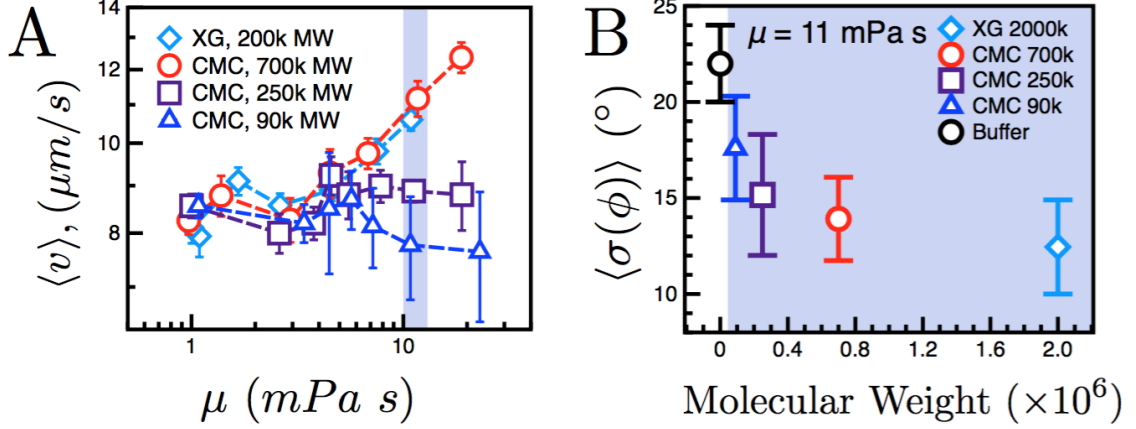


Figure B.7: (a) Cell velocities as a function of viscosity for varying polymers. At  $\mu = 11 \text{ mPa s}$  (shaded), the velocity increases with MW. (b) For  $\mu = 11 \text{ mPa s}$ ,  $\langle \sigma(\phi) \rangle$  decreases with MW, suggesting that fluid elasticity suppresses wobbling. The result in buffer is included for reference.

shift in the distribution function characterizing the end-to-end distance as a function of extensional forces generated as the DNA polymer samples the local flow field. The DNA configuration can typically be modeled as a self-avoiding walk (SAW) in two-dimensions. The distribution of end-to-end distance,  $x$ , under thermal fluctuations alone follows  $PDF(x) = ax^{1+\sigma}e^{-bx^\delta}$  with scaling exponents given by  $\sigma = 0.44$  and  $\delta = 4$  [7, 8]. The constant  $a$  is determined by the normalization condition. The constant  $b$  is related to the mean end-to-end distance and depends on the number of effectively independent chains constituting the polymer chain,  $N$ , and an effective segment length ( $r_0 = 50 \text{ nm}$  [6]), and is given by  $b = (r_0 N^{3/4})^{-\delta}$  where the contour length  $\ell_c = r_0 N$ . Rewritten explicitly in terms of the contour length, I get in the absence of imposed forces the equilibrium distribution

$$PDF(x/\ell_c) = \ell_c^{1+\sigma} a (x/\ell_c)^{1+\sigma} e^{-\frac{\ell_c F(x/\ell_c)}{k_B T}} \quad (\text{B.1})$$

where  $b^* = b(\ell_c)^\delta = r_0^\delta N^{\delta/4}$ . When a constant stretching (elongational) force  $F$  is applied to the polymer, the distribution function of end-to-end distances shifts. The distribution shifts accordingly to accommodate entropic effects [9] and attains the form:

$$PDF(x/\ell_c) = \ell_c^{1+\sigma} a (x/\ell_c)^{1+\sigma} e^{-b^*(x/\ell_c)^\delta} e^{-\frac{\ell_c F(x/\ell_c)}{k_B T}} \quad (\text{B.2})$$



I next quantify the PDF of the scaled stretch near the cell (at a radial distance  $5\text{ }\mu\text{m}$ ) and the PDF of the DNA in the absence of a cell both shown in Fig. B.8. Modeling the polymer in the absence of cells using Eq'n B.1, and fixing  $\sigma = 0.44$  and  $\delta = 4$ , I obtain  $b^* = 3100$ . By fixing  $\sigma = 0.44$ ,  $\delta = 4$  and  $b^* = 3100$ , I next fit the data in Fig. B.8 to Eq'n. B.2 and obtain  $F = 4.5\text{ fN}$  as an estimate of the effective fluid flow induced extensional force stretching the polymer, as shown in Fig. B.8.

## B.7 Estimation of Weissenberg Numbers

### A. Weissenberg numbers for freely swimming cells

The Weissenberg number  $Wi$  is defined here as the product of the fluid relaxation time  $\lambda$  and the characteristic frequency of the swimmer  $f$ , where  $f$  is the rotation rate of the *E. coli* bundle. Thus,  $Wi = 2\pi f\lambda$ . The relaxation times are estimated from previous measurements of CMC solutions in a macroscopic cone-and-plate rheometer [7] using a simple extrapolation scheme.

Next, the bundle rotation rates for my polymeric solutions are estimated using their viscosity values. Previous experiments have shown that bundle rotation rate decreases with viscosity [8]. Although the bundle rotation rate is not directly observed in the experiments, the viscosity of the solutions is well characterized (c.f. Fig. B.1). I use the available data [8] to estimate the average bundle rotation rate  $f$ . Assuming that the bundle rotation rate decreases as the inverse of the viscosity, the estimated bundle rotation rate  $f$  decreases from 130 to 55 Hz as the polymer concentration increases from 0 to 500 ppm, as shown in Table B.4. From these values, our estimated range of  $Wi = 2\pi f\lambda$  is 0.03 to 13.6 (Table B.4).

### Weissenberg numbers for DNA polymer near tethered *E. coli*

For the DNA molecule in water, the relaxation time  $\lambda$  is approximately 3 seconds [9]. The estimated shear rates  $\dot{\gamma}$  due to the flow generated by the tethered cell (Fig. 6) are approximately  $2.8\text{ s}^{-1}$  (B.6), which leads to  $Wi = 2\pi f\lambda \approx 8.4$ .

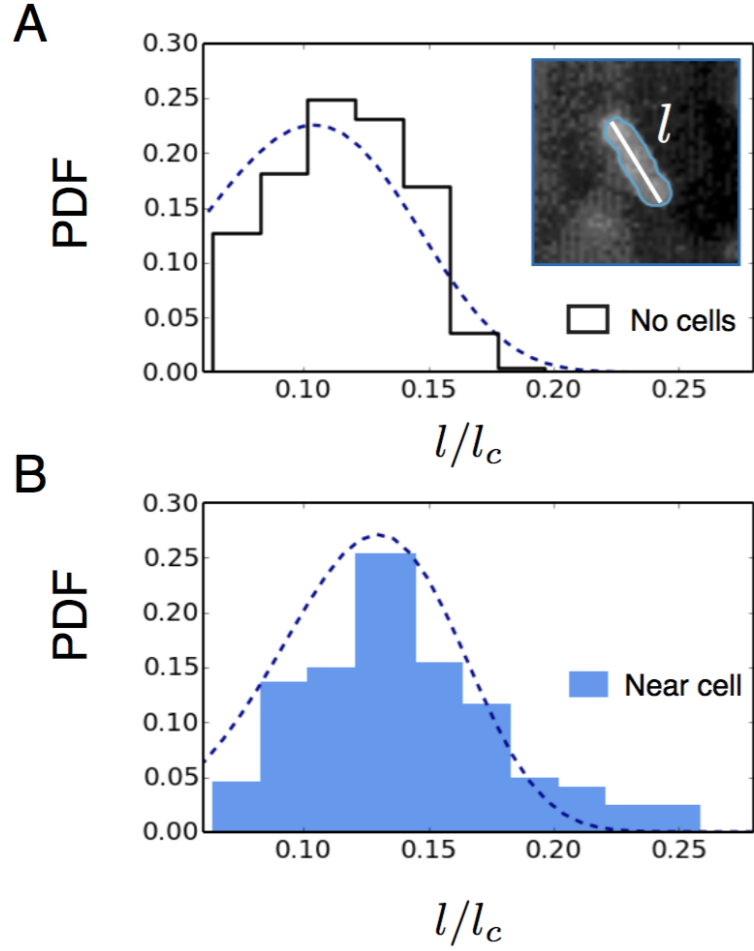


Figure B.8: Stretching of polymer molecule quantified using the probability distribution of a normalized extension given by the ratio of the length-scale  $l$  (the maximum distance along two points of the contour) and its contour length  $l_c$ . (A) The PDF for polymer molecules in the absence of cells. The dashed line corresponds to the predicted PDF for a self-avoiding random walk in two dimensions [7]. (Inset) Definition of the length  $l$ . (B) Normalized length fluctuations for the polymer near the cell are due to a contribution of thermal motion and its interaction with the cell. As can be seen the distribution function shifts to the right suggesting an extended state. The dashed line corresponds to Eq'n B.2.

Table B.4: Viscosity, concentration, relaxation time, and bundle rotation frequencies used to estimate Wi in solutions of CMC.

$\mu$ (mPa s)	$c$ (ppm)	$\lambda$ (s)	$f$ (Hz)	Wi
0.97	0	0.0	130	0
1.38	10	$2.6 \times 10^{-5}$	100	0.03
2.92	35	$3.6 \times 10^{-4}$	72	0.15
4.51	60	$8.98 \times 10^{-4}$	66	0.37
6.81	100	$2.2 \times 10^{-3}$	61	0.85
11.8	225	$9.5 \times 10^{-3}$	56	3.3
18.8	500	$3.96 \times 10^{-2}$	54	13.6

# Bibliography

- [1] Darnton NC, Turner L, Rojevsky S, Berg HC. 2006. **On torque and tumbling in swimming *Escherichia coli*.** *Journal of Bacteriology* 189:1756-1764.
- [2] Sowa Y, Berry RM. 2008. **Bacterial flagellar motor.** *Quarterly Reviews of Biophysics* 41:103-132.
- [3] Koser AE, Pan L, Keim NC, Arratia PE. 2013. **Measuring material relaxation and creep recovery in a microfluidic device.** *Lab on a Chip* 13:1850-1853.
- [4] Shen XN, Arratia PE. 2011. **Undulatory swimming in viscoelastic fluids.** *Physical Review Letters* 106:208101.
- [5] Lovely PS, Dahlquist FW. 1975. **Statistical measures of bacterial motility and chemotaxis.** *Journal of Theoretical Biology* 50:477-496.
- [6] Smith DE, Babcock HP, Chu S. 1999. **Single-polymer dynamics in steady shear flow.** *Science* 283:1724-1727.
- [7] Valle F, Favre M, De Los Rios P, Rosa A, Dietler G. 2005. **Scaling exponents and probability distributions of DNA end-to-end distance.** *Physical Review Letters* 95:158105.
- [8] de Gennes PG. 1979. **Scaling Concepts in Polymer Physics.** *Cornell University Press*.
- [9] Su T. 2011. **Entropic elasticity of polymers and their networks.** Ph. D. Thesis: *University of Pennsylvania: USA*.
- [10] Perkins TT, Quake SR, Smith DE, Chu S. 1994. **Relaxation of a Single DNA Molecule Observed by Optical Microscopy.** *Science* 264:822-826.